POLITECNICO

MILANO 1863

SCUOLA DI INGEGNERIA INDUSTRIALE
E DELL'INFORMAZIONE

Design and Performance Analysis of Reversible Axial Turbomachinery for Pumped Thermal Energy Storage Applications

TESI DI LAUREA MAGISTRALE IN
MECHANICAL ENGINEERING - INGEGNERIA MECCANICA

Author: **Matteo Pozzi**

Student ID: 10578957
Advisor: Prof. Alessandro Romei
Academic Year: 2022-23

*"Meglio un asino vivo
che un professore morto"*

Maria Luisa Nova

Abstract

In this thesis a method to design and to analyse axial reversible turbomachinery is presented. Reversible turbomachinery can act both as a compressor or as a turbine, depending on the flow direction. Their application is intended for a Pumped Thermal Energy Storage system (PTES), which exploits a closed reversible Brayton cycle. The utilization of reversible machines allows the simplification of the plant and a potential cost reduction. Aim of this thesis is twofold: at first, accomplish a preliminary design of this unconventional machine through a purposely developed meanline method, and then check the meanline validity through computational fluid-dynamics (CFD) simulations. Taking a reference PTES with a charge net power of 10 MW, the design of the compressor mode, which is the most critical operating mode, is obtained through a meanline code, followed by the analysis of the turbine mode. Codes are validated through full three-dimensional CFD simulations. It was found that the integral compressor performance deviate from the meanline prediction by 1%, while significant errors were found when comparing the turbine operation. Given the different fluidynamic between the two modes, the turbine mode exhibits negative incidences on all cascades, which combines with the small flow deflection imposed by the compressor mode and results in poor predictive capabilities of the meanline approach and in low efficiencies. Different working fluids and machine architectures were tested. Argon increases the costs for the heat exchangers, but it allows a lower pressure ratio, therefore a lower number of stages with respect to nitrogen. Pressure ratio for the charge mode is 2.08, compared to 2.95 for nitrogen, while for discharge mode is 2.35, compared to 3.33 for nitrogen, allowing 8 stages for the argon machines, while 12 for the nitrogen ones. The machine architecture with inlet and outlet guide vanes exhibits higher efficiency and a much simpler design with respect to the machine composed by only rotors and stators. Compressor isentropic efficiency for charge and discharge mode resulted 89.6% and 84% for argon, while 86.7% and 84.9% for nitrogen. Turbine modes were analysed using the same mass flow rate, but the target outlet pressure could not be reached due to the excessive negative incidence, which made turbine rotors act as compressor ones. Nevertheless, argon machines exhibited lower incidence and higher expansion ratio.

Keywords: Reversible turbomachinery, design, analysis, meanline, CFD

Abstract in lingua italiana

In questa tesi un metodo per progettare e analizzare turbomacchine assiali reversibili è presentato. Le turbomacchine reversibili possono funzionare sia come compressore che come turbina, in base alla direzione del flusso. La loro applicazione è intesa per un sistema Pumped Thermal Energy Storage (PTES), che sfrutta un ciclo Brayton chiuso e reversibile. L'utilizzo di macchine reversibili permette la semplificazione dell'impianto e una potenziale riduzione dei costi. L'obiettivo di questa tesi è doppio: innanzitutto realizzare un progetto preliminare di queste macchine non convenzionali attraverso un approccio alla linea media appositamente sviluppato, successivamente verificare la validità del metodo usato tramite simulazioni di fluidodinamica computazionale (CFD). Prendendo come riferimento un PTES con potenza netta in carica di 10 MW, il progetto della modalità compressore, la modalità più critica, è ottenuto tramite un codice alla linea media, seguito dall'analisi della modalità turbina. I codici sono stati validati tramite simulazioni CFD 3D. È risultato che le performance integrali del compressore deviano da quelle predette dal codice dell'1%, mentre errori significativi sono risultati comparando la modalità turbina. La modalità turbina mostra incidenza negativa su tutte le schiere, che si combina alla piccola deflessione imposta dalla modalità compressore, e risulta in scarse capacità predittive dell'approccio alla linea media e a basse efficienze. Diversi fluidi di funzionamento e diverse architetture delle macchine sono stati testati. Argon aumenta il costo per gli scambiatori di calore, ma permette un minore rapporto di compressione e quindi un minore numero di stadi rispetto all'azoto. Il rapporto di compressione in carica è di 2.08, rispetto a 2.95 per azoto, mentre per la scarica è 2.35 rispetto a 3.33 per azoto, permettendo 8 stadi per le macchine ad argon, mentre 12 per quelle ad azoto. Le macchine con palette direttrici all'inlet e all'outlet mostrano una maggiore efficienza e una costruzione più semplice rispetto alle macchine composte da soli rotori e statori. Efficienza isoentropica di compressione per carica e scarica è risultata 89.6% e 84% per argon, mentre 86.7% e 84.9% per azoto. Le modalità turbina sono state analizzate usando la stessa portata, ma la pressione obiettivo in uscita non è stata raggiunta a causa dell'eccessiva incidenza negativa, che ha portato i rotori ad agire come compressori. Ciononostante, le macchine ad argon hanno mostrato minore incidenza e un più alto rapporto di espansione.

Parole chiave: Turbomacchina reversibile, progetto, analisi, linea media, CFD

Contents

1 | Introduction

More and more in the following years, renewable energy sources will play an increased role in the energy mix for Europe and for the entire world. The European Union (EU) has set different targets and plans to reduce greenhouse gas emissions by 55% by 2030 and to become the first climate-neutral continent by 2050 [1]. In order to make this possible, energy scenarios have been proposed, in which not only the share of renewable sources is increased, but also the total energy consumed has to be decreased. The proposed policies are shown in Figure 1.1, alongside the 2019 energy mix [2].
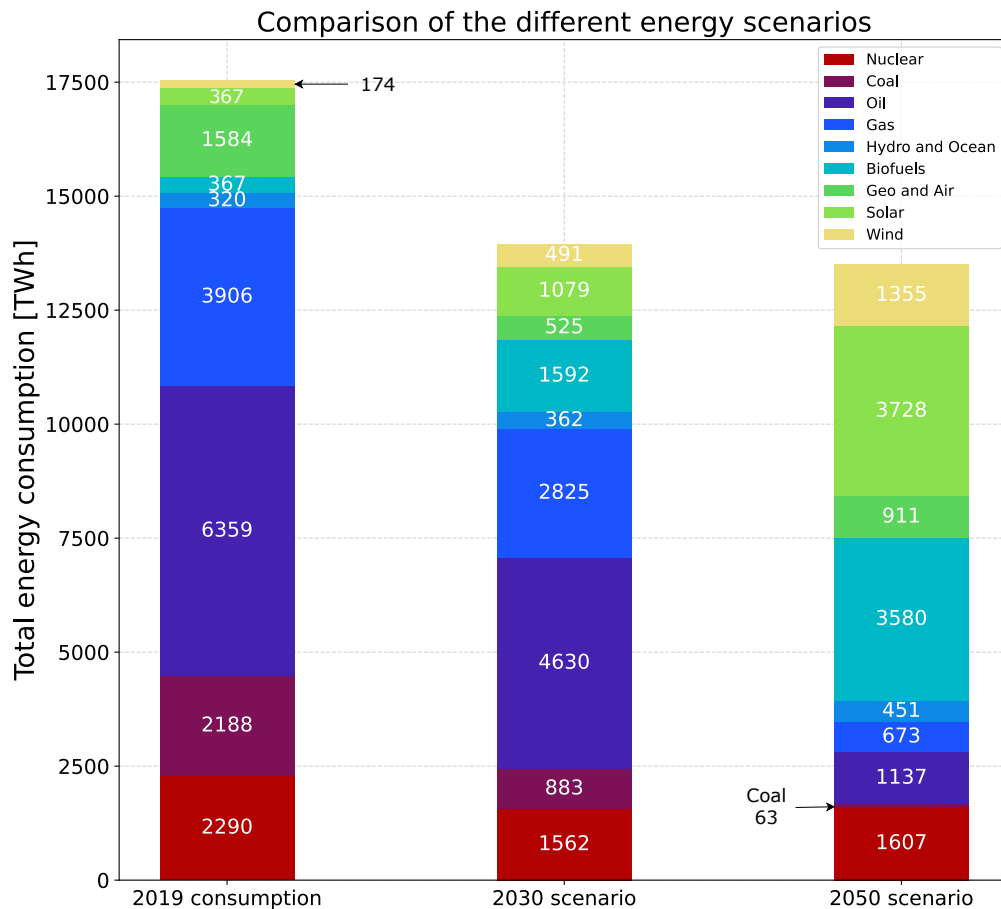

Figure 1.1: Energy scenarios for net-zero emissions compared with 2019 consumption.

The share of renewable sources was 15.3% (2670 TWh) in 2019, while it is going to increase to 29% (4049 TWh) by 2030 and to 74% (10025 TWh) by 2050.

With the increase of renewable sources use, there's also an increase in the variability of the energy that can be supplied: solar energy is available only during daylight hours and wind intensity and direction is not always the predicted one. An example of the daily energy demand and its source for Italy is shown in Figure 1.2 [3].
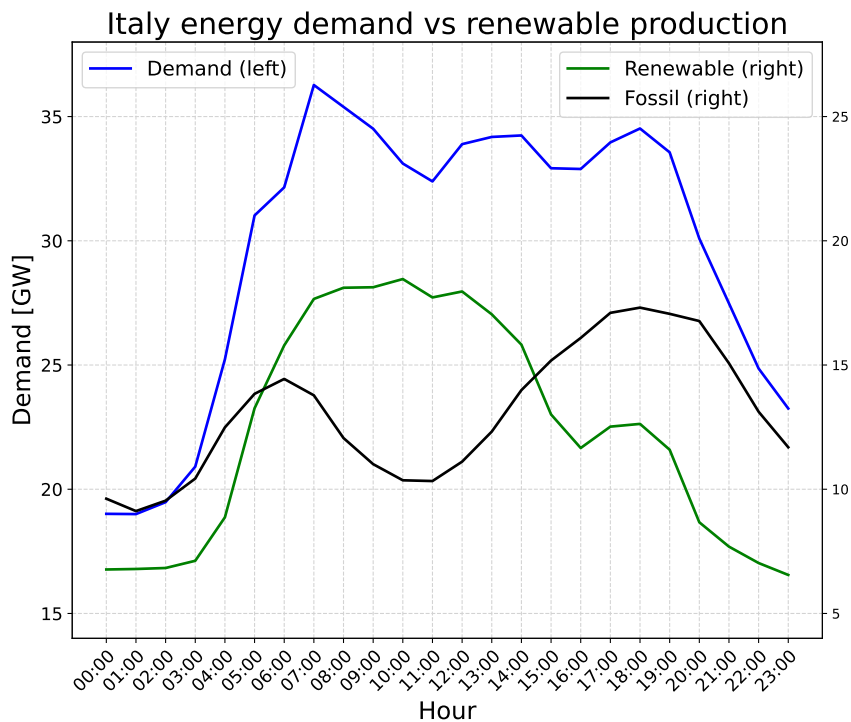

Figure 1.2: Daily demand and source of energy in Italy.

It can be seen how renewable energy production is not constant during the day, mainly because of daylight hours regarding solar energy, therefore peak of demand must be met with non-renewable sources. If the role of renewable energy sources, with their variability, has to increase consistently, it might happen either the production of energy exceeds the demand, resulting in wasted energy, or the opposite, i.e. additional power is requested. A solution for decreasing the dependency on fossil fuels to cover peak-power demand is to store the surplus of energy generated with renewable energy sources and then release it when necessary. This is the reason why energy storage becomes indispensable for reaching the above-mentioned goals. European Association for Storage of Energy (EASE) estimated that in order to comply with the above-mentioned targets, 200 GW of energy storage systems are needed by 2030 and 600 GW by 2050 [4].

1.1.   Energy Storage Systems

Different techniques for storing energy are possible, each with different characteristics in terms of discharge time, energy and power density and the form of energy that is stored. An overview of where these techniques fall for their discharge time and power ratings is shown in Figure 1.3.
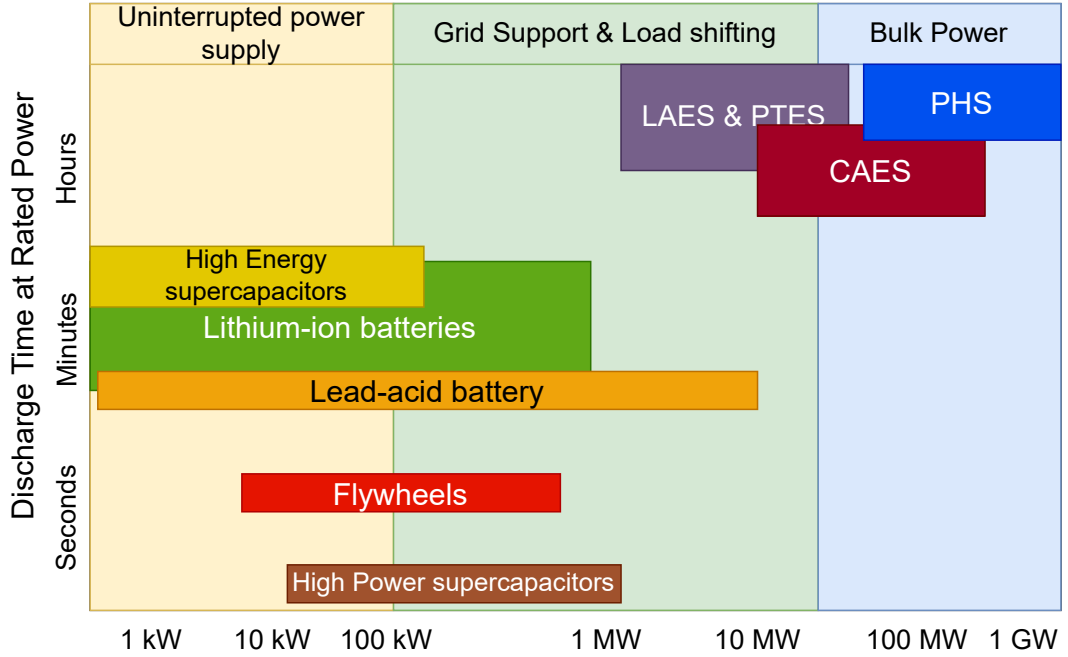

Figure 1.3: Comparison between different storage techniques [5].

Aim of this work is to study an application for large timescale and high power energy storage, therefore systems like batteries, flywheel and supercapacitors, which are suitable for low discharge time and low power are not considered.

The applications compared are characterised by the presence of a working fluid that circulates in the plant, which is responsible for the energy transfer. The most significant parameters used for comparing these systems are:

1. energy density ρ_E, the ratio between the energy discharged W_{dis} and the volume of the storage $\Sigma V_{storages}$:

$$\rho_E = \frac{W_{dis}}{\Sigma V_{storages}} \tag{1.1}$$

2. power density ρ_P, the ratio between the power discharged $\dot{W}_{dis}$ and the maximum

volumetric flow rate of the working fluid $\dot{V}_{max}$:

$$\rho_P = \frac{\dot{W}_{dis}}{\dot{V}_{max}} \tag{1.2}$$

3. cost per unit energy, in $\dfrac{\$}{kWh}$

4. cost per unit power, in $\dfrac{\$}{kW}$

5. round-trip efficiency RTE, the ratio between the energy that can be discharged $\dot{W}_{dis}$ and the energy accumulated during charge $\dot{W}_{ch}$:

$$RTE = \frac{W_{dis}}{W_{ch}} \tag{1.3}$$

High ρ_E and ρ_P is beneficial for the compactness of the plant, reducing the footprint and costs for materials. Systems with high power cost present long discharge time, therefore are used for covering the baseline demand, while plants with high energy cost are preferred for fast response in order to cover temporary peak demands. A higher RTE means that the system is able to provide higher energy when discharging.

Pumped Hydroelectric Storage

Pumped Hydroelectric Storage (PHS) works as a traditional hydroelectric plant, with water in the upper reservoir which is discharged to the lower reservoir to generate electricity. During off-peak demand or in case of surplus, water is pumped from the lower reservoir to the upper one, therefore storing potential energy. A schematic of the plant is shown in Figure 1.4
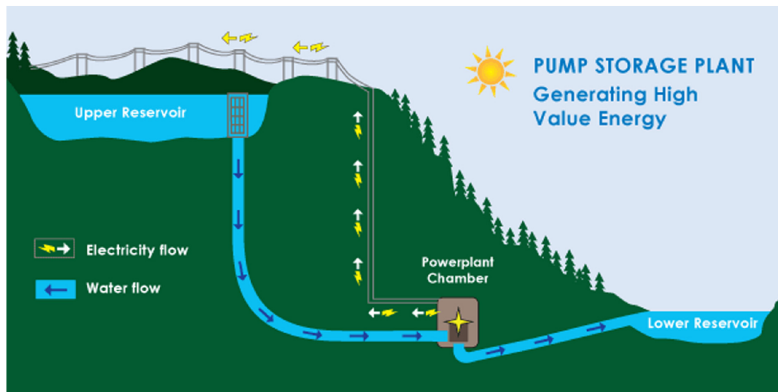

Figure 1.4: Pumped Hydroelectric Storage. [6]

This type of plant makes up for over 99% of the energy storage systems exploited in the world [5], but it is limited by the geological features needed for the installation area.

Compressed Air Energy Storage

Another type of large scale energy storage system is compressed air energy storage (CAES), which compresses air during surplus of power and stores it in vessels or underground caverns [6]. It consists of the second major energy storage system used [5], alongside PHS. The compressed air is then heated up and expanded in a turbine to recover the energy. The heat of compression can be either discharged to the environment or stored in a thermal reservoir. If available, the stored heat is used to reduce the heat supplied to the compressed air before the expansion.

Liquid air

Liquid air energy storage (LAES) stores energy in the form of thermal energy. Air is first compressed, then cooled down in two stages, first transferring heat to a hot store, successively to a cold store. The air is then expanded back to environmental pressure through a throttle valve, obtaining a two phase mixture of liquid and gaseous air. The liquid air is stored in cryogenic tanks, while the gaseous air is sent back into the cycle. During discharge, the liquid air is first pumped to high pressure, then heated by the cold and hot store, and finally drives a turbine to generate electricity [7].

Pumped Thermal Energy Storage

Pumped thermal energy storage (PTES) stores energy in the form of heat, which is pumped from a cold reservoir to a hot one and vice versa through a closed reversible Brayton cycle [8]. Heat is stored in the form of sensible or latent heat in dedicated tanks (charge phase) using the Brayton cycle as a heat pump. In the discharge phase, the Brayton cycle works as a power cycle to produce electricity. Advantages of PTES with respect to other solutions is a easy scalability for large-scale applications, since the energy content stored is a matter of size of the reservoirs and a low cost per energy, comparable with the one of PHS.

A summary on the main parameters chosen for compare the above-mentioned energy storage systems is shown in Table 1.1.

Table 1.1: Summary on Energy Storage Systems.

Storage system	ρ_E [Wh/L]	ρ_P [W/L]	$/kWh	$/kW	RTE [%]
PHS [6]	0.5-1.5	1000-2000	5-100	600-2000	65-87
CAES [6]	3-6	/	2-50	400-800	50-89
LAES [9]	50	/	260-530	/	40-85
PTES [7]	46	/	15	470	55-70

These systems all present a low cost per energy stored and a high cost per power delivered, therefore they benefit from large-scale sizing. That is why they are suitable for covering the baseline demand, which can be more easily predicted, rather than peak-power demand. Despite working for similar power range and purposes, they present differences that can lead to opt for a system rather than another. Systems like LAES and PTES are free from the requirement of specific geological features of the site, allowing for scaling potential. Moreover, they require only well-known components, such as heat exchangers, compressors and expanders.

Focus of this work is on PTES system due to the advantages just delineated and to the higher maturity of the technology.

1.1.1. PTES

The ideal closed, reversible Brayton cycle exploited is composed by 2 isoentropic transformations (compression and expansion) and 2 isobaric heat exchanges, as shown in Figure 1.5, in the enthalpy (h) - entropy (s) plane.
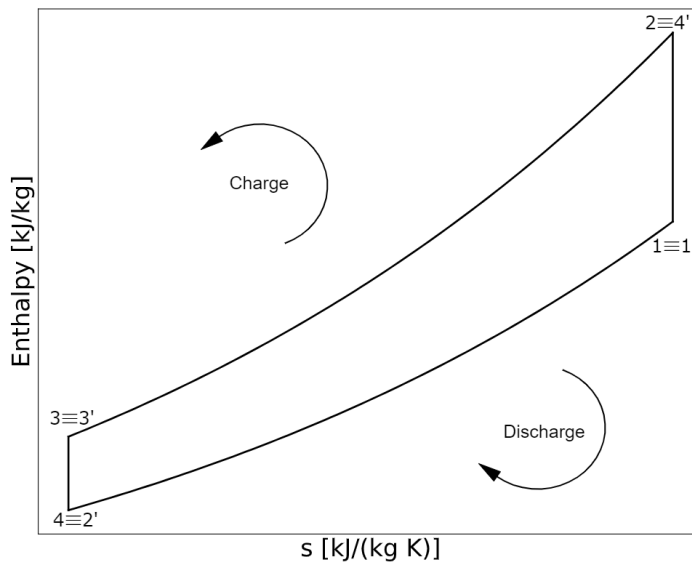

Figure 1.5: Ideal thermodynamic cycle of PTES.

The numbers without apostrophe representing the charge cycle points, while the ones
with apostrophe representing the discharge cycle points.

The 2 isobaric transformations are carried out through 2 heat exchangers, while the com-
pression and expansions can be carried out by either reciprocating devices or turboma-
chines. A captivating feature of this type of plant is that ideally the RTE is 1, assuming
isoentropic efficiency of the machines as 1 and no pressure loss in the heat exchangers. In
reality, the cycle between charge and discharge mode differs, as shown in Figure 1.6.
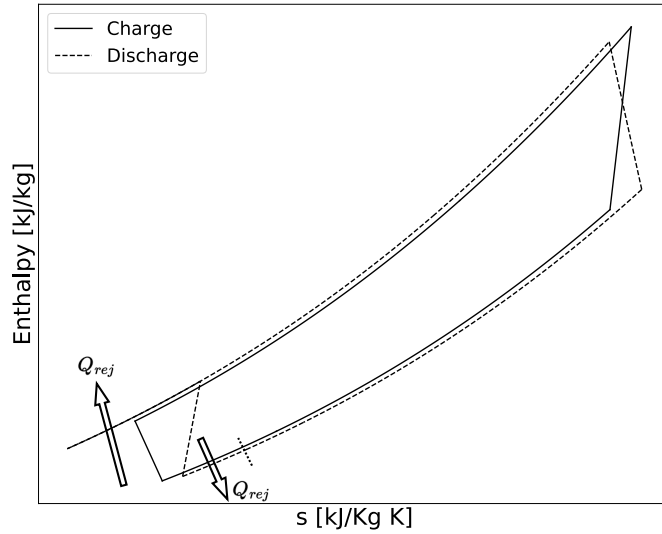

Figure 1.6: Real charge and discharge cycle for PTES application

The first disparity than can be noted is the different pressure and temperature levels
between charge and discharge mode. This is due to the irreversibilities of the machines
and pressure losses in the heat exchangers (HE) [10]. In this work, it is considered the
same pressure ratio β for the hot machines, i.e. compressor in charge mode (CC) and
turbine in discharge mode (TD). Due to the pressure losses in the HE, the compressor in
discharge mode (CD) has to provide a higher β than the one needed for the TD to close
the cycle. The same holds for charge mode, where the β available for the turbine (TC)
is lower than the β provided by CC. Moreover, all the irreversibilities generate heat that
has to be rejected to the environment. In this work, two heat rejections are carried out
in the discharge cycle.

The driving factor in energy storage systems is, as Laughlin stated, "safety, low cost and
high efficiency, in this order" [8]. A way of reducing a big part of the costs [7] is to exploit
the quasi symmetry of the thermodynamic cycle to use reversible machines, which can
work both as a compressor or as an expander, depending on the functioning mode. Focus
of this work is to study the feasibility of reversible turbomachinery, that can work both as
a compressor and as a turbine. In this way, only half of the machines are needed, reducing

the costs and simplifying the scheme of the plant, as shown in Figure 1.7.

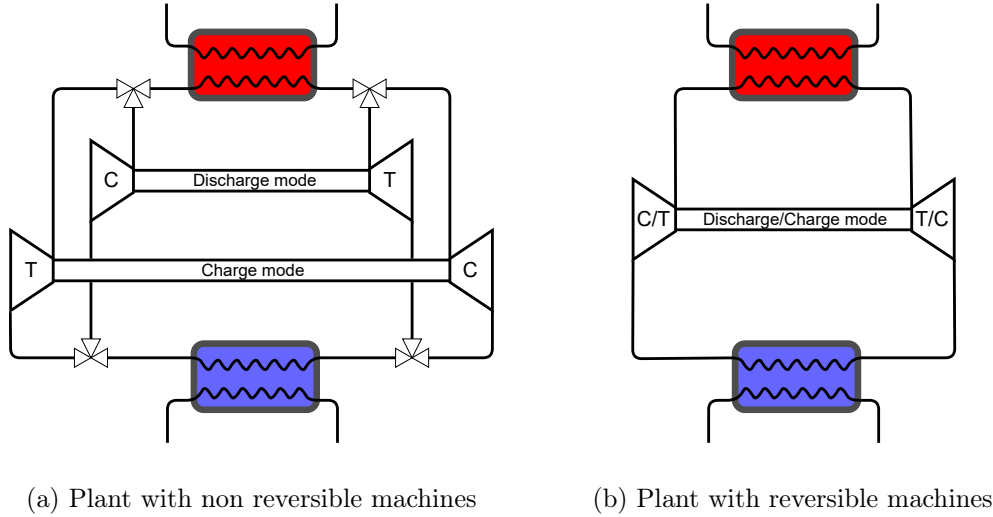(a) Plant with non reversible machines   (b) Plant with reversible machines

Figure 1.7: Plant schemes for non reversible and reversible turbomachines.

Being a closed cycle, it presents two main advantages. The first is that the pressure level of the cycle can be chosen freely, since it is not constrained by the environmental pressure. The pressure level can therefore be increased, leading to a more compact design, increasing ρ_E. The second is that the working fluid can be chosen freely. In this work, a comparison between two working fluids is performed: argon and nitrogen. Ar, being monoatomic, has a higher heat capacity ratio than N_2. This means that the same temperature ratio, which is linked to the power generated, can be achieved with a lower pressure ratio. Therefore, the number of stages can be reduced, leading to a more compact design. An example of the difference in the pressure ratio vs temperature ratio for the two fluids can be seen in Figure 1.8a, while the difference in the number of stages is shown in Figure 1.8b.

(a) Pressure ratio comparison.   (b) Number of stages comparison.
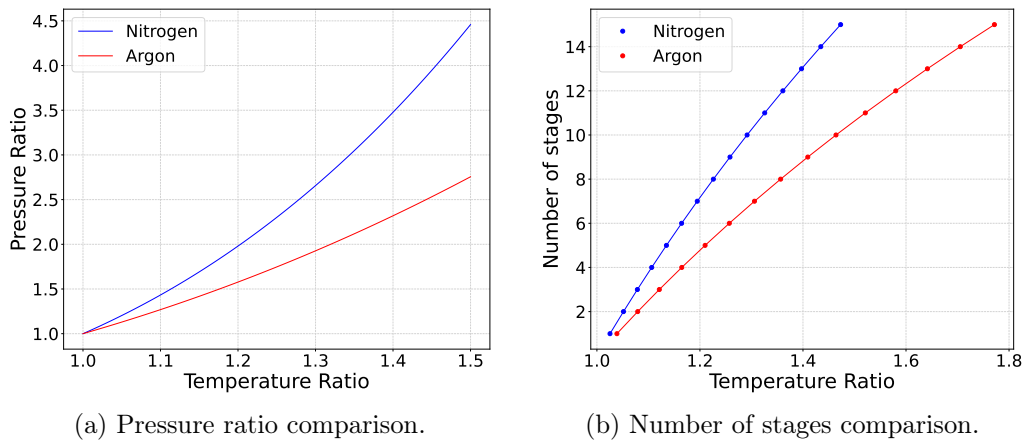
Figure 1.8: Pressure ratio and number of stages comparison for nitrogen and argon.

On the other hand, N_2 has better thermal conductivity properties, leading to more compact, therefore less expensive heat exchangers.

1.2.   Reversible Turbomachinery

Compressor and turbine work in opposite way: turbines accelerate the flow, deflecting it towards tangential direction, while compressors decelerate the flow, bringing it towards axial direction. In the case of strong deceleration, however, it can be present flow separation due to the adverse pressure gradient, which can bring the blade to stall. Therefore the rate of deceleration (and so deflection) of compressors is much lower than the one of turbines.

The aim of this work is to design a machine that optimises both compressor and turbine mode, hence traditional design techniques such as the Smith chart cannot be used. The design procedure has to be created from scratch, and it is decided to use a meanline approach for the calculations of the two functioning modes. This method allows to calculate flow and thermodynamic quantities at blade midspan and extending them to the whole section, ignoring circumferential and radial effects, such as radial equilibrium. In this way the behaviour of the machine is predicted at a global level for every inlet and outlet station of every cascade, ignoring local effects, such as tip clearance vortexes.
Meanline calculations are integrated with computational fluid dynamics (CFD) calculations, performed in the first place to validate the meanline code, then to visualize the whole flow field and to derive more detailed considerations on the 3D behaviour of the machine in both operational modes.

The main obstacle in the design of such machines is the non symmetric thermodynamic cycle between charge and discharge mode. This causes the pressure and temperature conditions at inlet and outlet of the corresponding machines to be different. It has also the effect of not allowing a repeating stages approach for both operating modes. Considering repeating stages for compressor mode, the passage height changes to keep the axial velocity constant. The variation in passage area depends on the change in density, thus pressure, given by the work exchanged. In turbine mode, the work exchanged is not the same, therefore the density does not change accordingly to the passage area. In this way, the axial velocity cannot be constant for both operating modes [10] [11], leading to incidence angle values different than design one for one of the two modes.
Harris [11] application for this kind of machine presented an average pressure ratio per stage of 1.1, therefore a similar specification is considered in this work.

Due to these considerations, the compressor mode, which is the most critical one in terms

of fluidynamic, and more influenced by the incidence angle, is designed at its optimum using a repeating stage approach. The turbine mode, instead, is analysed, running the geometry obtained from the compressor calculations backwards to calculate its performance. In this way the compressor works far from unstable operating conditions, such as stall.

Both of the calculations are finally linked through an optimisation routine, which is able to find the geometry that maximises the functioning for both compressor and turbine mode.

Two type of architectures are studied, one composed by only rotors and stators, and another with guide vanes both at inlet and outlet. The latter allows to simplify the design of the machine: the first and last stage of compressor design are avoided, which are more critical, and the machine is composed by only repeated stages.

1.3.   Thesis Organization

The current thesis delineates the design of reversible turbomachinery used in a PTES plant with a meanline approach. Out of the scope of this work is to study all the accessory components of this type of plant, such as the heat exchangers and also the costs.

Other than the introduction, three chapters are present that describe the work performed and one chapter that delineates the conclusions and future works:

- In chapter 2 the meanline analysis of the machines of both compressor and turbine configurations is performed, along with its validation with quasi-3D and fully 3D CFD analysis.

- In chapter 3 the meanline optimisation and outcomes are described.

- In chapter 4 it is detailed the methodology of the CFD analyses of the turbine mode of two classes of machines operating with either argon or nitrogen as working fluid. Such analyses allow drawing some useful considerations regarding the round-trip efficiency of the reversible PTES.

- In chapter 5 the conclusions of this work are outlined, together with suggestions for future works on this field.

2 | Meanline Analysis

The starting point of the flow analysis of the machine is a meanline code. Meanline means that all the flow and thermodynamic parameters are calculated at blade midspan at the inlet and outlet of every cascade, and are extended to the whole section, ignoring radial and circumferential effects, such as radial equilibrium. Losses are accounted also for 3-dimensional effects, such as clearance, end-wall and secondary losses as a global result.

Two codes are developed, one for the compressor and one for the turbine. Since the compressor is the most critical machine in terms of fluidynamic, the compressor meanline code is implemented as a design code, which generates the geometry of the machine given the design operating point, while the turbine meanline code is implemented as an analysis code, meaning that it takes as input the geometry generated by the compressor and runs it backwards to calculate the performance.

The aim of the codes is to predict the machine behaviour through rapid numerical and analytical calculations. The codes can then be coupled to an external optimisation routine, obtaining the geometry that maximises the functioning in both ways of operation (compressor and turbine mode).

2.1. Blade Geometry and Convention

It is necessary to choose a convention for blade angles and velocities, in order to accurately describe the machine functioning. All equations and figures present in this work are related to the conventions described here, unless otherwise specified.
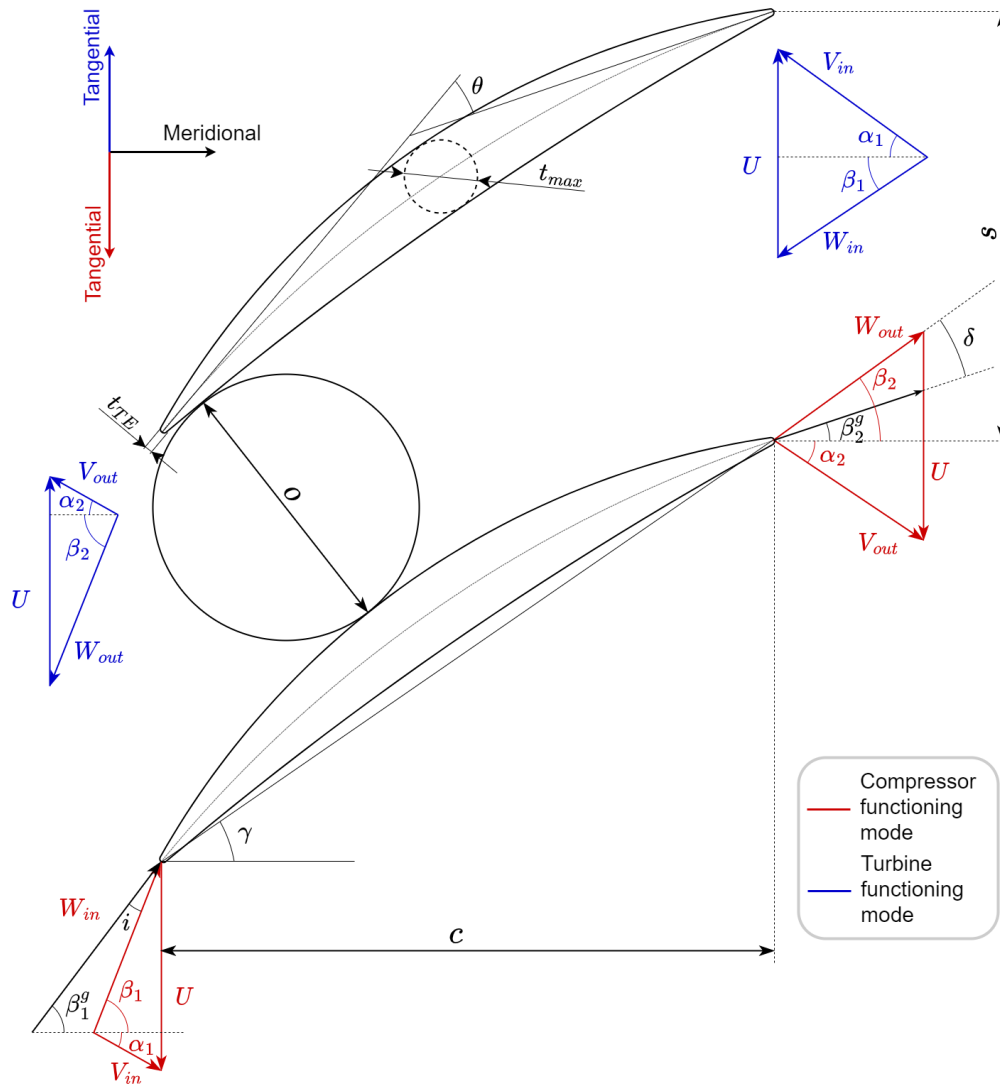
Figure 2.1: Blade conventions for geometrical and flow characteristics

Flow angles are defined from the meridional direction, and are referred to as α for angles in the stationary frame of reference and β in the rotating frame of reference of rotors. Angles are positive if they point in the same direction as the peripheral velocity (U). As flow angles, also velocities can be represented in the stationary frame of reference o in the rotating frame of reference of rotors. Velocity represented in the stationary frame of reference is called absolute velocity (V), while the one in the rotating frame of reference is called relative velocity (W). Velocities can be decomposed in two components: a meridional one (V_m or W_m) and a tangential one (V_t or W_t).

Velocities characterising a blade cascade are linked through each other, composing the so called velocity triangle (VT). By building the VT, all the velocities and flow angles can be linked mathematically.

For the application described in this work, β are always negative, while α are always positive, therefore some angles calculations differ in sign. Characteristics blade parameters are:

- blade angle at inlet β_{in}^g or α_{in}^g

- blade angle at outlet β_{out}^g or α_{out}^g

- stagger angle $\gamma_{rotor} = \dfrac{\beta_{out}^g + \beta_{in}^g}{2}$ or $\gamma_{stator} = \dfrac{\alpha_{out}^g + \alpha_{in}^g}{2}$

- camber angle $\theta_{rotor} = \beta_{out}^g - \beta_{in}^g$ or $\theta_{stator} = \alpha_{in}^g - \alpha_{out}^g$

- chord c

- spacing between blades s,

- solidity $\sigma = \dfrac{c}{s}$

- throat o, defined as the minimum circle that can be inscribed between two blades

- maximum thickness t_{max}

- trailing edge thickness t_{TE}

- aspect ratio $AR = \dfrac{b}{c}$

Blade angles and flow angles do not coincide for reasons explained in subsection 2.2.3, therefore it is defined a incidence angle i and a deviation angle δ which represent this difference, respectively, at the inlet and at the outlet, as shown in Equation 2.1.

$$\begin{aligned}
i_{rotor} &= \beta_{in} - \beta_{in}^g \\
i_{stator} &= \alpha_{in}^g - \alpha_{in} \\
\delta_{rotor} &= \beta_{out}^g - \beta_{out} \\
\delta_{stator} &= \alpha_{out} - \alpha_{out}^g
\end{aligned} \tag{2.1}$$

2.2. Compressor Code

A new code is started from scratch, in order to better suit what the aim of the machines is. This code undergoes two phases during the development of the project:

1. Preliminary performance prediction

2. Optimised machine performance prediction

The second phase will be detailed after the code validation against CFD predictions.

In the first phase the machine is made up of 3 archetypal stages composed by a rotor and a stator: the first with fully axial velocity inlet, the last with fully axial velocity outlet and the middle one represents a repeated stage, with χ of 0.5. The repeated stage assumption allows the code to be scaled to any number of stages in a trivial way, without adding complexity. In Figure 2.2 it is showed an example of the machine in the blade to blade plane and in 3D.
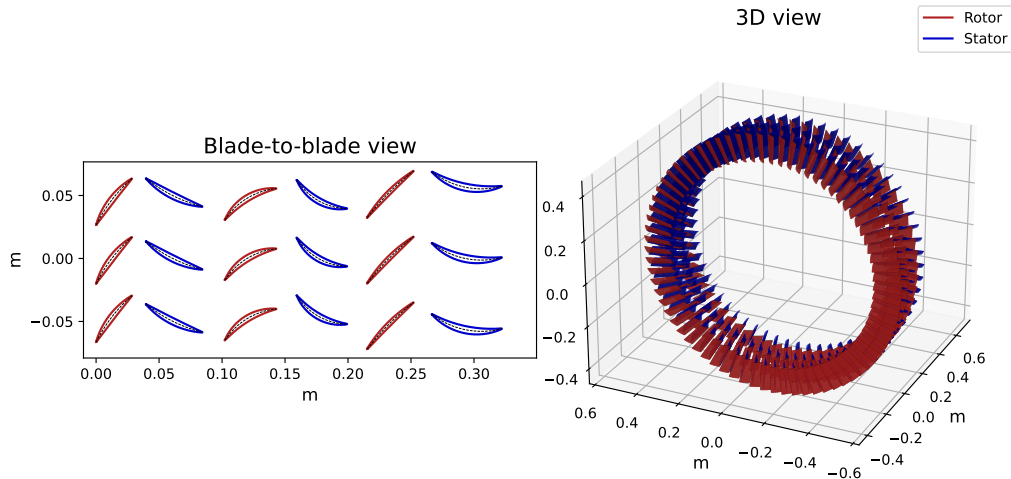

Figure 2.2: Rotors and stators machine Example.

In the second phase, two architectures are compared: one as the first used, and another where inlet and outlet guide vanes are added. This can guarantee that the turbine outlet velocity, in the reversed behaviour, is fully axial and can allow for the use of only repeated stages, removing the necessity for the first and last stage, which are more critical, as explained in section 3.3. An example of the machine in showed in Figure 2.3.
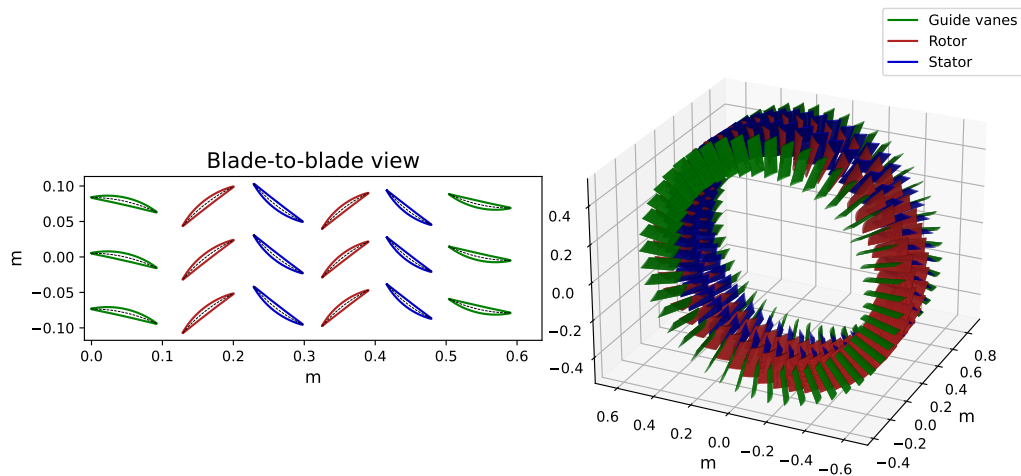
Figure 2.3: Machine with guide vanes both at inlet and outlet.

2.2.1.   Rotors and Stators Machine

Here is described the logic used behind the code when calculating the performance of the machine composed by only rotors and stators.

Being a design code, it is necessary to choose many input, such as adimensional coefficients, geometrical parameters and thermodynamic boundary conditions.

2.2.1.1.   Input

Here a description of all the input required for the functioning of the code are presented.

Thermodynamic BC

The required thermodynamic input are:

- Working Fluid

- Inlet Total Pressure

- Inlet Total Temperature

- Outlet Total Pressure (or Pressure Ratio)

The code is being written in order to run with general equations of state, which are not limited to the type of fluid. Fluid properties are calculated through CoolProp library, which implements state of the art equations of state for characterizing the fluid behaviour. Inlet and outlet total pressure, along with inlet total temperature, describe the operating conditions of the machine, taken from the thermodynamic cycle of the plant. The outlet total temperature is not given because it is a consequence of the machine efficiency.

Adimensional coefficients

Adimensional coefficients are a way to reduce the size of the design space of the machine. They are based on the observation that the behaviour of different machines can be characterized by the same adimensional coefficients. The adimensional coefficients required are:

- Work coefficient λ

- Flow coefficient ϕ

- Reaction degree χ

The work coefficient is defined as $\dfrac{l}{u^2}$, where $l = U(V_{tout} - V_{tin})$, and it is a measure of the deflection of the stage, and so how loaded it is. The flow coefficient is defined as

$\dfrac{V_m}{u}$, evaluated with the inlet velocity for compressor mode and the outlet one for turbine mode. Finally, the reaction degree is $\dfrac{\Delta h_{rotor}}{l}$, and represents how the rotor is loaded with respect to the stator.

For the middle stages λ and χ are not provided because the work coefficient is a consequence of the overall enthalpy rise, given the specified pressure ratio, as explained more deeply in section 2.2. The reaction degree is set to 0.5 to comply with the repeated-stage requirements. The flow coefficient has to be given for all the stages.

Geometrical and operating parameters

Geometrical parameters are required to define the size of the machine, both in dimensional and adimensional form. The quantities to be chosen are:

- rpm of the machine

- Mean diameter of the machine D_m

- Number of stages N_{st}

- Tip clearance of rotors τ

- Solidity σ

- Reynolds number (based on chord) Re_c

- Blade profile

- Maximum thickness to chord ratio $\dfrac{t_{max}}{c}$

- Edge thickness to maximum thickness ratio $\dfrac{t_{TE}}{t_{max}}$

- Mass Flow Rate $\dot{m}$

Since this type of machine has to be linked with the electric grid, a rotational speed of 3000 rpm is assigned in this thesis unless otherwise specified.

Reynolds number based on chord is defined as $Re_c = \dfrac{\rho V c}{\mu}$ and it is used to determined the chord length.

The blade profile chosen is a double circular arc (DCA) due to its fore-aft symmetry, which is suitable for both flow directions.

The final parameters required to define the blade shape are the thickness-to-chord ratio, and the ratio between the edge thickness and the maximum thickness. The default values

for these two ratios are 0.1, but as is explained in further on, it may cause problems in the creation of the blade geometry.

Finally, the mass flow rate in not a dimensional parameters per se, but it influences the passage area and so the blade height, since density and inlet velocity are calculated respectively through thermodynamic and adimensional parameters.

2.2.1.2.   Code Development

The code is developed with Python, a high level language program that allows for fast solving of analytical and numerical equations. It is chosen because it is free source and easily interfaceable with other software, as well as having a powerful optimiser.

The entire code is based on a *while* loop that takes an isoentropic efficiency of first guess and keep cycling until convergence is reached, so when the difference between the efficiencies of two consecutive iterations is under a given tolerance. For every loop present in the code an absolute tolerance of 10^{-6} is given so that the calculations are considered accurate. In order to avoid a loop repeating too many times and thus stalling the calculations, it is also given a maximum number of iteration of 50, after which the cycle is concluded. When a loop is not able to reach convergence it indicates a problem of some sort that has to be figured out before considering the results as satisfying.

The general machine described in this procedure is composed by n stages, and so 2n cascades and 2n+1 calculation stations. The indexing is depicted in Figure 2.4, in order to better understand it.
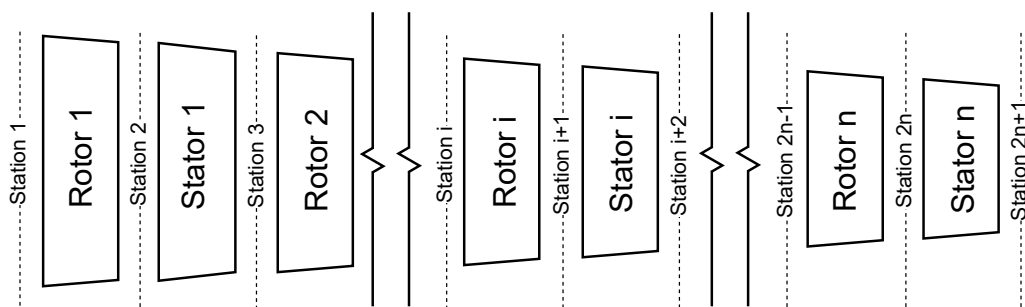
Figure 2.4: Example machine for the code description.

The first step is to divide the enthalpy increase between the stages. The enthalpy rise of the first and last stage is calculated from their work coefficients given as input. The total work is calculated from the isoentropic work l_{is}, which is calculated from the input total-total pressure ratio and from the isoentropic efficiency (which for the first iteration is taken as 1). The remaining enthalpy rise obtained by subtracting the enthalpy jump of

the first and last stage from the total work, can be divided equally between the repeated stages, as shown in Equation 2.2:

$$\Delta h_1 = \lambda_1 \cdot U^2$$
$$\Delta h_n = \lambda_n \cdot U^2$$
$$\Delta h_i = \frac{l_{is}}{\eta_{is}} - \Delta h_1 - \Delta h_n$$
$$(2.2)$$

For the first station, the kinematic quantities are know because the meridional velocity is known from the flow coefficient ϕ_1, so all velocity components can be calculated using VT correlations.

For the thermodynamic quantities, the total enthalpy can be calculated from P_{T1} and T_{T1}, and with the velocity the static enthalpy, as shown in Equation 2.3:

$$h = h_T - \frac{1}{2}V^2 \qquad (2.3)$$

Now, since two thermodynamic parameters are known, all the other properties can be calculated, such as density, pressure and temperature. The last quantity unknown is the blade height, which is obtained imposing the mass conservation:

$$b = \frac{\dot{m}}{\rho V_m \pi D_m} \qquad (2.4)$$

For every successive blade cascade outlet, a *while* loop is necessary, since the entropy increase is unknown and depends from the losses, which depend on some outlet parameters, such as the outlet blade height.

The loop for the outlet of the first rotor (station 2) starts by solving two non linear equations that find the axial velocity and blade height which respect the reaction degree and the mass flow rate imposed, using a first guess entropy, which is the same as the inlet one. Roots of non linear functions in this work are solved through the ScyPy function fsolve. Then, the enthalpy jump calculated with Equation 2.2 is used to find the new total enthalpy and the tangential velocity, using the Euler work formula, as shown in Equation 2.5.

$$h_{Tout} = h_{Tin} + \Delta h$$
$$V_{tout} = V_{tin} + \frac{\Delta h}{U}$$
$$(2.5)$$

Once these values are known, the density, needed together with enthalpy to obtain all the other properties, can be calculated through the conservation of mass and the blade height.

Cascade dimensions, such as chord c, spacing s and number of blades N_{bl} can now be obtained through Equation 2.6. A first guess chord is calculated, then corrected in order to obtain an integer number of blades.

$$
\begin{aligned}
c &= \frac{\mu Re_c}{\rho V} \\
s &= \frac{c}{\sigma} \\
N_{bl} &= \lfloor \frac{\pi D_m}{s} \rfloor \\
s &= \frac{\pi D_m}{N_{bl}} \\
c &= s \cdot \sigma
\end{aligned}
\tag{2.6}
$$

At this point the losses can be calculated using the correlations described in subsection 2.2.3. Losses account for an increase in entropy, calculated form the inlet one. This entropy is now compared to the entropy calculated at the step before, which was obtained starting from density and enthalpy, and the cycle is repeated until these two matches.

For the inlet of the first rotor of the repeated stages (station 3), the absolute angle α_3 is obtained from a non linear function similar to the one used before for station 2, but with the aim of having the reaction degree equal to 0.5. The axial velocity is obtained from the flow coefficient of the repeated stages ϕ_i, and it is used together with α_3 to calculate the tangential one.
After calculating the other kinematic quantities with VT correlations and Equation 2.3 for the static enthalpy, a *while* loop for the losses is performed taking as a first guess s_3 = s_2:

1. ρ_3, P_3, T_3, μ_3, a_3 from real gas properties, starting from h_3 and s_3

2. b_3 from mass conservation

3. c_3, s_3, N_{bl3} from Equation 2.6

4. loss calculation

5. entropy calculation

The new entropy is compared cycle by cycle with the one at the step before, until it

reaches convergence.

For the middle stages the procedure for the rotor and the stator is the same between them, apart from some kinematic quantities calculation. The meridional velocity is constant as deemed to the repeated-stage design strategy, while the tangential velocity differs. For rotors it is calculated from the total enthalpy rise of the stage, while for stators it is the same as the one of the previous stator, as shown in Equation 2.7:

$$
\begin{aligned}
\Delta V_t &= V_{it} + \frac{\Delta h_{Ti}}{U} \\
V_{i+1t} &= V_{it} + \Delta V_t \\
V_{i+2t} &= V_{it}
\end{aligned}
\tag{2.7}
$$

As before, it is now implemented a *while* loop to calculate the kinematic and thermodynamic quantities, as well as losses and entropy, repeated until convergence. This procedure is done for every repeated stage.

The stations missing are now the last three.
Station 2n-1 is calculated in the same manner as station 3, but using the reaction degree imposed as input, station 2n in the same way as station 2 and the last one in the same way as the outlet stator of a repeated stage, but imposing the absolute angle as 0.

Once all the calculations are performed for all the stages and all the quantities, the new compressor isoentropic efficiency can be calculated (Equation 2.8).

$$
\eta_{is} = \frac{h_{Tis,out} - h_{T1}}{h_{T,out} - h_{T1}}
\tag{2.8}
$$

This efficiency is compared with the first guess one. The same convergence criteria of the inner loops are applied in this case, and so the outer loop is repeated until convergence is reached.

The final step in the flow calculations is the radial distribution of velocity, hence angles. It is chosen a free vortex one, in which the product between the radial coordinate and the tangential velocity is constant along the span, as shown in Equation 2.9.

$$
V_t(r) \cdot r = constant
\tag{2.9}
$$

This allows for a higher blade loading at the hub, reducing the bending stresses on the blades, and for a constant l along the span.

All the deflections ϵ at every radial height are checked with the maximum ϵ allowable from Howell limit [12]. The equation for maximum ϵ is reported in Equation 2.10.

$$stators : \epsilon_{max} = \arctan\left(\frac{1.55}{1 + \frac{1.5}{\sigma}} + \tan\alpha_{out}\right) - \alpha_{out}$$

$$rotors : \epsilon_{max} = \arctan\left(\frac{1.55}{1 + \frac{1.5}{\sigma}} + \tan\beta_{in}\right) - \beta_{in}$$

(2.10)

Finally, the actual geometry of the blades can be calculated. The angles considered up until now are the flow angles, but as described in subsection 2.2.3, the blade angles differ because of deviation and optimal incidence. Knowing the correlations (Equation 2.19 for deviation angle and Equation 2.21 for optimal incidence angle), blade angles can be easily calculated with Equation 2.1.

Other blade angles calculated are θ and γ, as defined in section 2.1.
The last parameters needed are its thicknesses: the maximum one and the edges one. As explained before, they are given, respectively, as a ratio to the chord and as a ratio to the maximum thickness itself.

In order to generate the blades profile, a specific function is developed, which takes as input the camber and stagger angles, the chord and the spacing between the blades.

The profile is generated in 4 steps [13], as shown also in Figure 2.5:

1. Generation of the lower profile

2. Generation of the upper profile

3. Generation of the leading and trailing edges

4. Rotation around the center of mass of the stagger angle

(a) Lower profile.   (b) Upper profile.

(c) Leading and trailing edges.   (d) Staggered DCA blade.
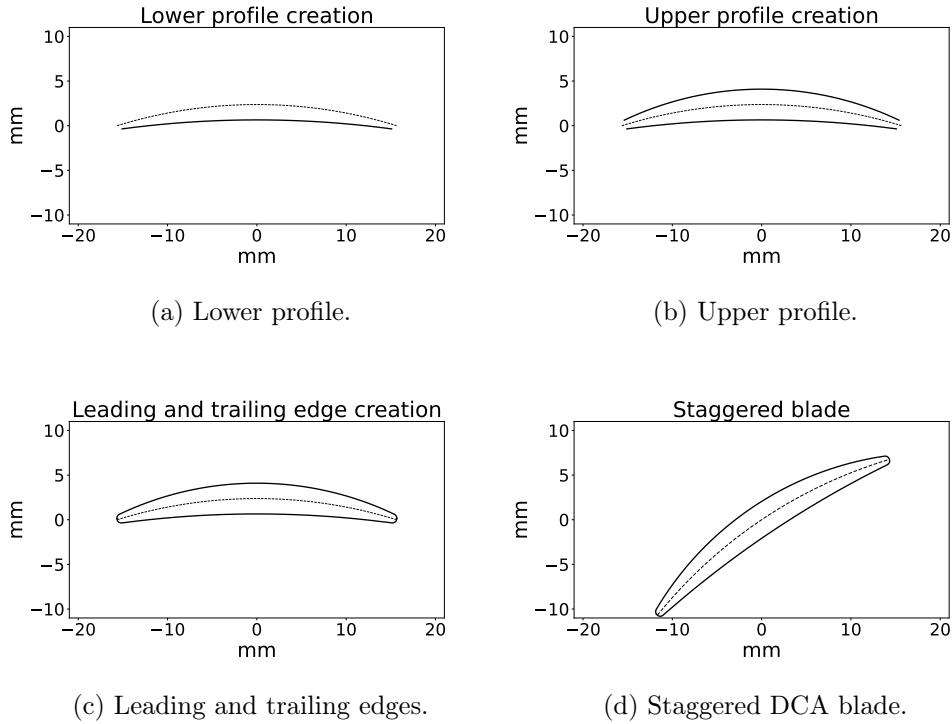
Figure 2.5: DCA blade creation steps.

The blade frame of reference is placed at half chord length and touches the extremities of the camber line. The camber line is a simple circular arc of extension $\left(\dfrac{\theta}{2}, \dfrac{\theta}{2}\right)$, with a radius R_c that allows the camber angle to be the design one.

The first part of the blade to be created is the lower profile, since it may be a source of a drawing problem. It is formed by the equation of a circular arc passing through the leading edge, the trailing edge and the point of maximum thickness in the middle. The formulae for this step are not reported by Aungier [13], the complete formulation is reported in Appendix A.

The problem rises if the point of maximum thickness is below the two edges extremities, as shown in Figure 2.6, that would mean an opposite curvature. This happens in the case of blades with a low deflection, and so low camber angle.
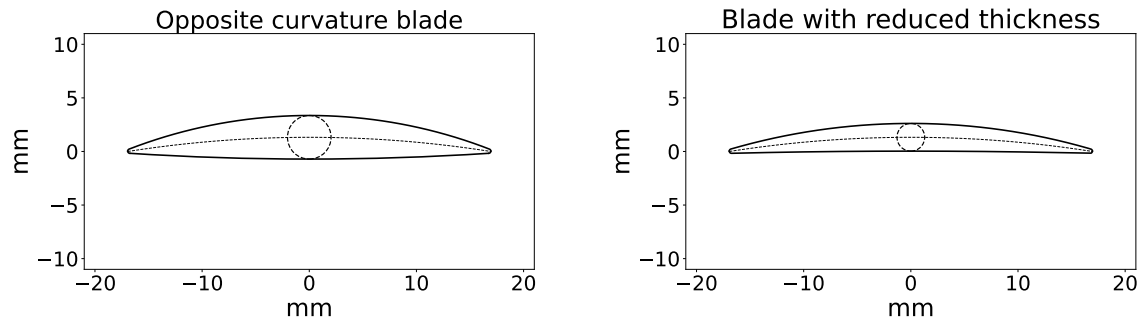
(a) Profile with the opposite curva-
tureĺabelfig:dcaright

(b) Profile with the reduced thickness.

Figure 2.6: Profile correction for thickness.

In this case, the thickness is reduced until the lower profile is flat, hence using the maximum thickness possible.

The next step is the creation of the upper profile, which follows the same path as the lower one, but it doesn't incur in the same curvature problem.

Then, leading and trailing edges are drawn as two circular arcs of radius $\dfrac{t_{TE}}{2}$, in a way that they blend in with the two profiles.

Finally, the blade now obtained is rotated of the stagger angle, using a simple rigid rotation around the center of mass, which corresponds to the center of the camber line, since the profile is symmetric.
This procedure is repeated for every blade at every radial coordinate in which the blades are discretised, in order to obtain the full 3D geometry.

Given that the deviation angle and optimal incidence angle are a function of the thickness, if the latter is reduced due to drawing problems, a final loop on blade angles and blade creation is performed until convergence.

In order to simulate the blades, the meshing software requires the set of points that compose each blade section. The function just described creates the files necessary that the meshing software (Turbogrid) reads as input for creating the blade. These files differ in the structure depending on the type of simulation that has to be performed, but essentially are a sequence of the coordinates of the points that compose each blade profile in circumferential, radial and axial direction. Two type of simulations are performed (quasi-3D and 3D), thus two type of files are needed. 2D simulations cannot be performed since Turbogrid requires at least 2 elements in the radial direction.

For what concerns quasi-3D simulations, the blade profile taken is only a slice at midspan, with a constant thickness of 0.002 m, which is the minimum usable thickness on TurboGrid when creating the mesh. Keeping the height as low as possible guarantees that no three dimensional effects are taken into consideration when simulating.

Actually, as explained more in detail in section 2.4, it was found more accurate to include the flaring also in the quasi-3D simulations. In this case, the blade height at outlet is taken as 0.002m, while the inlet one is in the same ratio with the outlet one as the actual ones are. For 3D simulations, all the stack of profiles are taken for composing the blade geometry.

The last information needed for the meshing software are the hub and shroud. These are composed by the coordinates of the points which describe the casing radial dimensions, while also having the function of limiting the computational domain in axial direction.

A scheme of how the blades' domain is created is shown in Figure 2.7, in which H indicates the hub points, while S the shroud points.
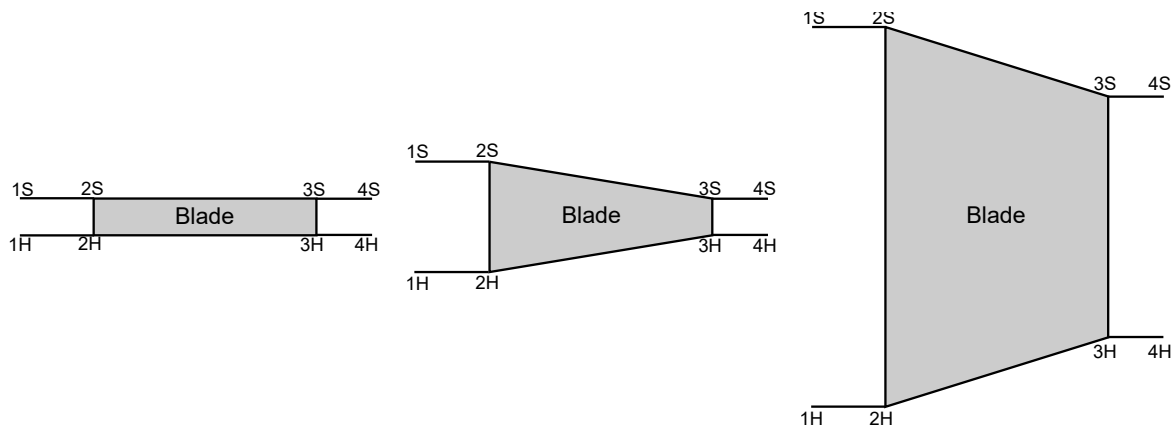
(a) Quasi-3D flat blade for simula- (b) Quasi-3D blade with flaring.   (c) 3D blade.
tion.

Figure 2.7: Meridional view of the different blades used in CFD simulations.

A flow-chart that summarises the calculations performed for this type of machine in shown in Figure 2.8.
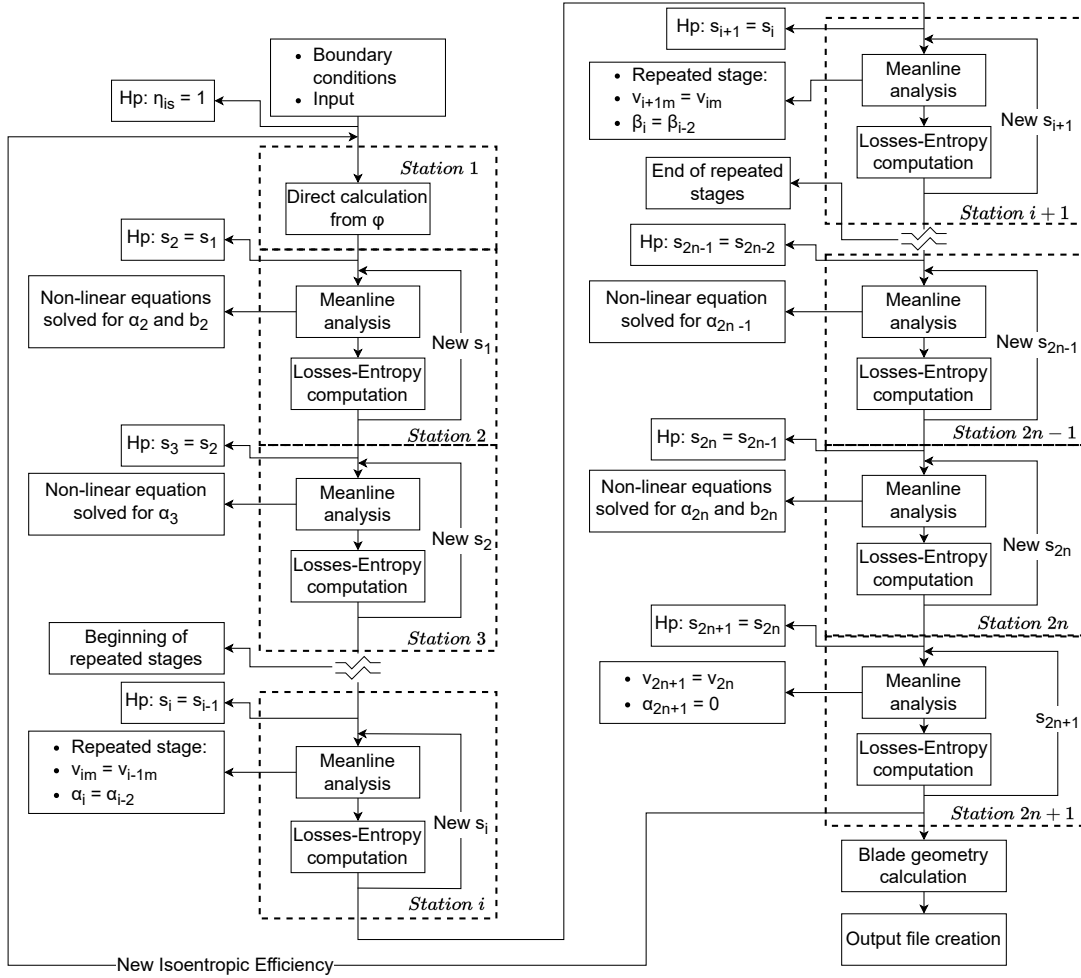
Figure 2.8: Flow chart representing compressor calculations.

2.2.2. Machine With Guide Vanes

The other type of machine requires the use of inlet guide vanes IGV and outlet guide vanes OGV. This is done to guarantee that the outlet velocity in turbine mode is fully axial, by rotating the outlet guide vane (inlet when referred to the compressor mode) in the proper position.

The use of guide vanes allows the use of only repeated stages for the other cascades, enabling a simpler design.

2.2.2.1. Code Development

Given the fact that there are not the first and last stage, the only ϕ required is the one of the middle stages, while no λ or χ are required. Also less σ and Re_c are necessary: one for the IGV, one for the repeated stages and one for the OGV.

Due to the rotation required for the guide vanes, they cannot allow the use of flaring.

Nothing is known in station 1, hence it has to be computed in a loop together with station 2, where the axial velocity is known from ϕ.
Starting from a first guess meridional velocity, which is the same as the one of the repeated stages, the cycle is as follows:

1. calculation of station 1, as done in the previous machine

2. calculation of station 2, as done for station 3 in the previous machine

3. the new axial velocity of station 1 is calculated through mass conservation, using the same blade height as the one of station 2

4. the cycle is repeated until convergence on the axial velocity is reached

Since the IGV deflects the flow towards tangential direction, the deviation and loss correlations used for step 2 are the ones for the turbines. The repeated stages and the OGV performance calculation are performed in the same way as the rotors and stators machine, with the OGV being the same as the last station, with the difference of the constant blade height.

A flow-chart that summarises the calculations performed for this type of machine in shown in Figure 2.9.
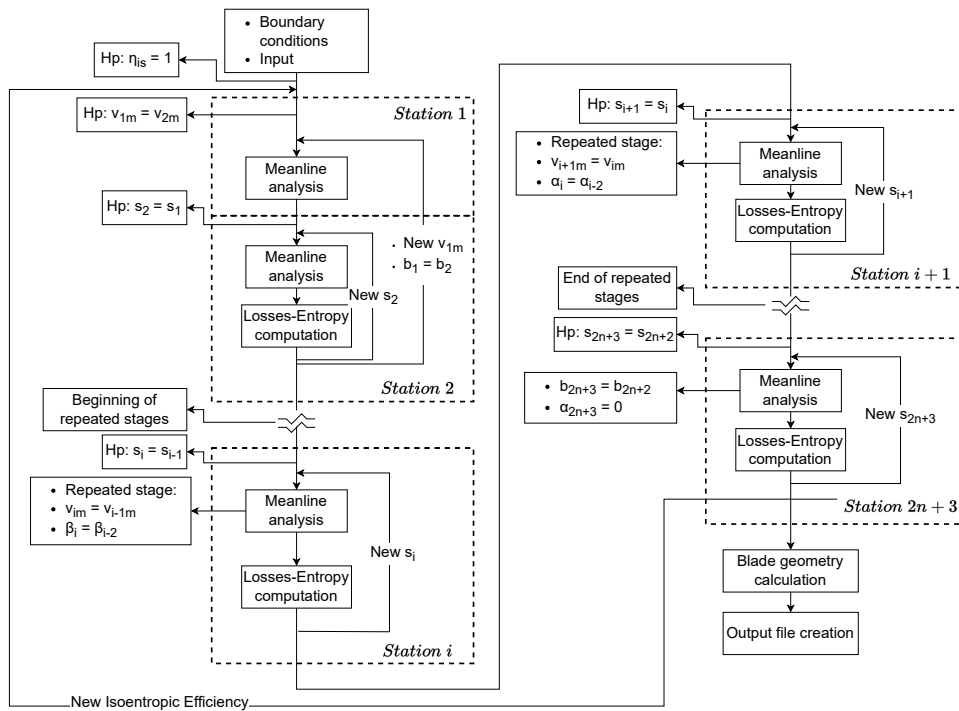
Figure 2.9: Flow chart representing compressor with guide vanes calculations.

2.2.3. Losses and Flow Angle Correlations for Compressors

A meanline code is able to predict the behaviour of the machine if losses and flow angles (hence optimal incidence i_opt and deviation δ) are calculated precisely. Literature is reviewed in order to find accurate correlations that can estimate the above-mentioned quantities.

2.2.3.1. Compressor Losses

When studying turbomachinery, the losses breakdown is carried out in order to better understand which is the most critical cause of losses and act on it. In reality all the loss contributions are linked through each other, but it still holds as an acceptable simplification.

The compressor loss contributions used in this work are:

1. Profile losses $\bar{\omega}_{prof}$

2. Secondary losses $\bar{\omega}_{sec}$

3. Tip clearance losses $\bar{\omega}_{tip}$

4. End wall losses $\bar{\omega}_{ew}$

As explained in chapter 1, this type of application presents low loading, hence shock waves are not expected to happen, therefore shock losses are not considered.

Compressor losses are defined as a total pressure loss relative to the inlet kinetic energy, as shown in Equation 2.11:

$$\bar{\omega} = \frac{P_{Tin} - P_{Tout}}{P_{Tin} - P_{in}} \tag{2.11}$$

Loss correlations are expressed using quantities in the rotating frame of reference when applied to rotating cascades. In case of stators, the mathematical expressions are the same, but every quantity is expressed in the stationary frame of reference, such as absolute velocity V instead of relative velocity W and absolute angle α instead of relative angle β.

Profile Losses

Profile losses include two effects: friction on the blade surface and wake mixing. Lieblein [14] performed experiments on 2D cascades of both NACA-65 and circular arc blades, using a Re_c between $2 \cdot 10^5$ and $4.5 \cdot 10^5$. He obtained the formulation delineated in Equation 2.12:

$$\bar{\omega}_{prof} = 2\frac{\theta_w}{c}\frac{\sigma}{\cos(\beta_{out})}\left(\frac{W_{out}}{W_{in}}\right)^2 \tag{2.12}$$

This expression depends on the the wake momentum thickness θ_w and to the rate of deceleration $\left(\dfrac{W_2}{W_1}\right)^2$. A higher deceleration, as well as a high θ_w, increases the losses. θ_w is correlated to the equivalent diffusion factor D_{eq}, which is the ratio between the maximum velocity on the blade and the outlet velocity. Since the maximum velocity cannot be known a priori, Lieblein [14] developed an expression for the ratio between the maximum velocity and the inlet velocity that fit its experiments, which can than be linked to D_{eq}. The correlations are reported in Equation 2.13.

$$
\frac{W_{max}}{W_{in}} = 1.12 + 0.61\frac{\cos^2\beta_{in}}{\sigma}\left|\tan\beta_{in} - \tan\beta_{out}\right| + 0.007(i - i_{des})^{1.43}
$$
$$
D_{eq} = \frac{W_{max}}{W_{out}} = \left(\frac{W_{max}}{W_{in}}\right)\frac{W_{in}}{W_{out}}
\tag{2.13}
$$

The expression for $\dfrac{W_{max}}{W_{in}}$ includes a contribution from the deflection $(\tan\beta_{in} - \tan\beta_{out})$ and a contribution from the incidence angle $(0.007(i - i_{des})^{1.43})$, when different from the optimum incidence i_{opt}. It can be seen how every factor that increases blade loading increases the losses.

Finally, θ_w is linked to D_{eq} through an expression formulated by Aungier [13], that fits Lieblein [14] experiments, as shown in Equation 2.14.

$$
\frac{\theta_w}{c} = 0.004\left[1 + 3.1(D_{eq} - 1)^2 + 0.4(D_{eq} - 1)^8\right]
\tag{2.14}
$$

This correlation is depicted in Figure 2.10, and it can be seen an abrupt increase in the wake momentum thickness to chord ratio for D_{eq} greater than 2, condition for which the compressor is considered to be stalling [14].
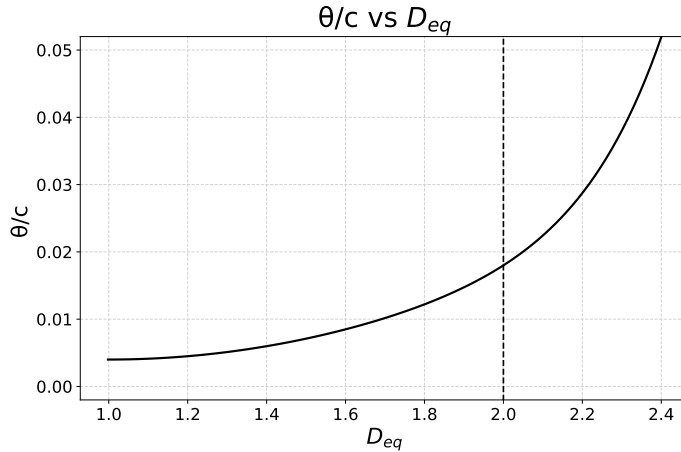
Figure 2.10: Wake momentum thickness vs equivalent diffusion factor.

Secondary Flow Losses

Flow field along the blade span is not uniform due to the presence of the boundary layer at both hub and shroud. The flow in these areas presents lower momentum with respect to the midspan one, therefore including a difference in the deflection imposed and creating vortexes in the secondary plane.

The loss expression implemented in this work is an elaboration of the Howell [15] one, from which is changed how $\bar{\omega}_{sec}$ is calculated. The correlation is based on a drag coefficient for secondary flow loss C_{Ds}, obtained from the lift coefficient of the blade C_L, as shown in Equation 2.15:

$$\bar{\omega}_{sec} = \frac{1}{2} \frac{C_{Ds}\,\rho_{in}\,\sigma\bar{W}^2}{P_{Tin} - P_{in}}$$
$$C_{Ds} = 0.018\,C_L^2 \tag{2.15}$$
$$C_L = 2\cos\bar{\beta}\,\left| \frac{\tan\beta_{in} - \tan\beta_{out}}{\sigma} \right|$$

The use of a drag coefficient implies an incompressible flow assumption, which can affect the accuracy of the model for high Mach number ($M\ /\ M_w > 0.5$).
$\bar{W}$ and $\bar{\beta}$ indicate average values. Also the calculation for the average value of the angle in changed, in order to consider the case where the axial velocity is not constant between inlet and outlet. The expressions for the calculation of the average values are shown in Equation 2.16

$$\bar{W}_a = \frac{W_{a,in} + W_{a,out}}{2}$$
$$\bar{W}_t = \frac{W_{t,in} + W_{t,out}}{2}$$
$$\bar{\beta} = \arctan\left(\frac{\bar{W}_t}{\bar{W}_a}\right) \tag{2.16}$$
$$\bar{W} = \frac{W_{in} + W_{out}}{2}$$

End-wall Losses

End-wall losses are caused by the friction of the flow with the machine casing, so they are strictly correlated with the secondary flow losses. As secondary flow losses, their correlation is based on a drag coefficient for end-wall losses C_{Dew}, but it is now depending

on s and b, as shown in Equation 2.17.

$$\bar{\omega}_{ew} = C_{Dew}\sigma\frac{\cos^2\beta_{in}}{\cos^3\bar{\beta}}$$
$$C_{Dew} = 0.02\,\frac{s}{b}$$

(2.17)

The higher the blade height, the less the boundary layer has an effect on the passage section.

Tip clearance Losses

Tip clearance losses derive from the presence of a gap of width τ on the shroud of the rotors, in order to avoid rubbing during operating conditions. Flow in the clearance is subject to two pressure gradients: pressure side (PS) to suction side (SS) and blade outlet to blade inlet. The pressure imbalance between PS ans SS is proportional to the circulation on the blade, therefore the lift coefficient of the blade. Under compressible flow assumption, as for $\bar{\omega}_{sec}$, $\bar{\omega}_{tip}$ can be expressed from the drag coefficient. These two contributions create vortical structures that contributes to mixing losses downstream of the blade, but also an additional mass flow rate that returns back and has to be compressed again, requiring additional power.

The correlations are taken from Manfredi and Fontaneto [16], who made a revision of the current tip clearance losses present in the literature. Tip losses are made up of two contributions: one is caused by the induced velocities present in the inviscid region of the tip gap (C_{D1tip}), and the other caused by the energy lost in the boundary layer (C_{D2tip}). The expressions are reported in Equation 2.18.

$$\bar{\omega}_{tip} = \frac{1}{2}(C_{D1tip} + C_{D2tip})\frac{\sigma\rho_{in}\bar{W}^2}{P_{Tin} - P_{in}}$$
$$C_{D1tip} = 0.7\frac{C_L^2\tau}{ARb}$$
$$C_{D2tip} = \frac{7C_L^{\frac{3}{2}}\left(\frac{\tau}{b}\right)^{\frac{3}{2}}}{\sigma AR\cos\bar{\beta}}$$

(2.18)

2.2.3.2.   Flow Angles for Compressors

When passing through a blade cascade, the fluid flow is deflected by the geometry of the blade. This deflection, however, cannot be imposed in the same manner throughout the blade passage. Fluid particles close to the wall have to follow the blade shape, but the ones in the middle of the passage tend to keep the original direction due to their inertia.

This causes a decrease in the flow deflection imposed to the flow and therefore a different outlet flow angle than the one imposed by the blade. The deviation increases with blade loading, hence higher deflection, higher incidence angle, higher Mach number, and lower σ.

Compressor blades present also an optimal incidence angle, that corresponds to minimum losses.

Deviation

Deviation correlation is composed by a base deviation of NACA 65 blades with 10% thickness-to-chord ratio and zero camber angle and then corrected for different blade type, different thickness and different camber angle. The equation in shown in Equation 2.19.

$$\delta = K_{sh}K_{t,\delta}(\delta_0)_{10} + m\theta \tag{2.19}$$

K_{sh} is 0.7 for DCA blades, $K_{t,\delta}$ is a correction coefficient for thicknesses different than 10% of the chord, $(\delta_0)_{10}$ is the base deviation for 10% thickness-to-chord ratio and m is a coefficient which depends on σ.

The expressions reported in Equation 2.20 are extrapolated by Aungier [13] from experimental results of Lieblein [17]. The experimental results are instead shown in Figure 2.11.

$$K_{t,\delta} = 6.25 \left(\frac{t_{max}}{c}\right) + 37.5 \left(\frac{t_{max}}{c}\right)^2$$
$$(\delta_0)_{10} = 0.01\sigma|\beta_{in}| + \left(0.74\sigma^{1.9} + 3\sigma\right)\left(\frac{|\beta_{in}|}{90}\right)^{1.67+1.09\sigma}$$
$$m = \frac{m_{1.0}}{\sigma^b} \tag{2.20}$$
$$m_{1.0} = 0.249 + 0.074x - 0.132x^2 + 0.316x^3$$
$$x = \frac{|\beta_{in}|}{100}$$
$$b = 0.9625 - 0.17x - 0.85x^3$$

(a) Zero-camber deviation.

(b) Thickness correction coefficient.

(c) Factor $m_{1.0}$.

(d) Factor b.
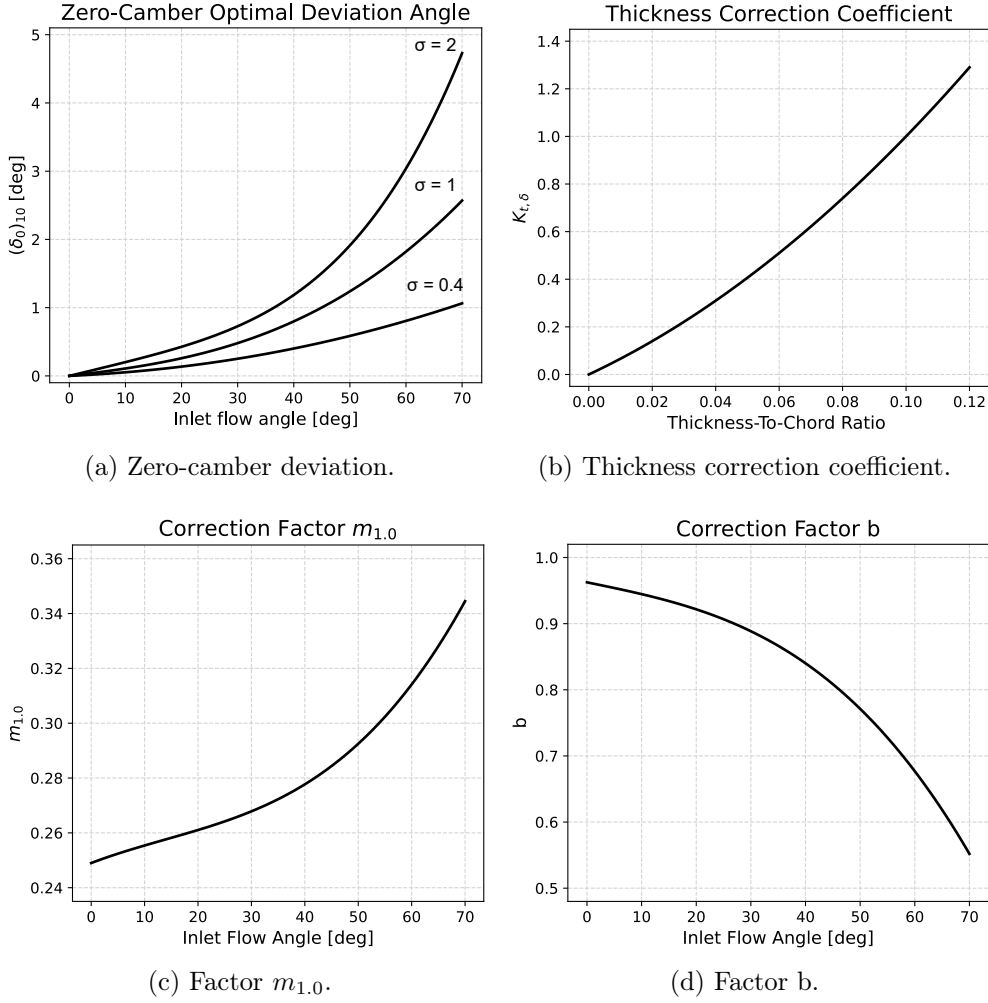
Figure 2.11: Correction coefficients for compressor deviation angle.

Optimal Incidence

Optimal incidence angle is found in the same configuration of experiments for the deviation angle by Lieblein [17]. The expression for the optimal incidence angle in shown in Equation 2.21

$$i = K_{sh}K_{t,i}(i_0)_{10} + n\theta \tag{2.21}$$

The structure of the equation mimics the one for deviation, with a zero-camber incidence for NACA 65 blade having a thickness of 10% with respect to the chord $(i_0)_{10}$ which is corrected by the real thickness using $K_{t,i}$, the blade type using K_{sh} and the real camber angle. K_{sh} is again 0.7 for DCA, while the other coefficients expressions are reported in Equation 2.22.

$$K_{t,i} = \left(10\frac{t_{max}}{c}\right)^q$$

$$q = \frac{0.28}{0.1 + \left(\frac{t_{max}}{c}\right)^{0.3}}$$

$$(i_0)_{10} = \frac{|\beta_{in}|^p}{5 + 46\exp{-2.3\sigma}} - 0.1\sigma^3 e^{\left(\frac{|\beta_{in}|-70}{4}\right)} \tag{2.22}$$

$$n = 0.025\sigma - 0.06 - \frac{\left(\frac{|\beta_{in}|}{90}\right)^{1+1.2\sigma}}{1.5 + 0.43\sigma}$$

As for the deviation, the equations above mentioned are extrapolated by Aungier [13] from Lieblein [17]. The original experimental results are shown in Figure 2.12.

(a) Zero-camber optimal incidence.

(b) Thickness correction coefficient.

(c) Factor n.
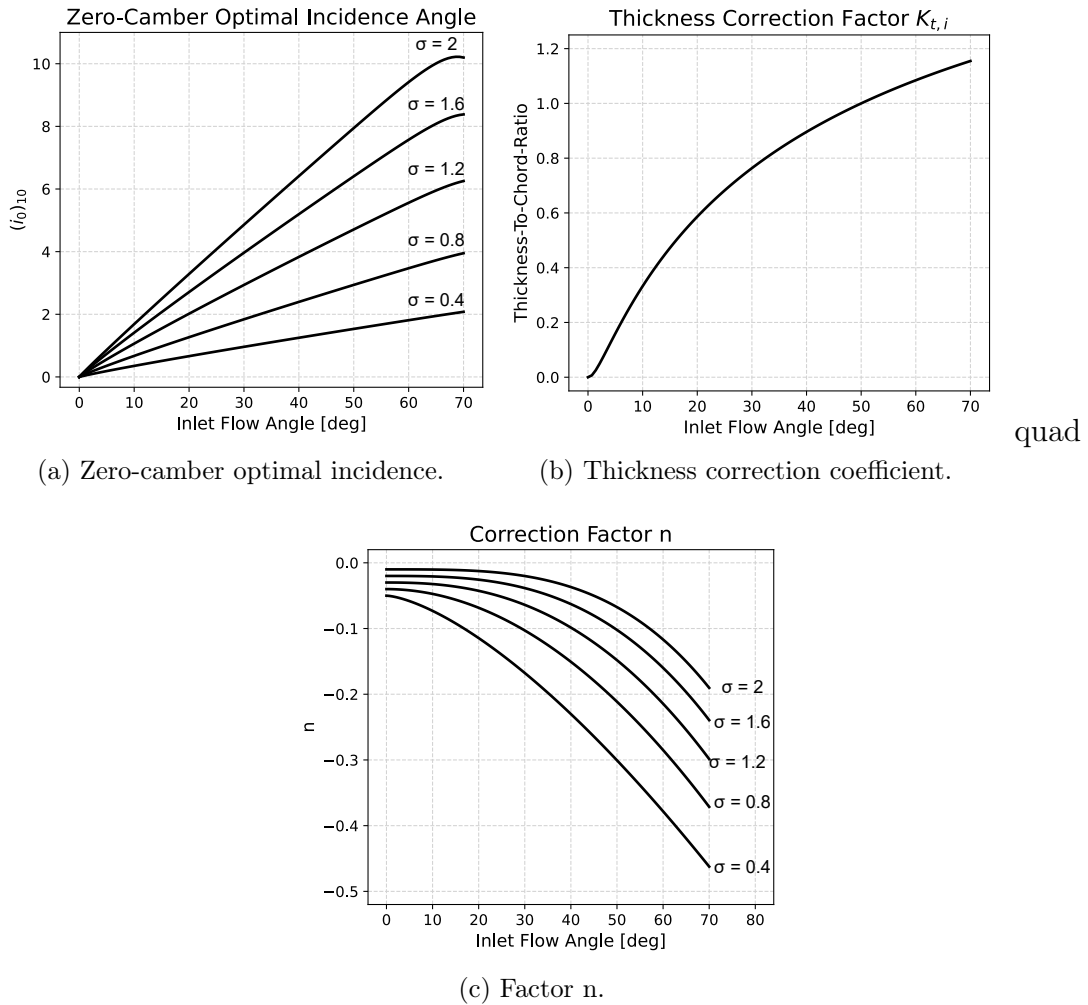
Figure 2.12: Correction coefficients for compressor optimal incidence angle.

2.3. Turbine Code

As mentioned at the beginning of this chapter, the turbine code is an analysis one, thus it takes as input the geometry generated by the compressor and it calculates the performance for the opposite flow direction. Other than the geometry, the only parameters needed are the mass flow rate, the rotational speed and total pressure and temperature at the inlet.

2.3.1. Code Development

Station 1 of the turbine is performed through a loop, using a first guess density (the total one), repeating the following operations until convergence:

1. Axial velocity calculation through mass conservation

2. Kinematic quantities calculation, through VT correlations

3. Static enthalpy calculation through Equation 2.3

4. New density calculation, starting from static enthalpy and entropy

Then, the procedure for a stator and for a rotor is repeated until all the stages are completed, each with its respective frame of reference.

For what concern stators, the incidence is first calculated from the flow angle, since the blade angles are known. Then, a loop is performed, using three first guesses:

1. Outlet angle, taken as the metal one

2. Entropy, taken as the inlet one

3. Axial velocity, taken as the inlet one

These quantities have to converge using, respectively, three equations:

1. Flow angle through blade angle and deviation angle

2. Loss entropy increase

3. Mass conservation

Then, the following operations are carried out in a *while* loop until convergence on all the three assumptions is met:

1. Tangential velocity calculation from the axial one and α

2. Kinematic quantities calculation through VT correlations

3. Static enthalpy calculation through Equation 2.3

4. Thermodynamic quantities calculation from static enthalpy and entropy

5. Mach number calculation

6. Deviation angle calculation, through Equation 2.40

7. Flow angle calculation, through Equation 2.1

8. Losses calculation, through Equation 2.24

9. New entropy calculation

For what concerns the rotors, the procedure is the same, except that the static enthalpy is no more calculated from the total one, but from the rothalpy I, defined as:

$$I = h + \frac{w^2}{2} - \frac{u^2}{2} \tag{2.23}$$

which is constant across a rotor. All this procedure is repeated for every station of the machine, up to the last one.

A flow-chart that summarises the calculations performed for this type of machine in shown in Figure 2.13.
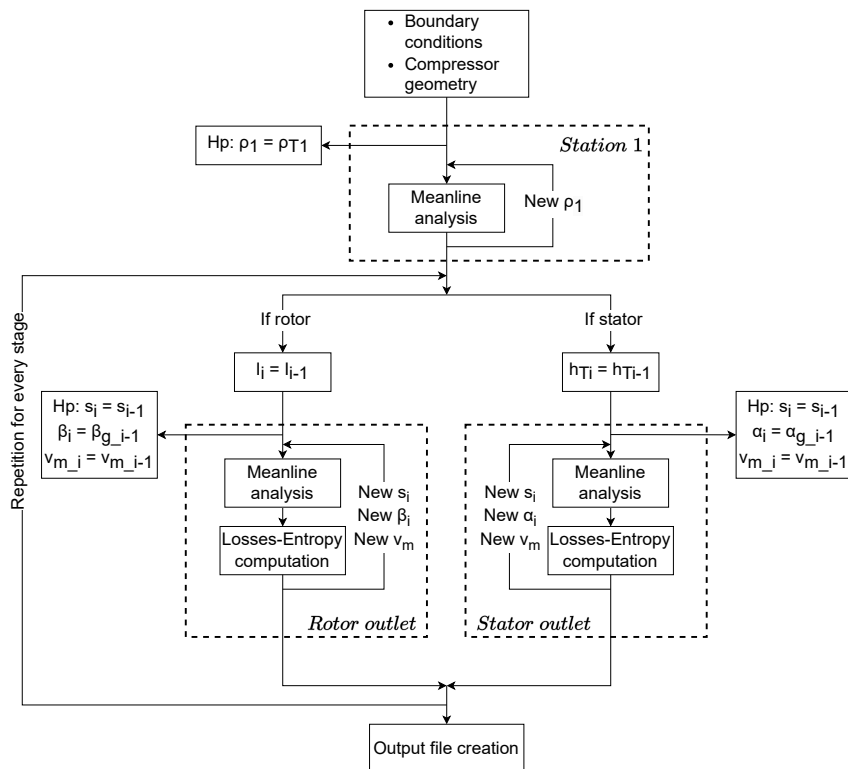
Figure 2.13: Flow chart representing turbine calculations.

In case of the machine with guide vanes, the procedure is the same, except for the possibility of rotating the turbine mode OGV in order to have a fully axial outlet velocity. Compressor mode IGV blade angle is equal to 0 since the flow entering is axial. When reversing the operational mode, this angle becomes the turbine mode OGV outlet angle, which is subject to the deviation angle for turbine mode. Since the deviation angle of turbine is greater than 0, keeping the turbine mode OGV in the same position would cause a swirl angle in the outlet velocity. Therefore the turbine mode OGV has the possibility to rotate in order to compensate for this situation.

For what concerns the code, the calculations are performed in the same manner up to the OGV outlet. In this station, instead of the outlet angle as a first guess, it is taken a rotation of the OGV. Convergence has to be reached on rotation.

A flow-chart that summarises the calculations performed for this type of machine in shown in Figure 2.14.
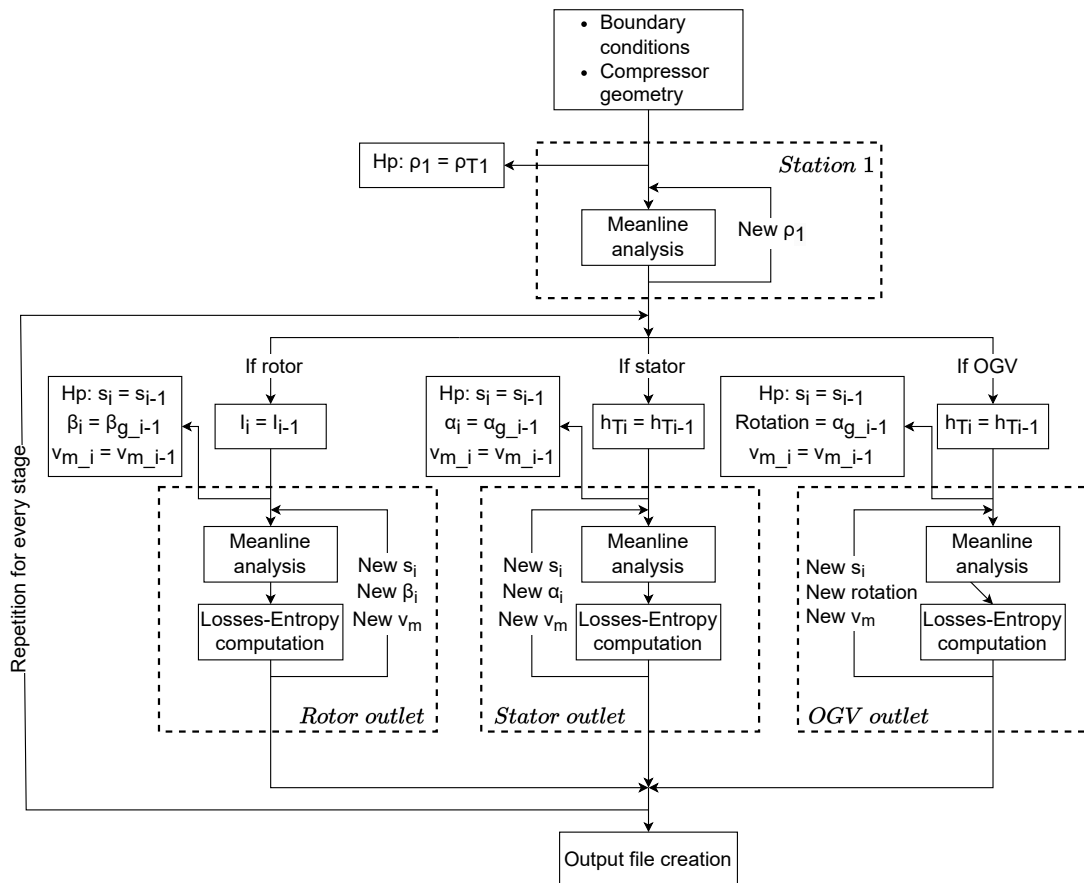
Figure 2.14: Flow chart representing turbine with guide vanes calculations.

2.3.2.   Losses and Flow Angle Correlations for Turbine

In the same way as the compressor, literature is reviewed in order to find accurate correlations that can predict the real behaviour of the machine.

2.3.2.1.   Turbine Losses

As for compressors, loss contributions are split into different independent contributions. The contributions used in this work are:

1. Profile losses $\bar{\omega}_{prof}$

2. Trailing-edge losses $\bar{\omega}_{TE}$

3. Tip clearance losses $\bar{\omega}_{tip}$

4. Secondary and End-wall losses $\bar{\omega}_{sec}$

For the same reasons as compressors, shock losses are not considered.

Total pressure loss coefficient is calculated as the ratio between the total pressure difference between inlet and outlet of the blade and the kinetic energy at the outlet of the blade. The expression is shown in Equation 2.24.

$$\bar{\omega} = \frac{P_{Tin} - P_{Tout}}{P_{Tout} - P_{out}} \tag{2.24}$$

The variables taken in this formulation are the ones referred to the rotating frame of reference of rotors. For what concern stators, the corresponding variables in the stationary frame of reference have to be taken.

Loss correlations are taken from Aungier [18], who has revised the updates from Kacker & Okapuu [19] and Dunham & Came [20] of the Ainley & Mathieson [21] experimental results. In his book, Aungier [18] measured the angle from the tangential direction, as opposed to the convention used in this thesis, i.e. angles measured from meridional direction. Therefore, the expressions reported hereinafter are converted to the latter convention, unless otherwise specified.

Trailing Edge Losses
Trailing edge losses are computed as an expansion loss due to a sudden enlargement of the passage area [22]. The passage area after the blade trailing edge is approximately equal to $(s \sin \beta_g)$, therefore before the end of the blade it is the same quantity subtracted

of the trailing edge thickness. β_g is called the gauging angle, and it is defined from the throat o: $\sin \beta_g = \dfrac{o}{s}$.

The correlation for the loss coefficient is reported in Equation 2.25

$$\bar{\omega}_{TE} = \left(\frac{t_{TE}}{s \sin \beta_g - t_{TE}} \right)^2 \tag{2.25}$$

Profile Losses

The profile loss correlation is the Ainley & Mathieson one [21], modified by Aungier [18]. $\bar{\omega}_{prof}$ are calculated as a weighted average between the losses of a nozzle turbine (cascade with fully axial inlet) and the losses of an impulse turbine (inlet and outlet are symmetrical), corrected by several coefficients. The Aungier revision consists in the removal of the trailing edge loss, which is treated in a separate manner. In the original formulation it was already included, considering a trailing edge thickness of $t_{TE} = 0.02s$. The formulation is reported in Equation 2.26.

$$\bar{\omega}_{prof} = K_{mod}K_{inc}K_M K_P K_{RE} \left\{ \left[\bar{\omega}_{p1} + \xi^2(\bar{\omega}_{p2} - \bar{\omega}_{p1}) \right] \left(5\frac{t_{max}}{c} \right)^{\xi} - \bar{\omega}_{TE} \right\} \tag{2.26}$$

The parameter present in this formulation are:

- K_{mod}, correction for modern profiles, which are more efficient. It is equal to $\dfrac{2}{3}$.

- K_{inc}, correction for incidence angle.

- K_M, correction for Mach number effects.

- K_P, correction for compressibility effects.

- K_{RE}, correction for Reynolds number effects.

- Y_{p1}, profile loss coefficient for nozzle blades

- Y_{p2}, profile loss coefficient for impulse blades

- $\xi = \dfrac{\beta_{in}^g}{\beta_{out}}$, which is the weight for the average between the two profile losses. When $\beta_{in}^g = 0$, it is a nozzle turbine, therefore only Y_{p1} is considered. When $\beta_{in}^g = \beta_{out}$, it is an impulse turbine, therefore only Y_{p2} is considered.

Y_{p1}

Profile losses for nozzle turbines are provided in relation to the solidity and to the outlet angle. The equations for interpolating the graph data are taken from Aungier [18], and

are shown in Equation 2.27.

$$Y_{p1} = \begin{cases} A + BX^2 + CX^3, & \text{if } |\beta_{out}| \geq 60° \\ A + B|X|^n, & \text{if } |\beta_{out}| < 60° \end{cases} \tag{2.27}$$

The coefficients used for the equations are depicted in Equation 2.28.

$$X = \frac{1}{\sigma} - \frac{1}{\sigma_{min}}$$

$$\frac{1}{\sigma_{min}} = \begin{cases} 0.46 + \dfrac{90 - |\beta_{out}|}{77}, & \text{if } |\beta_{out}| \geq 60° \\ 0.614 + \dfrac{90 - |\beta_{out}|}{130}, & \text{if } |\beta_{out}| < 60° \end{cases}$$

$$n = 1 + \frac{90 - |\beta_{out}|}{30}$$

$$A = \begin{cases} 0.025 + \dfrac{|\beta_{out}| - 63}{530}, & \text{if } |\beta_{out}| \geq 63° \\ 0.025 + \dfrac{|\beta_{out}| - 63}{3085}, & \text{if } |\beta_{out}| < 63° \end{cases} \tag{2.28}$$

$$B = 0.1583 - \frac{90 - |\beta_{out}|}{1640}$$

$$C = 0.08 \left[\left(\frac{90 - |\beta_{out}|}{30} \right)^2 - 1 \right]$$

The graphical data from Ainley & Mathieson is shown in Figure 2.15.
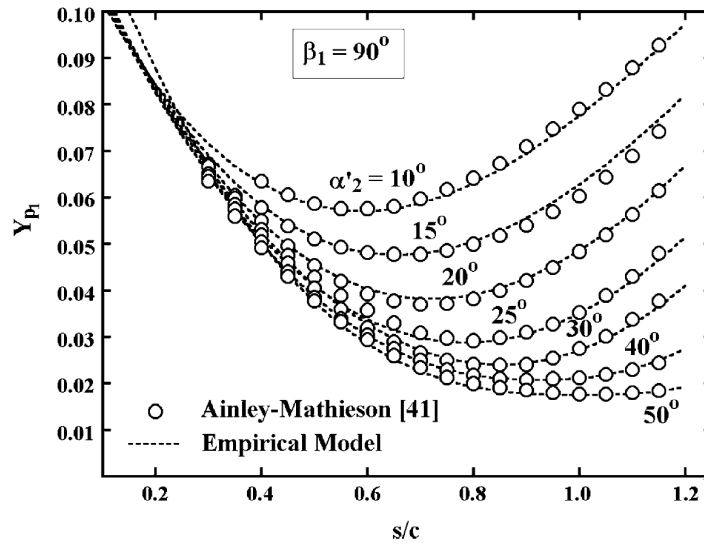
Figure 2.15: Pressure loss coefficient for nozzle blades. [21]. The data reported in this graph uses the tangential angle convention (β_{TG}) and not the axial one (β_{AX}). Therefore, the correct angles to be used in the correlations is $\beta_{AX} = 90 - \beta_{TG}$.

Y_{p2}

Profile losses for impulse turbines are also provided in relation to the solidity and the outlet angle. The equations are shown in Equation 2.27.

$$Y_{p2} = A + BX^2 - CX^3 \tag{2.29}$$

The coefficients used for the equations are depicted in Equation 2.30.

$$X = \frac{1}{\sigma} - \frac{1}{\sigma_{min}}$$

$$\frac{1}{\sigma_{min}} = 0.224 + 1.575 \frac{90 - |\beta_{out}|}{90} - \left(\frac{90 - |\beta_{out}|}{90}\right)^2$$

$$A = 0.242 - \frac{90 - |\beta_{out}|}{151} + \left(\frac{90 - |\beta_{out}|}{127}\right)^2 \tag{2.30}$$

$$B = \begin{cases} 0.3 - \dfrac{|\beta_{out}| + 60}{50}, & \text{if } |\beta_{out}| \geq 60° \\ 0.3 - \dfrac{|\beta_{out}| + 60}{275}, & \text{if } |\beta_{out}| < 60° \end{cases}$$

$$C = 0.88 - \frac{90 - |\beta_{out}|}{42.4} + \left(\frac{90 - |\beta_{out}|}{72.8}\right)^2$$

The graphical data from Ainley & Mathieson is shown in Figure 2.16.
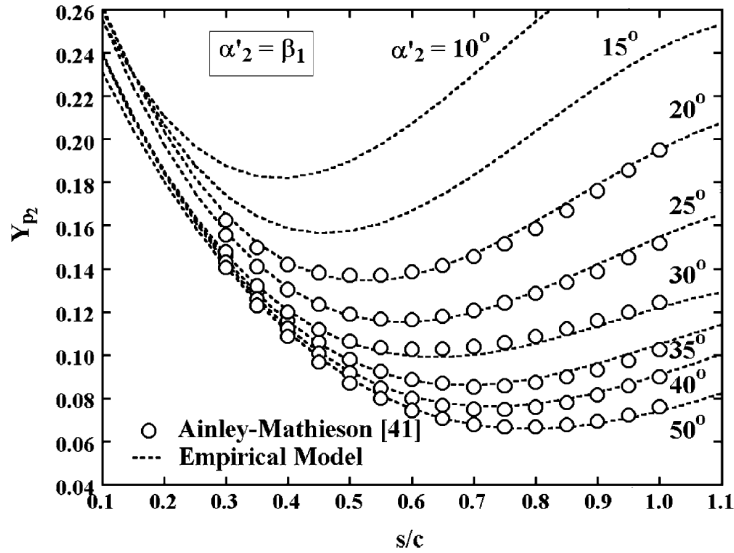
Figure 2.16: Pressure loss coefficient for impulse blades. [21]. The data reported in this graph uses the tangential angle convention (β_{TG}) and not the axial one (β_{AX}). Therefore, the correct angles to be used in the correlations is $\beta_{AX} = 90 - \beta_{TG}$.

The mathematical expressions of profile losses for compressor and turbine is not similar, but it reflects similar concepts:

- losses increase for increasing deflection

- losses increase for increasing $|\beta_{opt}|$

- there's an optimum σ that minimises $\bar{\omega}_{prof}$

The presence of an optimum σ is easily understandable by looking at Figure 2.15 and Figure 2.16. For compressor losses it is implicit in the fact that $\bar{\omega}_{prof}$ increases linearly with σ, but D_{eq}, which influences $\dfrac{\theta_w}{c}$, decreases with increasing σ.

K_{inc}

The correction for i is given as a function of the ratio between the incidence angle and the stalling incidence angle i_s. Loss increases for increasing i as absolute value, with greater influence for positive i.

The expressions for the incidence correction factor is given in Equation 2.31.

$$K_{inc} = \begin{cases} -1.39214 - 1.90738\dfrac{i}{i_s}, & \text{if } \dfrac{i}{i_s} < -3 \\[2mm] 1 + 0.52\left|\dfrac{i}{i_s}\right|^{1.7}, & \text{if } -3 \leq \dfrac{i}{i_s} < 0 \\[2mm] 1 + \left(\dfrac{i}{i_s}\right)^{2.3+0.5\frac{i}{i_s}}, & \text{if } 0 \leq \dfrac{i}{i_s} < 1.7 \\[2mm] 6.23 + 9.8577\left(\dfrac{i}{i_s} - 1.7\right), & \text{if } \dfrac{i}{i_s} >= 1.7 \end{cases} \tag{2.31}$$

i_s is computed from a reference value i_{sr}, obtained with $\sigma = 1.33$, as shown in Equation 2.32, and then corrected for different σ.

$$i_s = i_{sr} + \Delta i_s$$

$$i_{sr} = \begin{cases} i_{s0} + \left|\left.i_{sr}\right|_{|\beta_{out}|=50} - i_{s0}\right|\left|\dfrac{|\beta_{out}| - 35}{15}\right|, & \text{if } |\beta_{out}| \geq 50° \\[2mm] i_{s0} + A - B\xi^2 + C\xi^3 + D\xi^4, & \text{if } |\beta_{out}| < 50° \end{cases}$$

$$i_{s0} = 20 - \dfrac{\xi + 1}{0.11}$$

$$A = 61.8 - \left(1.6 - \dfrac{90 - |\beta_{out}|}{165}\right)|\beta_{out}|$$

$$B = 71.9 - 1.69(90 - |\beta_{out}|)$$

$$\tag{2.32}$$

$$C = 7.8 - \left(0.28 - \frac{90 - |\beta_{out}|}{320} \right) |\beta_{out}|$$

$$D = 14.2 - \left(0.16 + \frac{90 - |\beta_{out}|}{160} \right) |\beta_{out}|$$

$$X = \frac{1}{\sigma} - 0.75$$

$$\Delta i_s = \begin{cases} -38X - 53.5X^2 - 29X^3, & \text{if } \sigma \geq 1.25 \\ 2.0374 - \left(\frac{1}{\sigma} - 0.8 \right) \left[69.58 - \left(\frac{90 - |\beta_{out}|}{14.48} \right)^{3.1} \right], & \text{if } \sigma < 1.25 \end{cases}$$

The graphical data from Ainley & Mathieson is shown in Figure 2.17.
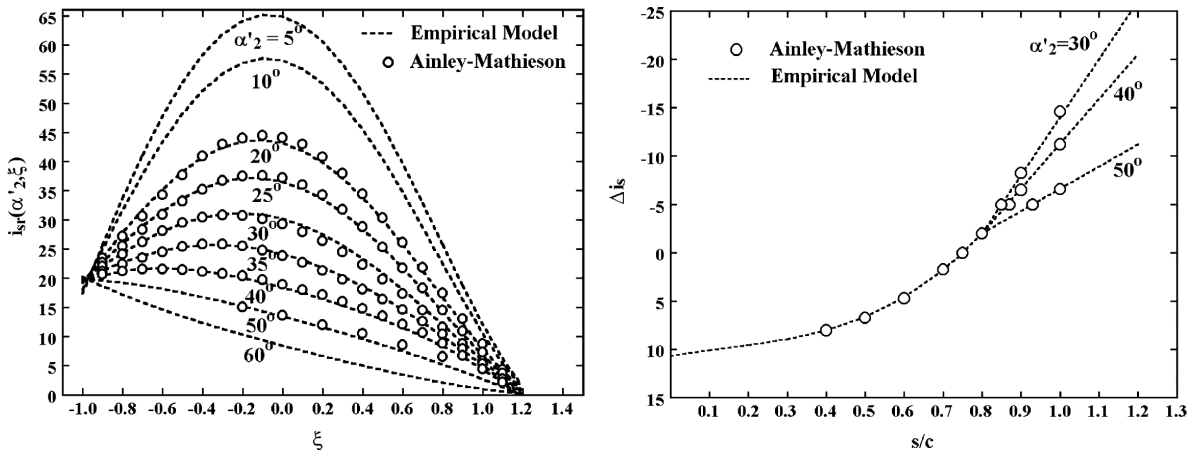
(a) Stalling incidence for $\sigma = 1.33$.   (b) Stalling incidence correction factor.
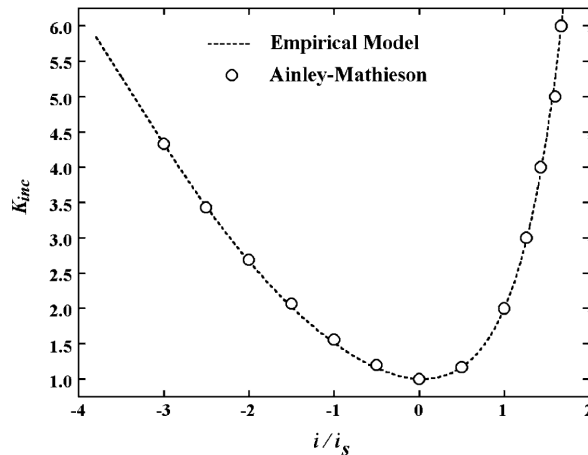
(c) Correction factor for off-design incidence.

Figure 2.17: Correction coefficients for compressor optimal incidence angle. The data reported in this graph uses the tangential angle convention (β_{TG}) and not the axial one (β_{AX}). Therefore, the correct angles to be used in the correlations is $\beta_{AX} = 90 - \beta_{TG}$.

K_M

Mach number correction factor accounts for local shock waves that are present starting from Mach number greater than 0.6. In case of supersonic Mach number, losses have to be considered with an appropriate shock loss correlation, which is not used in this work for low loading nature of this application. Mach number effects are enhanced by a lower radius of curvature of the suction side of the blade R_{SS}.

The numerical expressions reported by Aungier [18], was revealed to be wrong, since it did not match the experimental results reported by Ainley & Mathieson [21]. The formula here reported is extrapolated directly from the graph, using an Excel solver.
The obtained expression is reported in Equation 2.33.

$$K_M = 1 + \left[1.17(M_{out} - 0.52) + 192.58(M_{out} - 0.68)^3\right] \left(\frac{s}{R_{SS}}\right)^{3.01M_{out}-0.55} \tag{2.33}$$

The graphical data from Ainley & Mathieson is shown in Figure 2.18.
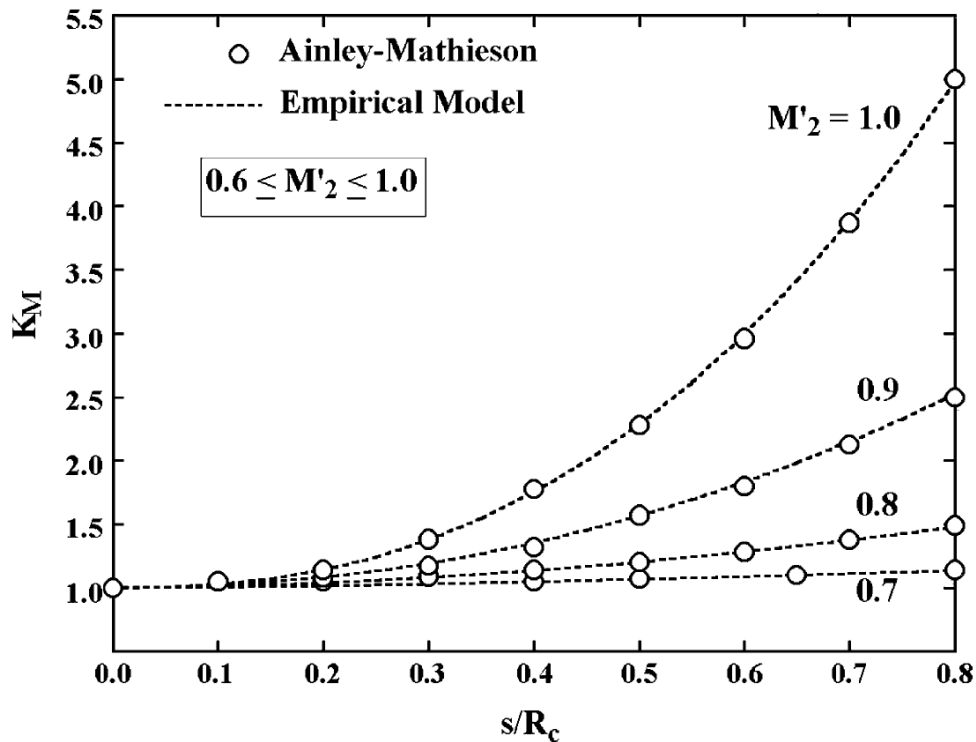
Figure 2.18: Correction coefficient for Mach Number

K_p

In accelerating flows, compressibility reduces the boundary layer thickness and suppresses

flow separation, therefore providing a beneficial effect. In this case the Kacker & Okapuu [19] model has been revised by Aungier [18] to avoid particular operating conditions in which the profile loss coefficient becomes negative.

The expression for K_p is reported in Equation 2.34.

$$K_p = 1 - (1 - K_1)X^2 \tag{2.34}$$

The coefficients present are delineated in Equation 2.35.

$$
\begin{aligned}
K_1 &= 1 - 0.625 \left(\tilde{M}'_{out} - 0.2|\tilde{M}'_{out} - 0.2| \right) \\
X &= \frac{2\tilde{M}'_{in}}{\tilde{M}'_{in} + \tilde{M}'_{out} + |\tilde{M}'_{out} - \tilde{M}'_{in}|} \\
\tilde{M}'_{in} &= \frac{M'_{in} + 0.566 - |0.566 - M'_{in}|}{2} \\
\tilde{M}'_{out} &= \frac{M'_{out} + 1 - |M'_{out} - 1|}{2}
\end{aligned}
\tag{2.35}
$$

K_{RE}

Reynolds correction factor accounts for roughness effect on performance, using the skin friction model of flat planes. For $Re_c < 1 \cdot 10^5$ it is based on the laminar skin friction model, while consequently for $Re_c > 5 \cdot 10^5$ it is based on the turbulent skin friction model. For $5 \cdot 10^5 < Re_c < 5 \cdot 10^5$, K_{RE} is 1. The expressions are reported in Equation 2.36.

$$
K_{RE} =
\begin{cases}
\sqrt{\dfrac{10^5}{Re_c}}, & \text{if } Re_c < 10^5 \\
1, & \text{if } 10^5 < Re_c < 5 \cdot 10^5 \\
1 + \left[\left(\dfrac{\log(5 \cdot 10^5)}{\log(Re_r)} \right)^{2.58} - 1 \right] \left(1 - \dfrac{5 \cdot 10^5}{Re_c} \right), & \text{if } Re_c > 5 \cdot 10^5
\end{cases}
\tag{2.36}
$$

The influence on the blade peak-to-valley roughness e is present only for turbulent regime, and it is expressed in terms of of a critical blade chord number $Re_r = 100\dfrac{c}{e}$, above which roughness effect is relevant.

The graphical data from Ainley & Mathieson is shown in Figure 2.19.
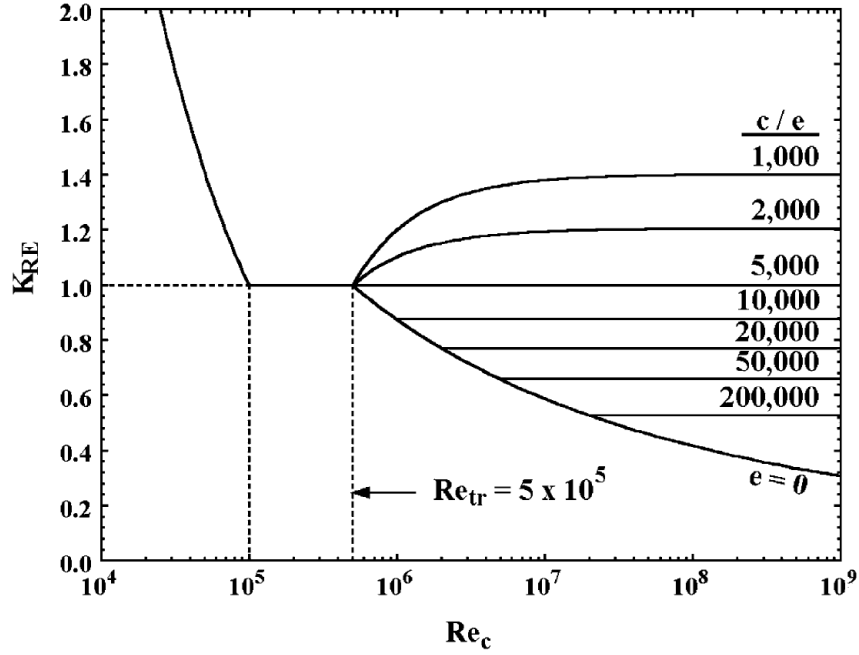
Figure 2.19: Correction coefficient for Reynolds Number

Secondary Flow and End-Wall Losses

In Ainley & Mathieson [21] secondary flow losses and end-wall losses are treated together, as the effects from non-uniformity of the flow through a cascade, in particular due to the presence of boundary layer on the casing.

The expression for the secondary flow loss coefficient is shown in Equation 2.37.

$$\bar{\omega}_{sec} = K_{RE}K_s\sqrt{\frac{Y_s^2}{1 + 7.5Y_s^2}} \tag{2.37}$$

The expression is based on the same lift coefficient as seen for compressors in Equation 2.15. This lift coefficient is used to calculate a preliminary secondary flow loss coefficient Y_s, corrected for low aspect ratio blades, as suggested from Kacker & Okapuu [19].

The expressions for the coefficients needed to calculate $\bar{\omega}_{sec}$ are depicted in Equation 2.38.

$$Z = (C_L\sigma)^2 \frac{\cos^2\beta_{out}}{\cos^3\bar{\beta}}$$

$$Y_s = 0.0334 F_{AR}\, Z \frac{\cos\beta_{out}}{\cos\beta_{in}} \tag{2.38}$$

$$F_{AR} = \begin{cases} \dfrac{c}{b}, & \text{if } \dfrac{b}{c} \geq 2 \\ 0.5\left(2\,\dfrac{c}{b}\right)^{0.7}, & \text{if } \dfrac{b}{c} < 2 \end{cases}$$

$$K_s = 1 - (1 - K_p)\dfrac{\left(\frac{c_{ax}}{b}\right)^2}{1 + \left(\frac{c_{ax}}{b}\right)^2}$$

The expression for the end-wall losses for the compressor is identical to the Ainley loading parameter Z for turbine, except for the use of the C_L instead of C_{Dew}. Nevertheless, C_{Dew} is inversely proportional to AR and σ, as are, respectively, F_{AR} and C_L.

Tip Clearance Losses

Tip clearance, as for compressors, is necessary to allow for a smooth operation of the machine and avoid rubbing. The flow in the gap is subject to two pressure gradients: one from PS to SS of the blade and from inlet to outlet of the cascade. This causes vortexes, as well as letting through a part of the flow that is not expanded by the blade, diminishing the work that can be extracted.

The loss coefficient is taken from Dunham & Came [20], as shown in Equation 2.39.

$$\bar{\omega}_{CL} = 0.47 Z \left(\frac{c}{b}\right) \left(\frac{\tau}{c}\right)^{0.78} \tag{2.39}$$

This expression can be well correlated with the one of compressors, since they both are depend on the square of the lift coefficient of the blade (here present in the coefficient Z), which models the pressure gradient between PS and SS. Moreover, the dependence on blade geometrical features is identical: they are both inversely proportional to the aspect ratio of the blade and they both increase with σ. The proportionality with the gap, however, is not linear and is not the same: for compressors it is greater than 1, while for turbine it is lower than 1.

2.3.2.2.   Flow Angles for Turbines

In case of turbines, the optimal incidence angle is equal to 0, while deviation still exists, for the same reasons as the compressor. Nevertheless, deviation angle is less critical for turbines due to the reduced pressure gradient present and due to the fact that deflections are generally much higher, therefore its weight is reduced.

Deviation angle

Deviation correlation is taken from Aungier [18], and it is a function of only geometrical parameters. For $M/M_w < 0.5$ it is constant, with a value depending on the gauging angle

β_g. At $M/M_w = 1$ it is equal to 0, and for $0.5 < M/M_w < 1$ it is created a fitting curve for linking the two values.

The numerical expressions for the deviation are reported in Equation 2.40

$$\delta = \begin{cases} \arcsin\left(\left(\dfrac{o}{s}\right)\left[1 + \left(1 - \dfrac{o}{s}\right)\left(\dfrac{\beta_g}{90}\right)^2\right]\right) - \beta_g, & \text{if } M_{out} \leq 0.5 \\ \delta\Big|_{M_{out}=0.5}(1 - 10X^3 + 15X^4 - 6X^5), & \text{if } 0.5 < M_{out} < 1 \end{cases} \qquad (2.40)$$

$$X = 2M_{out} - 1$$

A summary of all the loss and flow angles correlation for both compressor mode and turbine mode is shown in Table 2.1.

Table 2.1: Summary of all loss and angles correlation used in this work.

Correlation	Compressor mode	Turbine mode
Profile Losses	$\bar{\omega}_{prof} = 2\dfrac{\theta_w}{c}\dfrac{\sigma}{\cos\beta_{out}}\left(\dfrac{W_{out}}{W_{in}}\right)^2$	$\bar{\omega}_{prof} = K_{mod}K_{inc}K_MK_PK_{RE}\left\{\left[\bar{\omega}_{p1} + \xi^2(\bar{\omega}_{p2} - \bar{\omega}_{p1})\right]\left(5\dfrac{t_{max}}{c}\right)^\xi - \bar{\omega}_{TE}\right\}$
Secondary Flow Losses	$\bar{\omega}_{sec} = \dfrac{1}{2}\dfrac{C_{Ds}\,\rho_{in}\,\sigma\bar{W}^2}{P_{Tin} - P_{in}}$	$\bar{\omega}_{sec} = K_{RE}K_s\sqrt{\dfrac{Y_s^2}{1 + 7.5Y_s^2}}$
End-wall Losses	$\bar{\omega}_{ew} = C_{Dew}\sigma\dfrac{\cos^2\beta_{in}}{\cos^3\bar{\beta}}$	/
Tip clearance Losses	$\bar{\omega}_{tip} = (C_{D1} + C_{D2})\dfrac{\frac{1}{2}\sigma\rho_{in}\bar{W}^2}{P_{Tin} - P_{in}}$	$\bar{\omega}_{CL} = 0.47Z\left(\dfrac{c}{b}\right)\left(\dfrac{\tau}{c}\right)^{0.78}$
Trailing Edge Losses	/	$\bar{\omega}_{TE} = \left(\dfrac{t_{TE}}{s\sin\beta_g - t_{TE}}\right)^2$
Deviation Angle	$\delta = K_{sh}K_{t,\delta}(\delta_0)_{10} + m\theta$	$\delta = \begin{cases} \arcsin\left(\left(\dfrac{o}{s}\right)\left[1 + \left(1 - \dfrac{o}{s}\right)\left(\dfrac{\beta_g}{90}\right)^2\right]\right) - \beta_g, & \text{if } M_{out} \le 0.5 \\[2ex] \delta\big|_{M_{out}=0.5}(1 - 10X^3 + 15X^4 - 6X^5), & \text{if } 0.5 < M_{out} < 1 \end{cases}$
Optimal incidence Angle	$i = K_{sh}K_{t,i}(i_0)_{10} + n\theta$	$i = 0$

2.4. Meanline Code Validation

The code calculations now have to be verified through CFD simulations. To validate the three archetypal stages (first, intermediate, and last) only three stages are simulated. In this way the repetition of the middle, repeated ones which would only increase the computational time is avoided.

Since using Lieblein's correlations for losses and deviation, the characteristics of the machine have to match its experiments in terms of fluidynamic conditions. Therefore, it is looked for a machine with contained loading ($\lambda < 0.4$ and $\phi < 0.65$) and with the same chord Reynolds number range (between $2.0 \cdot 10^5$ and $4.5 \cdot 10^5$).

The values chosen are shown in Table 2.2.

Table 2.2: Input values for the preliminary performance prediction.

Stage	1		2		1	
Cascade	R	S	R	S	R	S
ϕ	0.55		0.62		0.62	
λ	0.4		/		0.22	
χ	0.85		0.5		0.68	
σ	1.2	1	1.25	1	1.2	
Re_c	$4.5 \cdot 10^5$	$4.5 \cdot 10^5$	$4.5 \cdot 10^5$	$4.5 \cdot 10^5$	$4.5 \cdot 10^5$	

P_{Tin} is chosen as 2 bar, T_{Tin} as 300K and P_{Tout} as 2.65. In this way β_{TT} is of 1.325, meaning an average β for every stage of 1.098. λ for the middle stages resulted 0.333. Working fluid is air, considered as ideal gas. The mean diameter D_m is chosen as 1080 mm. A higher D_m lowers the loading coefficient, since it lowers the deflection needed, but lower deflection can cause the blade thickness to be reduced, as explained in section 2.2. For structural reasons, it is decided for any blade to have a thickness-to-chord ratio of at least 0.05, therefore D_m cannot be as high as wanted. This trade-off delivered a peripheral velocity at midspan of 169 $\frac{m}{s}$.

Since the inlet velocity is derived from the ϕ_1, and the density is derived from thermodynamic quantities, the mass flow rate influences only the passage area, therefore the blade height b. It is chosen as 25 $\frac{kg}{s}$, in order to obtain the aspect ratio of the first blade of about 2.

Tip clearance is set as 0.5mm and is present only in the rotors, while stators can allow for a better sealing, thus neglecting the presence of the clearance.

The machine described here is the one considered for all the meanline validation procedure.

The first step is to simulate the behaviour of the machine at midspan, performing quasi-3D simulations which accounts only for profile losses. Then, more comprehensive 3D simulations are executed, in order to capture three-dimensional effects, such as secondary flows and tip clearance losses.

2.4.1. Compressor Code Validation

The software used for creating the mesh is TurboGrid, which belongs to the ANSYS package. It requires as input the hub, shroud and blade coordinates provided by the meanline code, as well as mesh characteristics, such as number of elements and boundary layer characteristics. The software splits the domain in different blocks, each with a hex-structured mesh.

When simulating a single blade profile, the hub and shroud exceed the blade of half a chord from the leading edge and a full chord from the trailing edge, to guarantee uniform properties at the outlet face, hence avoiding spurious pressure oscillation therein. When instead simulating a cascade, it is chosen a spacing between two cascade of half of the axial chord.

After generating the computational domain, the simulation is set and performed with CFX. The simulations performed are steady-state, using the k-ω SST turbulence model, reaching y^{+} at the walls of 1, hence solving the boundary layer up to the blade. TurboGrid is able to build the mesh according to this constraint by providing as input Re_c.
The principal discretization schemes used are:

- second order central difference scheme for diffusion

- TVD with Barth & Jeperson flux limiter for convection

Total variation diminishing (TVD) exploits second order discretisation except in presence of high gradients, where a first-order one is used for ensuring stability.

All the simulations are performed until the isoentropic efficiency reaches a plateau and does not change with increasing number of iterations. No stopping criteria based on residuals or maximum number of iterations is therefore imposed.

2D simulations as mentioned earlier cannot be performed because Turbogrid necessitates of at least two elements in the radial direction. Therefore, quasi-3D CFD simulations are implemented. The domain simulated is only a slice of the blade, of constant height 0.002m, as described in section 2.2. It is needed to make the profile as bi-dimensional as

possible: D_m is increased, in order to have the same spacing using 300 blades, which is the maximum number allowable from Turbogrid. In this way, being at a bigger diameter, the curvature in the secondary plane is lower, decreasing the three-dimensional effects. The mass flow rate needs to be scaled as well, in order to have the same velocity inlet.

An example of the mesh for a single blade is shown in Figure 2.20, illustrating it in the blade-to-blade plane and in the secondary plane.
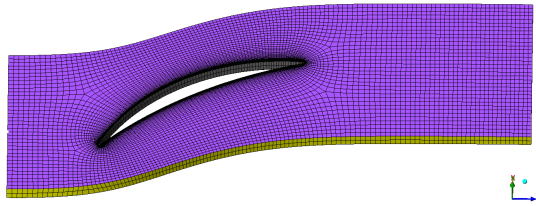
Figure 2.20: Mesh example for a single compressor rotor blade.

The 2 layers in radial direction are visible, as well as the discretization in the blade-to-blade plane, with the meridional length of the domain to allow the flow to uniform before the outlet face.

At first, a grid independency analysis has to be performed, therefore it is taken a single blade, the second rotor of the compressor mode of the machine described earlier, and simulated with increasing number of mesh elements, until convergence on a certain parameter is observed. The parameter chosen is the compressor total pressure loss coefficient, as defined in Equation 2.11, consistently with the aim of validating the profile loss correlation provided by Lieblein. Being the simulation bi-dimensional, the only losses present are the profile ones.
The first and last stage are particular due to the high reaction degree, therefore it is chosen to simulate the second rotor because it represent a classic repeated stage with reaction degree equal to 0.5.

The boundary conditions applied are:

- $P_T = 227\,040$ Pa and $T_T = 311.48$ K at the inlet face

- $\alpha = 28.46°$ at the inlet face

- $\dot{m} = 2.832 \; \dfrac{kg}{s}$ at the outlet face

- Periodicity at side faces

- Free-slip at hub and shroud

The free-slip condition forces the streamlines to follow the hub and the shroud, which is necessary for this kind of simulations. This approximation introduces a certain degree of inaccuracy since the shape of the streamtube in reality is not necessarily the one chosen of constant height.

For every CFD simulation performed in this work, adiabatic and smooth walls are considered.

Simulations are performed starting from 20 000 elements and going up to 100 000, and finally 300 000 elements. Due to the presence of two elements in the radial direction, the elements in the blade-to-blade plane are half of the ones indicated.

The results or the grid independence analysis is shown in Table 2.3.

Table 2.3: Grid independency analysis for 2D simulations.

Mesh elements number	$\bar{\omega}_{prof}$
20 000	0.0234
100 000	0.0198
300 000	0.0197

When passing from 20 000 elements to 100 000, the profile loss diminish of 15%, while it changes of only 0.5% when increasing the number of elements to 300 000. Therefore, the mesh with 100 000 elements is considered as the independent one and can be used to compare the meanline code results. The comparison is made for what concerns kinematic and thermodynamic parameters, calculating how much distant the meanline calculations are from the CFD results as percentage. Calculations are considered accurate if the difference is in the range of ±5%.

The result of the comparison for the main quantities is shown in Table 2.4.

Table 2.4: Quasi-3D CFD with constant blade height comparison with the meanline code.

Quantity	Quasi-3D CFD		Meanline		Error	
	In	Out	In	Out	In	Out
$P_T \left[\dfrac{N}{m^2}\right]$	227 040	251 200	227 040	248 740	0.00 %	0.98 %
$T_T \ [K]$	311.48	321.58	311.48	319.87	0.00 %	0.53 %
$V_m \left[\dfrac{m}{s}\right]$	105.01	93.33	105.18	105.18	0.16 %	11.27%
$W_t \left[\dfrac{m}{s}\right]$	-111.63	-54.47	-109.64	-60.00	0.33 %	9.22 %
$\beta \ [°]$	-46.12	-32.86	-46.19	-29.70	0.33 %	10.64%

As can be seen, the kinematic quantities are far from the predicted ones of the meanline code, showing an error of about 10%. This might be caused by the δ correlation, which is not able to predict well the actual one, but also from the blade domain, which forces the stream tube to have the same height both at inlet and outlet. Considering the latter problematic, a simulation is performed with a new domain, which implements blade flaring. In this domain the blade height at outlet is kept the same, but the inlet one is increased to obtain the same ratio $\left(\dfrac{b_{out}}{b_{in}}\right)$ of the actual blade.

Since the domain span is changed only in the radial direction, where the number of elements has to be kept as 2, no variation in the mesh parameters is implemented. The results of the simulation are shown in Table 2.5.

Table 2.5: Quasi-3D CFD simulation with flaring comparison with meanline code.

Quantity	Quasi-3D flaring CFD		Meanline		Error	
	In	Out	In	Out	In	Out
$P_T \left[\dfrac{N}{m^2}\right]$	227 040	250 700	227 040	248 740	0.00 %	0.79 %
$T_T \ [K]$	311.48	321.00	311.48	319.87	0.00 %	0.35 %
$V_m \left[\dfrac{m}{s}\right]$	105.10	105.10	105.18	105.18	0.08 %	0.00 %
$W_t \left[\dfrac{m}{s}\right]$	-111.90	-58.96	-109.64	-60.00	2.06 %	1.74 %
$\beta \ [°]$	-46.79	-29.29	-46.19	-29.70	1.31 %	1.39 %

The implementation of the flaring improved the results, bringing every quantity to be in the given range of $\pm 5\%$.

Once a row of blade is simulated and the meanline predictions resulted accurate, the full compressor can be simulated, using firstly the same quasi-3D approach, and then a fully 3D approach, in order to verify also the accuracy of the other source of losses. Since the blade chord is more or less constant throughout the machine, the mesh size can be kept as the same of the single blade just simulated.

When simulating multiple cascades with relative motion, different approaches can be used, such multiple reference frame (MRF) and sliding meshes. While MRF necessitate for the flow to be nearly uniform at the interface, and sliding meshes calculation are necessarily unsteady, a convenient alternative that can reduce the computational time is the mixing-plane approach. With this method, the information between a domain and the other are passed as boundary conditions which are "mixed" at the interface. In this way, any unsteadiness that may arise due to the non-uniform circumferential flow, such as separated flow or wake, is removed, providing a steady-state result. Different mixing approaches can be used in CFX, the one chosen is the Constant Total Pressure, in which both the static and total pressure are averaged, in order to calculate the velocity field to be passed to the other blade.

The quasi-3D mesh resulted in $600\,000$ cells.

The boundary conditions used are the ones described for the full machine, which are:

- $P_T = 200\,000$ Pa and $T_T = 300$ K at the inlet face

- $\dot{m} = 2.743\ \dfrac{kg}{s}$ at the outlet face

- Periodicity at side faces

- Free-slip at hub and shroud

The results of the CFD simulation are shown in Table 2.6, the meanline predictions in Table 2.7 and the percentage error between the two calculations in Table 2.8.

Table 2.6: Quasi-3D CFD simulation results of the full machine for compressor mode.

Parameter	Rotor 1		Stator 1		Rotor 2		Stator 2		Rotor 3		Stator 3	
	In	Out	In	Out	In	Out	In	Out	In	Out	In	Out
$P_T \left[\frac{N}{m^2}\right]$	200 000	228 000	227 800		250 700		249 600		267 000		266 200	
$T_T \ [K]$	300.00	312.00	312.00		321.00		321.00		327.50		327.50	
$V \left[\frac{m}{s}\right]$	93.40	112.50	120.00		152.70		113.20		132.20		105.70	
$V_m \left[\frac{m}{s}\right]$	93.40	87.17	105.10		105.10		105.50		105.60		105.70	
$V_t \left[\frac{m}{s}\right]$	0.00	71.19	57.79		110.80		40.95		79.27		4.31	
$\alpha \ [°]$	0.00	39.24	28.80		46.51		21.21		36.89		2.34	
$W \left[\frac{m}{s}\right]$	193.70	132.20	153.50		120.70		166.40		139.00		/	
$W_t \left[\frac{m}{s}\right]$	-169.60	-98.83	-111.90		-58.96		-128.70		-90.37		/	
$\beta \ [°]$	-61.16	-48.59	-46.79		-29.29		-50.66		-40.56		/	
$M \ [-]$	0.27	0.32	0.34		0.43		0.32		0.37		0.29	
$M_w \ [-]$	0.56	0.38	0.44		0.34		0.47		0.39		/	
$\bar{\omega} \ [-]$	0.023		0.013		0.020		0.023		0.018		0.032	

Table 2.7: Meanline code results for the full machine for compressor mode.

Parameter	Rotor 1		Stator 1		Rotor 2		Stator 2		Rotor 3		Stator 3	
	In	Out	In	Out	In	Out	In	Out	In	Out	In	Out
$P_T \left[\frac{N}{m^2}\right]$	200 000	227 200	227 040		248 740		248 260		265 350		265 000	
$T_T \ [K]$	300.00	311.48	311.48		319.87		319.86		326.17		326.17	
$V \left[\frac{m}{s}\right]$	93.31	110.27	121.09		151.94		111.05		128.00		105.18	
$V_m \left[\frac{m}{s}\right]$	93.31	86.92	105.18		105.18		105.18		105.18		105.18	
$V_t \left[\frac{m}{s}\right]$	0.00	67.86	60.00		109.64		35.63		72.95		0.00	
$\alpha \ [°]$	0.00	37.98	29.70		46.19		18.71		34.74		0.00	
$W \left[\frac{m}{s}\right]$	193.61	133.85	151.94		121.09		170.37		142.88		/	
$W_t \left[\frac{m}{s}\right]$	-169.65	-101.79	-109.64		-60.00		-134.02		-96.70		/	
$\beta \ [°]$	-61.19	-49.51	-46.19		-29.70		-51.88		-42.59		/	
$M \ [-]$	0.27	0.31	0.35		0.43		0.31		0.36		0.29	
$M_w \ [-]$	0.56	0.38	0.43		0.34		0.48		0.40		/	
$\bar{\omega} \ [-]$	0.019		0.010		0.014		0.016		0.012		0.015	

Table 2.8: Percentage error of the quasi-3D simulation of the full machine compared to the meanline code for compressor mode.

Parameter	Rotor 1		Stator 1		Rotor 2		Stator 2		Rotor 3		Stator 3	
	In	Out	In	Out	In	Out	In	Out	In	Out	In	Out
P_T $\left[\frac{N}{m^2}\right]$	0.00 %	0.35 %	0.33 %		0.79 %		0.54 %		0.62 %		0.45 %	
T_T $[K]$	0.00 %	0.17 %	0.17 %		0.35 %		0.36 %		0.41 %		0.41 %	
V $\left[\frac{m}{s}\right]$	0.10 %	2.02 %	0.90 %		0.50 %		1.94 %		3.28 %		0.49 %	
V_m $\left[\frac{m}{s}\right]$	0.10 %	0.29 %	0.08 %		0.08 %		0.30 %		0.40 %		0.49 %	
V_t $\left[\frac{m}{s}\right]$	0.00 %	4.91 %	3.69 %		1.06 %		14.94 %		8.67 %		/	
α $[°]$	0.00%	3.31 %	3.03 %		0.70 %		13.37 %		6.19 %		/	
W $\left[\frac{m}{s}\right]$	0.05 %	1.23 %	1.03 %		0.32 %		2.33 %		2.72 %		/	
W_t $\left[\frac{m}{s}\right]$	0.03 %	2.91 %	2.06 %		1.74 %		3.97 %		6.54 %		/	
β $[°]$	0.05 %	1.86 %	1.31 %		1.39 %		2.35 %		4.78 %		/	
M $[-]$	0.14 %	2.37 %	0.94 %		0.46 %		1.87 %		3.18 %		0.41 %	
M_w $[-]$	0.06 %	1.18 %	0.97 %		0.46 %		2.42 %		2.78 %		/	
$\bar{\omega}$ $[-]$	20.5%		28.2%		45.2%		44.1%		51.9%		104.7%	

The kinematic and thermodynamic quantities are all within the 5% limit up the outlet of the second stator, The reason might be in the fact that δ is overestimated, therefore the flow has a incidence angle i which is different from the design one. This causes an increment in the loading on the blade, therefore of δ. This increment in the loading is not accounted in the meanline code, since the correlation used and reported in Table 2.1 works only for design i. This means that the i accumulates cascade over cascade, increasing the gap between the meanline predictions and the CFD simulations due to its influence on δ and losses.

This is also a cause of the increase in the total pressure loss coefficient error, which again is not accounted for in the meanline code. Another factor influencing the total pressure loss coefficient error might be the mixing-plane approach when passing informations from a cascade to the next one. P_T evaluated at one side of the interface or the other might vary of few hundreds of Pa, which is negligible compared to the value of P_T itself, but when using it to calculate the loss coefficient, it might bring to a variation of the results of even the 30 %.

This increase deviation angle can be seen in Figure 2.21, in which the streamlines of the flow in the second stage are highlighted.
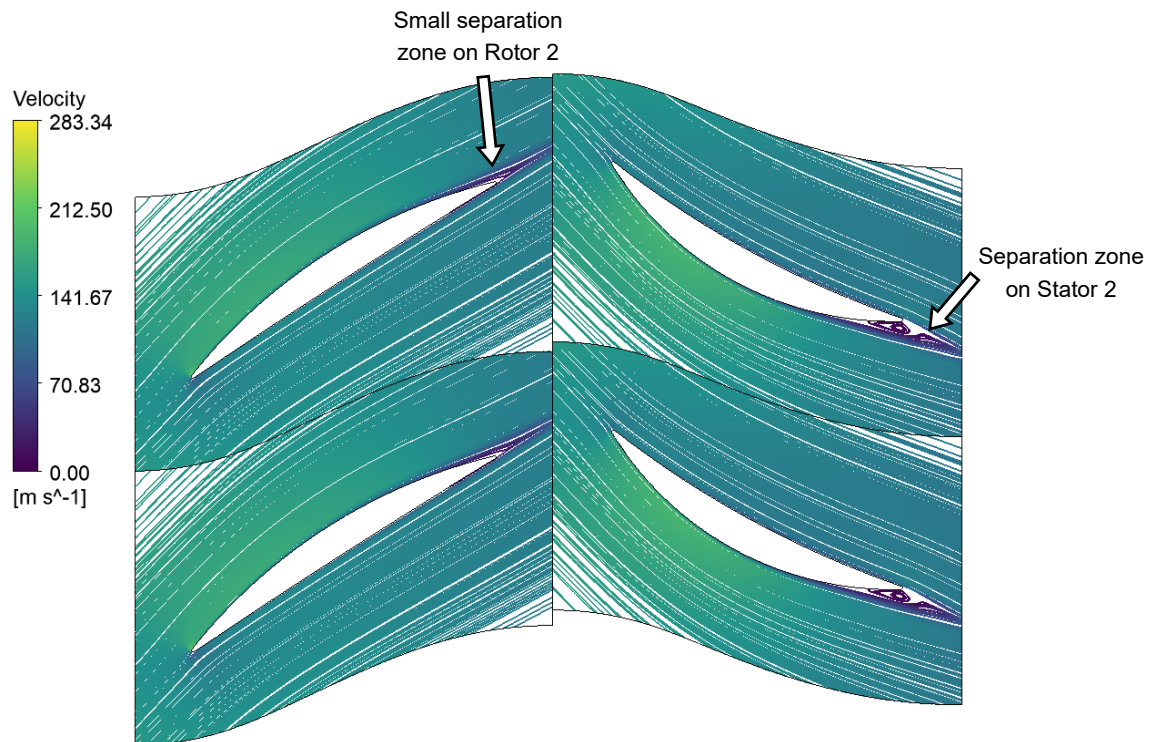
Figure 2.21: Streamlines on the second stage for the quasi-3D simulation.

It can be seen how from the second stator there is a separation zone at the trailing edge, which causes the flow to enter the successive cascade with a wrong i.

The final step is to simulate the fully 3D machine. The mesh in no more composed by only 2 elements in the radial direction, but it has to be able to capture the effects of the walls and in the clearance gap. The radial span of the blade is split in four parts, the hub, the shroud, the tip gap and the passage for the free stream. An example of the mesh, with its parts in shown in Figure 2.22. (The tip gap has been increased just for visualization purposes). In case of stators the part of the mesh corresponding to the tip clearance is not present, therefore the shroud part reaches the casing.
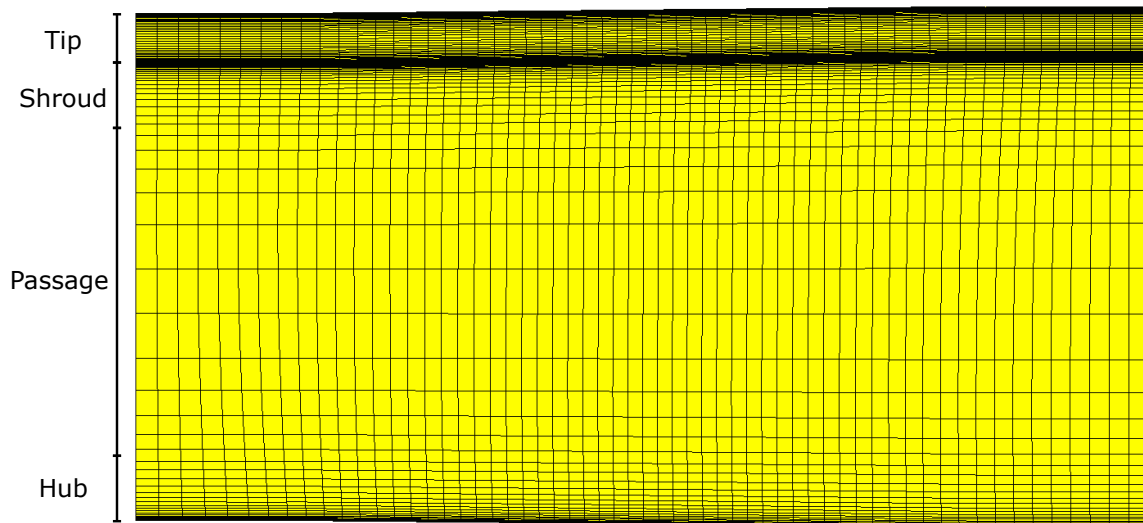
Figure 2.22: Mesh subdivision for the passage discretisation.

The mesh part at the hub has a span of 10 % of the blade height, and it represents the boundary layer at the casing. The parameters needed to create this part of the mesh are the y^+ looked for at the wall (1, as mentioned earlier) and the expansion ratio of the cells, which is the ratio between the height of two consecutive cells. This parameter is modified in order to obtain a number of elements representing the boundary layer of 13. The mesh at the tip of the blade is created in the same manner, while the clearance gap one matches the expansion ratio at the tip. Finally, for the free stream mesh it is given the number of mesh elements in which it is discretised. The mesh discretisation is kept the same for the blade-to-blade plane, while it is necessary to perform an independence analysis for the radial span discretisation. The number of elements in which the blade is discretised in the radial direction is increased from 12 to 20 and finally to 30.

Again, it is looked for the total pressure loss coefficient to not change when increasing the number of cells. This convergence is done on the first blade of the machine since the flow entering the cascade has an uniform direction, which is not true for the second rotor. Moreover, it is the highest blade, therefore the one that requires more elements to be discretised in. The same discretisation is kept for all the other blades.

The results for the grid independence analysis is shown in Table 2.9.

Table 2.9: Grid independence analysis for the 3D blade

Passage elements number	$\bar{\omega}$
12	0.0353
20	0.0335
30	0.0334

The total pressure loss coefficient changes of 0.30% when increasing the number of passage layers from 20 to 30, therefore the 20 layer mesh is chosen as the right one to simulate with, which resulted in about 2 000 000 cells per blade row.

The boundary conditions used are the same as the quasi-3D simulation, with the exception of the hub and the shroud: for the hub is used a no-slip condition, while for the shroud is used a counter-rotating wall in case of rotors and no-slip for stators.

Results for the fully 3D simulations are shown in Table 2.10.

Table 2.10: 3D CFD simulation results for compressor mode.

Parameter	Rotor 1		Stator 1		Rotor 2		Stator 2		Rotor 3		Stator 3	
	In	Out	In	Out	In	Out	In	Out	In	Out	In	Out
$P_T \left[\frac{N}{m^2}\right]$	200 003	226 914	226 276		250 928		249 223		263 784		262 055	
$T_T \left[K\right]$	300.00	311.65	311.72		321.44		321.53		327.07		327.09	
$V \left[\frac{m}{s}\right]$	93.48	113.24	119.24		154.91		116.38		133.60		110.91	
$V_m \left[\frac{m}{s}\right]$	93.48	89.52	105.84		106.63		107.57		108.61		110.63	
$V_t \left[\frac{m}{s}\right]$	0.00	68.29	54.57		111.87		43.99		76.74		4.86	
$\alpha \left[°\right]$	0.00	37.34	27.28		46.37		22.24		35.24		2.52	
$W \left[\frac{m}{s}\right]$	194.47	136.34	157.06		121.94		166.19		143.64		/	
$W_t \left[\frac{m}{s}\right]$	-170.49	-102.34	-115.89		-58.48		-126.45		-93.74		/	
$\beta \left[°\right]$	-61.26	-48.82	-47.60		-28.74		-49.61		-40.80		/	
$M \left[-\right]$	0.27	0.32	0.34		0.44		0.33		0.37		0.31	
$M_w \left[-\right]$	0.56	0.39	0.45		0.35		0.47		0.40		/	
$\bar{\omega} \left[-\right]$	0.034		0.020		0.029		0.034		0.020		0.066	

Table 2.11: Meanline code results for the 3D CFD simulation for compressor mode.

Parameter	Rotor 1		Stator 1		Rotor 2		Stator 2		Rotor 3		Stator 3	
	In	Out	In	Out	In	Out	In	Out	In	Out	In	Out
$P_T \left[\frac{N}{m^2}\right]$	200 000	226 440	226 190		250 350		249 260		265 910		265 000	
$T_T \, [K]$	300.00	311.47	311.47		321.02		321.02		327.32		327.32	
$V \left[\frac{m}{s}\right]$	93.31	110.27	119.43		154.43		111.05		128.00		105.18	
$V_m \left[\frac{m}{s}\right]$	93.31	86.92	105.18		105.18		105.18		105.18		105.18	
$V_t \left[\frac{m}{s}\right]$	0.00	67.86	56.58		113.07		35.63		72.95		0.00	
$\alpha \, [°]$	0.00	37.98	28.28		47.07		18.71		34.74		0.00	
$W \left[\frac{m}{s}\right]$	193.61	133.85	154.43		119.43		170.37		142.88		/	
$W_t \left[\frac{m}{s}\right]$	-169.65	-101.79	-113.07		-56.58		-134.02		-96.70		/	
$\beta \, [°]$	-61.19	-49.51	-47.07		-28.28		-51.88		-42.59		/	
$M \, [-]$	0.27	0.31	0.34		0.44		0.31		0.36		0.29	
$M_w \, [-]$	0.56	0.38	0.44		0.34		0.48		0.40		/	
$\bar{\omega} \, [-]$	0.037		0.017		0.033		0.035		0.023		0.041	

Table 2.12: Percentage error of 3D CFD simulation compared to the meanline code for compressor mode.

Parameter	Rotor 1		Stator 1		Rotor 2		Stator 2		Rotor 3		Stator 3	
	In	Out	In	Out	In	Out	In	Out	In	Out	In	Out
$P_T \left[\frac{N}{m^2}\right]$	0.00%	0.21%	0.04%		0.23%		0.01%		0.80%		1.11%	
$T_T \, [K]$	0.00%	0.06%	0.08%		0.13%		0.16%		0.08%		0.07%	
$V \left[\frac{m}{s}\right]$	0.19%	2.69%	0.16%		0.31%		4.80%		4.37%		5.45%	
$V_m \left[\frac{m}{s}\right]$	0.19%	3.00%	0.62%		1.38%		2.27%		3.26%		5.18%	
$V_t \left[\frac{m}{s}\right]$	/	0.64%	3.54%		1.06%		23.49%		5.20%		/	
$\alpha \, [°]$	/	1.69%	3.53%		1.48%		18.88%		1.44%		/	
$W \left[\frac{m}{s}\right]$	0.44%	1.86%	1.70%		2.10%		2.45%		0.53%		/	
$W_t \left[\frac{m}{s}\right]$	0.49%	0.54%	2.49%		3.38%		5.65%		3.06%		/	
$\beta \, [°]$	0.12%	1.38%	1.12%		1.66%		4.36%		4.22%		/	
$M \, [-]$	0.24%	2.76%	0.16%		0.31%		4.89%		4.59%		5.70%	
$M_w \, [-]$	0.49%	1.95%	1.71%		2.10%		2.38%		0.76%		/	
$\bar{\omega} \, [-]$	8.7%		21.8%		12.7%		1.97%		13.4%		62.1%	

The considerations done for the quasi-3D simulation are repeated, since the results are very similar: the results are accurate up to the outlet of the middle stator, where they start

to diverge. Nevertheless, η_{TTis} is of 90.5% compared to 88.6% of the meanline predictions, and the total pressure prediction at the outlet has an error of 1.1%. Therefore the global characteristics of the machine are met with reasonable errors.

2.4.2. Turbine Code Validation

Once the compressor is verified, the same procedure can be performed for the turbine mode.

The mesh used is the same, it is just reversed the direction of the flow. The boundary conditions imposed change only at the inlet: $P_T = 265000$ Pa and $T_T = 326.2$ K. The same $\dot{m}$ is imposed as well as the same wall conditions. A fully 3D simulations are performed on all the machine.

As explained in section 1.2, the i is negative for all the cascades. Other than the reason already described, there's an influence also from the δ. Since a design code is used for the compressor mode, the blade geometry is purely a consequence of the compressor behaviour in terms of δ and i. In fact, the blade angle at the outlet of a cascade is obtained from the flow angle and δ for compressor mode, as shown in Figure 2.23.
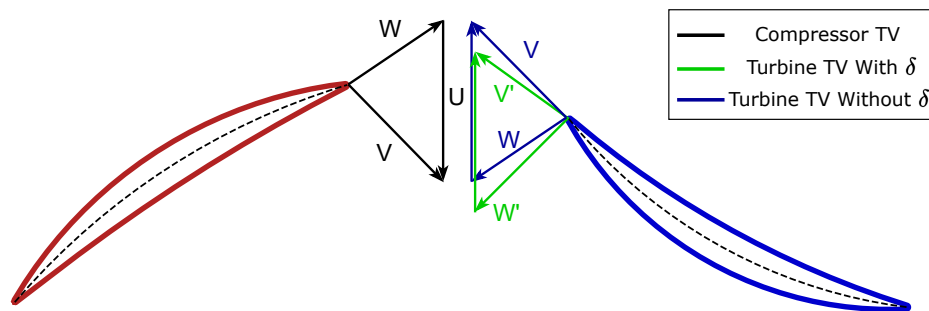
Figure 2.23: Velocity triangles for compressor and turbine mode

When reversing the flow, if it is considered an ideal turbine cascade with δ equal to 0, the flow enters the compressor cascade already with a negative i (The compressor TV and turbine TV are the same). When, instead, δ is the real one, this situation worsens, increasing the value of the negative i on the successive blade. This effects is also present at the first cascade, for which the blade angle is different than 0 to account for the compressor δ. The comparison between the meanline code and the 3D simulation are shown in Table 2.13.

Table 2.13: 3D CFD simulation results for turbine mode.

Parameter	Rotor 1		Stator 1		Rotor 2		Stator 2		Rotor 3		Stator 3	
	In	Out	In	Out	In	Out	In	Out	In	Out	In	Out
$P_T \left[\frac{N}{m^2}\right]$	265001	264219	257222		240457		240542		239803		209753	
$T_T \ [K]$	326.17	326.18	324.00		324.02		318.57		318.60		310.14	
$V \left[\frac{m}{s}\right]$	113.13	127.56	120.66		152.76		131.99		117.22		115.70	
$V_m \left[\frac{m}{s}\right]$	113.13	113.23	111.53		111.16		110.19		91.56		115.20	
$V_t \left[\frac{m}{s}\right]$	0.00	58.58	45.47		104.67		72.22		72.69		-10.40	
$\alpha \ [°]$	0.00	27.36	22.18		43.28		33.24		38.45		-5.16	
$W \left[\frac{m}{s}\right]$	/	158.97	167.34		129.21		147.63		134.28		213.70	
$W_t \left[\frac{m}{s}\right]$	/	-111.40	-124.61		-65.46		-97.98		-97.60		-180.00	
$\beta \ [°]$	/	-44.53	-48.17		-30.49		-41.64		-46.83		-57.38	
$M \ [-]$	0.32	0.36	0.34		0.43		0.37		0.33		0.34	
$M_w \ [-]$	/	0.44	0.47		0.36		0.42		0.38		0.63	
$\bar{\omega} \ [-]$	0.030		0.022		0.028		0.025		0.030		0.058	

Table 2.14: Meanline code results for the 3D CFD simulation for turbine mode.

Parameter	Rotor 1		Stator 1		Rotor 2		Stator 2		Rotor 3		Stator 3	
	In	Out	In	Out	In	Out	In	Out	In	Out	In	Out
$P_T \left[\frac{N}{m^2}\right]$	265000	264410	245870		244450		219910		218930		186060	
$T_T \ [K]$	326.17	326.17	321.46		321.46		312.09		312.09		298.37	
$V \left[\frac{m}{s}\right]$	113.06	130.36	121.18		164.50		132.15		115.27		165.18	
$V_m \left[\frac{m}{s}\right]$	113.06	113.23	115.47		117.06		117.66		96.95		139.26	
$V_t \left[\frac{m}{s}\right]$	0.00	64.60	36.78		115.58		60.16		62.36		-88.83	
$\alpha \ [°]$	0.00	29.71	17.67		44.64		27.08		32.75		-32.53	
$W \left[\frac{m}{s}\right]$	/	154.45	176.02		128.94		160.72		144.60		293.61	
$W_t \left[\frac{m}{s}\right]$	/	-105.05	-132.86		-54.06		-109.48		-107.29		-258.48	
$\beta \ [°]$	/	-42.85	-49.01		-24.79		-42.94		-47.90		-61.69	
$M \ [-]$	0.32	0.36	0.34		0.47		0.38		0.33		0.50	
$M_w \ [-]$	/	0.43	0.50		0.37		0.46		0.41		0.89	
$\bar{\omega} \ [-]$	0.026		0.113		0.042		0.018		0.062		0.024	

Table 2.15: Percentage error of 3D CFD simulation compared to the meanline code for turbine mode.

Parameter	Rotor 1		Stator 1		Rotor 2		Stator 2		Rotor 3		Stator 3	
	In	Out	In	Out	In	Out	In	Out	In	Out	In	Out
$P_T \left[\frac{N}{m^2}\right]$	0.00%	0.07%	4.62%		1.63%		9.38%		9.53%		12.73%	
$T_T \ [K]$	0.00%	0.00%	0.79%		0.80%		2.08%		2.09%		3.94%	
$V \left[\frac{m}{s}\right]$	0.06%	2.15%	0.43%		7.14%		0.12%		1.70%		29.96%	
$V_m \left[\frac{m}{s}\right]$	0.06%	0.00%	3.41%		5.04%		6.35%		5.55%		17.28%	
$V_t \left[\frac{m}{s}\right]$	/	9.32%	23.60%		9.44%		20.05%		16.58%		88.29%	
$\alpha \ [°]$	/	7.91%	25.51%		3.05%		22.74%		17.40%		84.14%	
$W \left[\frac{m}{s}\right]$	/	2.93%	4.93%		0.21%		8.15%		7.14%		27.22%	
$W_t \left[\frac{m}{s}\right]$	/	6.04%	6.21%		21.07%		10.51%		9.03%		30.36%	
$\beta \ [°]$	/	3.92%	1.71%		23.00%		3.02%		2.24%		6.98%	
$M \ [-]$	0.11%	2.16%	0.80%		7.76%		1.13%		0.72%		32.63%	
$M_w \ [-]$	/	2.91%	5.28%		0.46%		9.07%		8.04%		29.97%	
$\bar{\omega} \ [-]$	15.1%		80.7%		32.1%		45.1%		50.6%		144.6%	

The negative incidence situation somehow is compensated by the increased losses due to this i effect. The higher losses reduces the total pressure and so ρ, which in turn accelerates the flow to match the same $\dot{m}$. A higher V_m is able to increase the i value, and even bring it to be positive for the latter cascades.

Globally, however, the results are much less accurate than the compressor one. The reasons might be in the wrong predictions of the loss coefficient for i different than 0, but also in the δ calculation. The correlation used for δ depends only on geometrical parameters of the blade, and δ does not change depending on the different blade loading of successive cascades due to incidence mismatch.

Conventional turbine blades are characterised by high deflections, therefore small variations on i are usually irrelevant. For this type of machines the deflection is the same as a conventional compressor, therefore the same small variations on i affect more substantially the fluidynamic.

However, the effects described seems not to be relevant when simulating the cascade using CFD, as can be seen in Figure 2.24, which represent the streamlines for the 3D simulation taken at midspan.

Figure 2.24: Streamlines for turbine mode.
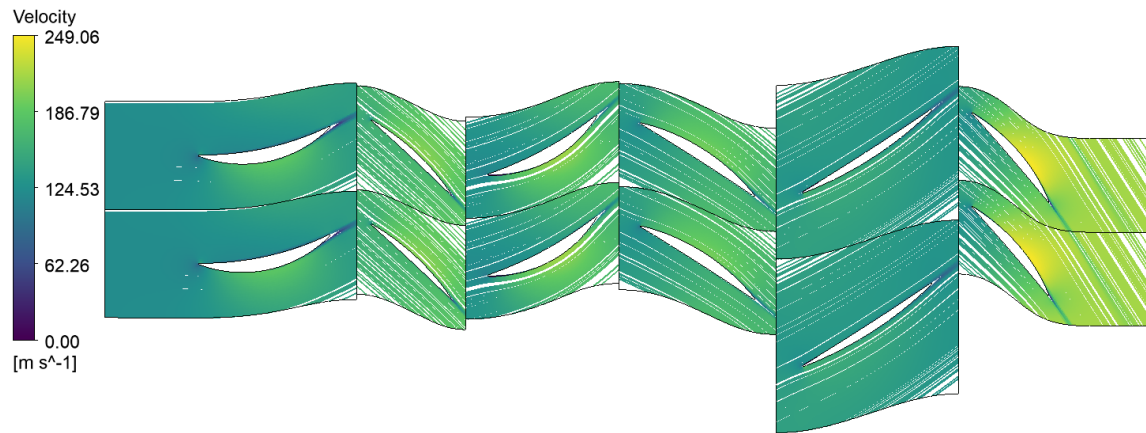
The significant mismatch between CFD and meanline results means that the latter cannot be used to predict accurately the machine performance. Therefore only the compressor meanline code will be used in conjunction with an optimisation routine, to obtain the final machines. The turbine mode is only analysed through CFD simulations.

3 | Reversible Turbomachinery Optimisation

The aim of the meanline validation performed in section 2.4 was to understand if the meanline codes are accurate with respect to CFD simulations. If both the codes are accurate, their calculations can be coupled with an optimisation routine, in order to maximise the efficiency of the machine in both operating modes.

It is resulted that only the compressor code is able to predict well the global behaviour of the machine, hence the optimisation can only work on the compressor functioning mode. The turbine mode performance will be assessed through high-fidelity CFD simulations.

3.1. Optimisation Routine Implementation

The optimisation is carried out through the differential evolution (DE) algorithm, which is implemented in Python through the SciPy library. DE allows to improve a candidate solution for the problem, finding its minimum. This algorithm is chosen because it does not require the problem to be differentiable or even continuous. Moreover, in contrast to gradient-based methods, DE avoids being trapped in local minimums. On the other hand, it cannot guarantee to find the optimal solution.

The algorithm tries different compressor designs, changing the input parameters of the meanline code (from now on referred to as optimisation variables) to find the optimal machine in terms of efficiency.

The optimisation is carried out for both the rotors and stators machine and the one with guide vanes, in order to understand the differences in the behaviour, and whether one or the other is more suitable for this kind of application.

The optimisation variables for the rotors and stators machine are:

1. Mean diameter D_m

2. Flow coefficient ϕ for all the stages

3. Reaction degree χ for first and last stage

4. Work coefficient λ for all the stages

5. Solidity σ for all the stages

In case of the machine with guide vanes the optimisation variables are:

1. Mean diameter D_m

2. Flow coefficient ϕ for the repeated stages

3. Solidity σ for all the stages

The number of stages, being an integer number, is not used as a variable of the optimisation problem, but it is chosen prior to the optimisation.

The design space available is limited by bounding the values of the optimisation variables to values of interest for this application. The full details of the optimisation variables for the rotors and stators machine and the machine with guide vanes are shown, respectively, in Table 3.1 and Table 3.2.

Table 3.1: Optimisation variables for the rotors and stators machine

Variable	Bounds
Mean diameter D_m	(1250, 2500)
Flow coefficient for the first stage ϕ_1	(0.3, 0.9)
Flow coefficient for the repeated stages ϕ_i	(0.3, 0.9)
Flow coefficient for the last stage ϕ_n	(0.3, 0.9)
Reaction degree for the first stage χ_1	(0.2, 1.0)
Reaction degree for the last stage χ_n	(0.2, 0.9)
Work coefficient for the first stage λ_1	(0.2, 0.45)
Work coefficient for the last stage λ_n	(0.2, 0.45)
Solidity for the first rotor σ_1	(1, 1.2)
Solidity for the first stator σ_2	(1, 1.2)
Solidity for the repeated stages σ_i	(1, 1.2)
Solidity for the last rotor σ_{2n-1}	(1, 1.2)
Solidity for the last stator σ_{2n}	(1, 1.2)

Table 3.2: Optimisation variables for the machine with guide vanes

Variable	Bounds
Mean diameter D_m	(1250, 2500)
Flow coefficient for the repeated stages ϕ_i	(0.3, 0.9)
Solidity for the IGV σ_{IGV}	(1, 1.2)
Solidity for the repeated stages σ_i	(1, 1.2)
Solidity for the OGV σ_{OGV}	(1, 2)

λ for the first and last stage is limited to 0.45 due to the criticality of their design. The minimum diameter is taken as 1250 mm in order to ensure an adequate peripheral velocity ($200 \ \frac{m}{s}$) at midspan to lower the deflection needed. The upper limit for σ_{OGV} is taken as 2 to ensuring compliance with Howell limit on deflection for every blade height.

The objective function chosen is the compressor isentropic efficiency η_{is}, corrected with some penalties. These penalties are required in order to avoid some designs that are problematic for this kind of application, such as high loading, DCA blades too thin, as well as impossible designs, such as $\eta_{is} < 0$ or blades touching at the hub. The penalties chosen are:

- if the code is not able to find a solution, the value of 0.1 is provided in the place of η_{is}

- if η_{is} is greater than 1 (due to convergence issues), the value of 0.1 is provided in its place

- if any blade thickness is lower than 0 or not a number, the value of 0.1 is provided in the place of η_{is}

- if blades touch at the hub, due to the hub diameter being too low or the blade number too high, the value of 0.1 is provided in the place of η_{is}

- if the peripheral velocity at the tip of the first rotor exceeds $450 \ \frac{m}{s}$, the value of 0.1 is provided in the place of η_{is}. This is done to avoid excessive mechanical stresses on the blades

- if the first stator of the rotors and stators machine, which is the most critical one, does not act as a compressor one (pressure decreases or the angle is more tangential), the efficiency obtained is lowered by 0.15

- if the pressure increase for the first stator of the rotors and stators machine is due to the blade height increasing, the efficiency obtained is lowered by 0.2

- if any *while* loop has not reached convergence, the efficiency obtained is lowered by 0.3

- if any Mach number, whether absolute or relative is greater than 0.75, meaning that the compressor is transonic, the efficiency obtained is lowered by 0.15

- if any thickness is lower than 5% of the chord, leading to structural integrity problems, the efficiency obtained is lowered by 0.2 for every blade with that characteristic

- if any λ of the repeated stages is greater than 0.35, the efficiency obtained is lowered by 0.3.

- if the Howell limit on deflection ϵ is not respected at any blade radial coordinate, the efficiency obtained is lowered by 0.1, while if it exceeds 4 degrees, it is lowered by 0.2.

In this way, impossible or problematic designs provide as output a very low efficiency, therefore giving to the optimiser the possibility to look for the optimal solution in other design areas, which are not affected by the penalties.

3.2.   Optimisation of Turbomachinery

Once the optimisation routine is established, the actual machines can be optimised. The input parameters that are not optimised and therefore have to be provided are:

1. inlet total pressure P_{Tin}

2. inlet total temperature T_{Tin}

3. outlet total pressure P_{Tout}

4. mass flow rate $\dot{m}$

5. Aspect ratio AR of the blades

6. working fluid

7. number of stages N_{st}

P_{Tin}, T_{Tin} and P_{Tout} are provided by a in-house code, which is able to calculate all the thermodynamic coordinates of a reversible Brayton cycle for PTES application. The main input required are the mass flow rate of the working fluid and the maximum pressure of the cycle.

The mass flow rate is chosen in order to obtain a target power during charge of 10 MW

for both working fluids. The same charge and discharge time is assumed, therefore the mass flow rate used is the same for charge and discharge mode.

The maximum pressure of the cycle corresponds to the outlet pressure of the compressor in charge mode, and it is an important parameter that influences the power density of the plant. In fact, a higher pressure level can guarantee the circulation of the same mass flow rate of the working fluid with smaller machines.

For the blade chord calculation it was originally chosen the Re_c, taken as $Re_c = 4.5 \cdot 10^5$ in order to match Lieblein's experiments [17]. After running some optimisations, the minimum resulting chord length obtained was around 7mm. This is considered too low for structural and manufacturing reasons (t_{max} would have been 0.7mm), therefore it is imposed a length of 40mm for the chord of the last cascade. The aspect ratio resulted is kept constant for all the other cascades and used to calculate their chord length. In this way Re_c increases, falling outside of Lieblein's experiments [17], but it is not expected to have an influence on the results, since the flow is already fully turbulent.

The machine optimisation is performed for both nitrogen and argon. The choice of the working fluid affects the number of stages, as explained in chapter 1. Therefore the number of stages is chosen in order to obtain an average β_{TT} of around 1.1 for both the working fluids.

A total of 8 machine optimisations are performed: compressor in charge and discharge mode for the two working fluids and for the two types of machine architectures. The input parameters between the two types of machines are the same, therefore only 4 set of variables are required. These are shown in Table 3.3.

Table 3.3: Input parameters for the 4 machine design optimisations.

Input	N_2 Charge	N_2 Discharge	Ar Charge	Ar Discharge
P_{Tin} [bar]	3.389	3.190	4.810	4.527
T_{Tin} [°C]	327.931	-10.070	328.178	-4.417
P_{Tout} [bar]	10	10.625	10	10.625
$\dot{m} \left[\dfrac{kg}{s} \right]$	55	55	110.68	110.68
AR [-]	0.55	0.45	1.1	0.60
N_{st}	12	12	8	8

It can be seen, as already predicted, that for a similar temperature range, the Ar machine has a lower pressure ratio. For the charge mode it is of 2.08, compared to 2.95 for N_2,

while for discharge mode it is 2.35 instead of 3.33. Using the same β_{TT} of 1.1, as already mentioned, N_{st} resulting is of 8 for Ar and 12 for N_2. On the other hand, in order to reach the same power, $\dot{m}$ for Ar is double the one for N_2.

3.3.   Optimisation Results

The results of the optimisations for the rotors and stators machine are shown in Table 3.4.

Table 3.4: Optimisation results for the rotors and stators machine.

Machine	CC N_2	CD N_2	CC Ar	CD Ar
D_m	/	1268	1345	1255
ϕ_1	/	0.51	0.45	0.33
ϕ_i	/	0.55	0.59	0.53
ϕ_n	/	0.71	0.73	0.75
χ_1	/	0.85	0.87	0.87
χ_n	/	0.60	0.60	0.58
λ_1	/	0.43	0.37	0.31
λ_n	/	0.20	0.21	0.20
σ_1	/	1.13	1.16	1.07
σ_2	/	1.14	1.04	1.07
σ_i	/	1.17	1.19	1.11
σ_{2n-1}	/	1.12	1.07	1.03
σ_{2n}	/	1.19	1.18	1.20
η_{is}	/	0.82	0.89	0.83

The machines in the blade-to-blade plane and in 3D are represented in Figure 3.1.

(a) Compressor discharge for nitrogen.

(b) Compressor charge for argon.

(c) Compressor discharge for argon.
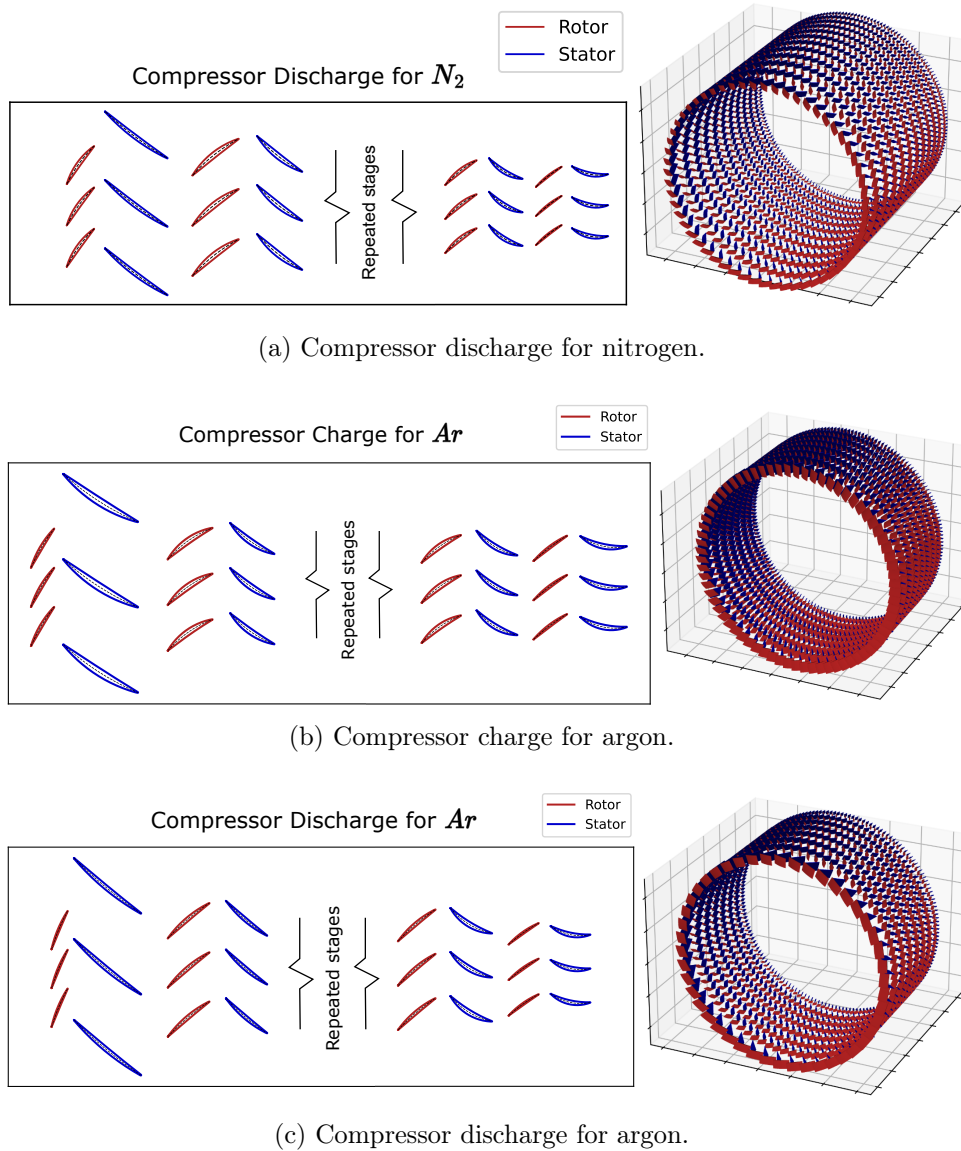
Figure 3.1: Compressor optimum rotors and stators machines.

The optimisation procedure for the compressor in charge mode for N_2 could not find an optimum solution after more than 4 days of computations, so the calculations were stopped and no value is reported in the corresponding column. The other optimisations required about 2 days to be completed.

All the machines are subject to the penalty due to the first stator decreasing the pressure. This is due to its low ϵ, given the high reaction degree, and the fact that the meridional velocity has to increase at the inlet of the successive cascade: the pressure rise given by the stator is compensated by the acceleration of the flow. This condition is particularly prominent in the CD for Ar, which presents also the penalty for the low thickness: both

the first rotor and the first stator present a thickness-to-chord-ratio of 0.048 at the hub. The reason is the low ϵ, which reduces the blade t_{max} to allow its construction. The low ϵ is enhanced by the λ_1 of 0.31, lower with respect to the other machines. This is compensated by the low ϕ_1, since for lower V_m, the ϵ needed for the same ΔV_t is higher. This effect can also be seen in the optimal D_m, which is just slightly above the lower bound in order to increase the ϵ of every cascade and therefore t_{max}.

ϕ for the middle and last stages is very similar for all the machines, as well as λ_n, χ_1 and χ_n.

λ for the repeated stages resulted as:

- 0.282 for CD N_2

- 0.345 for CC Ar

- 0.208 for CD Ar

The hot machine requires more work to compress the hot fluid, despite the lower β_{TT}, that is why its λ is higher. This is in line with the higher D_m resulted for the CC, which is needed to keep λ in the penalty limit of 0.35.

The higher D_m, on the other hand, lowers b for the same required $\dot{m}$. The highest $\dfrac{b}{D_m}$ obtained is of 0.043 at the inlet of CC for Ar. An example of the resulting meridional channel for that machine in shown in Figure 3.2.
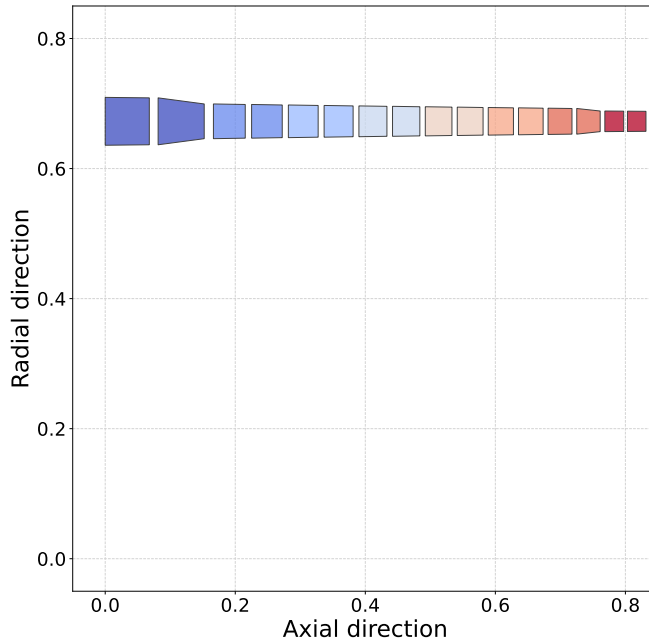
Figure 3.2: Meridional channel for CC Ar

This brings $\bar{\omega}_{ew}$ to be the primary source of loss, contributing for about 50 % of the overall losses for all the machines. To overcome this, a higher $\dot{m}$ should be used to increase b (and power generated).

Mach number is always below 0.5 for all the machines, denoting the low loading characteristic.

The results for the optimisation for the machine with guide vanes are reported in Table 3.5.

Table 3.5: Optimisation results for the machine with guide vanes.

Machine	D_m [mm]	ϕ	σ_{IGV}	σ_i	σ_{OGV}	η_{is}
CC N_2	1775.1	0.4249	1.11	1.12	1.895	0.867
CD N_2	1306.34	0.4239	1.08	1.02	1.96	0.849
CC Ar	1386	0.467	1.05	1.2	1.89	0.896
CD Ar	1301.12	0.456	1.09	1	1.99	0.84

Optimisation for the machine with guide vanes works only on 5 parameters, rather than 13, therefore it requires only around 10 hours to obtain the optimum result.

None of the machines were penalised by critical design features, highlight the simpler design of the machine. This is a first hint on the fact that this type of architecture is better than the previous one.

A representation of the machines in the blade-to-blade plane and in 3D is shown in Figure 3.3.
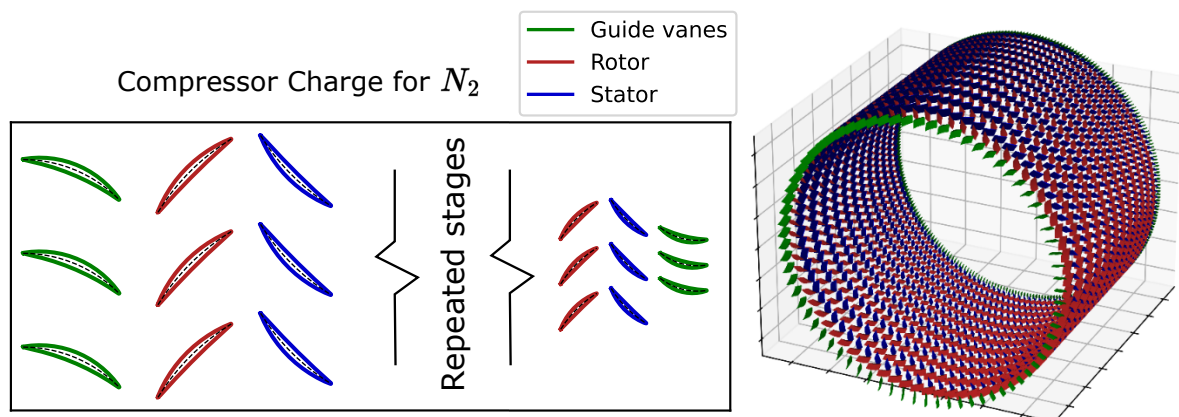
(a) Compressor charge for nitrogen.

Figure 3.3: Compressor optimum guide vanes machines.
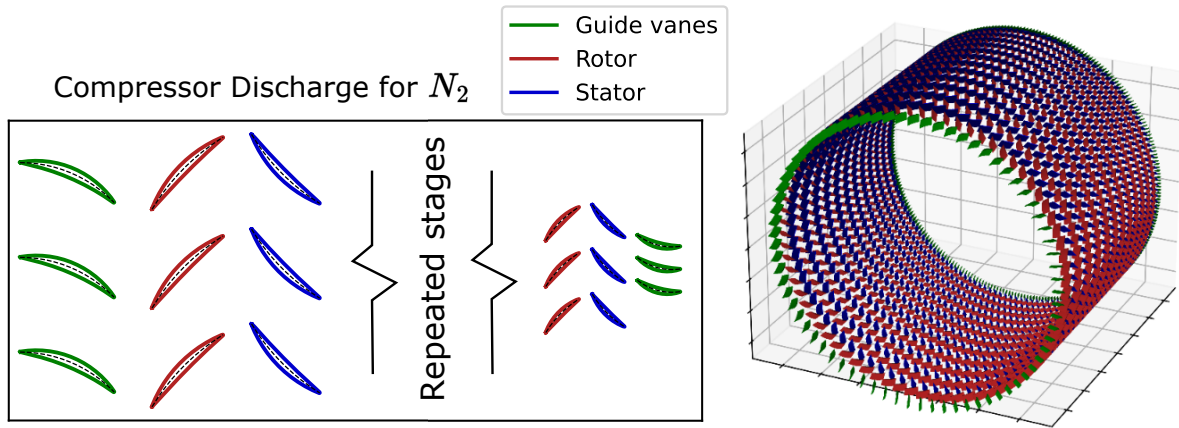
(b) Compressor discharge for nitrogen.
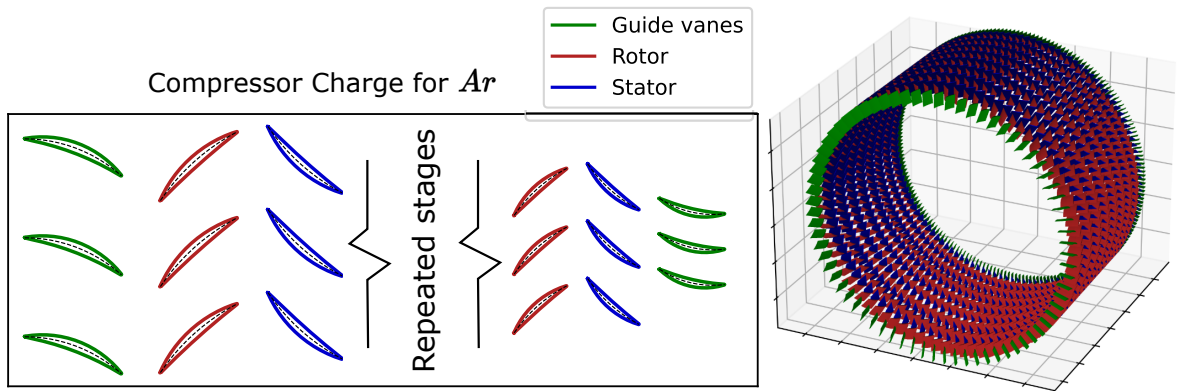
(c) Compressor charge for argon.
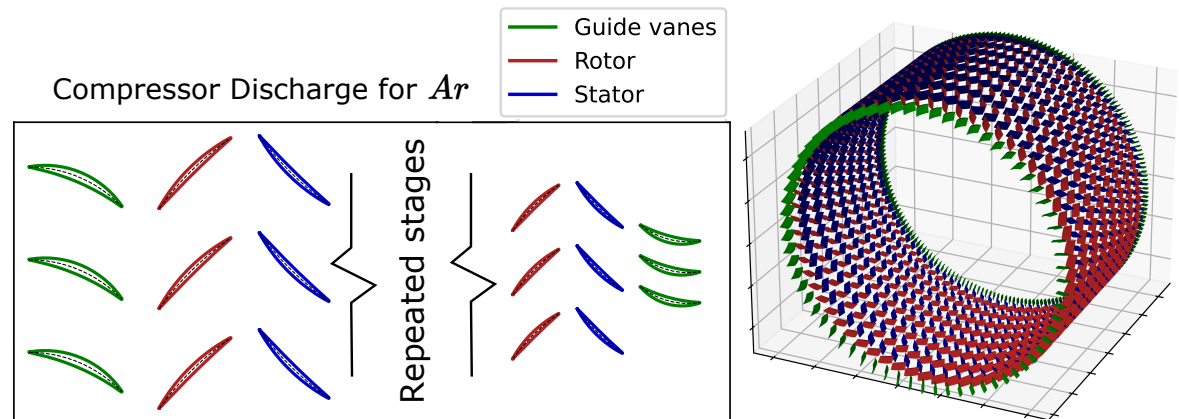
(d) Compressor discharge for argon.

Figure 3.3: Compressor optimum guide vanes machines.

λ of the repeated stages is:

- 0.280 for CC N_2

- 0.265 for CD N_2

- 0.314 for CC Ar

- 0.203 for CD Ar

The same considerations made on the rotors and stators machine on λ and D_m can be done for this machine.

ϕ for the repeated stages is similar between charge and discharge for both N_2 and Ar, with the Ar one being slightly higher.

σ_{OGV} is close to the upper limit for all the machines, which is needed to respect Howell's limit. In fact kinematic deflection for OGV is around 40° for all the machines at midspan. As for the rotors and stators machine, Mach number is below 0.45 for all the machines.

Machines with guide vanes present higher η_{is} compared to the machine with only rotors and stators, as well as not presenting design criticality, therefore it is chosen to analyse only its turbine mode behaviour through CFD simulations.

4 | 3D CFD Analysis

Once the optimal compressor mode geometries are obtained, the corresponding turbine mode are analysed. As explained in section 3.3, the architecture using guide vanes resulted as the most efficient, therefore only this framework is studied through high-fidelity 3D CFD simulations. The aim of these simulations is to understand the fluidynamic when reversing the flow, since the meanline code resulted not accurate.

The boundary conditions of the thermodynamic cycle for the turbine in charge mode (TC) and in discharge mode (TD) for both working fluids are shown in Table 4.1. Turbines are simulated using the same $\dot{m}$ to be coherent with the optimised compressors obtained.

Table 4.1: Boundary conditions applied to CFD simulations.

Parameter	TC N_2	TD N_2	TC Ar	TD Ar
P_{Tin} [bar]	9.604	10.000	9.604	10.000
T_{Tin} [K]	333.176	813.762	333.386	813.246
β_{TT} [K]	2.72	2.95	1.92	2.08
$\dot{m}$	55.0	55.0	110.68	110.68

The meanline code could not provide a solution for the boundary conditions applied, therefore the proper OGV rotation to obtain axial flow at the outlet is not known and, therefore, is not changed.

The computational domain is built as done in section 2.4, using half axial chord between two cascades and a full chord before the first cascade. After the last cascade, it was used a chord and a half, but convergence could not be reached due to the presence of a wake after the OGV. The outlet domain is increased to 3 times the last chord, and cells with growing aspect ratio are used to increase numerical diffusivity and eliminate the wake. The difference between the two meshes can be seen in Figure 4.1.
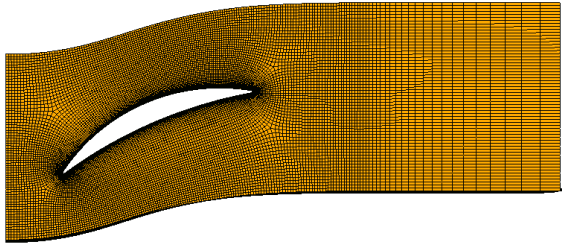
(a) Mesh exceeding one and a half chord.
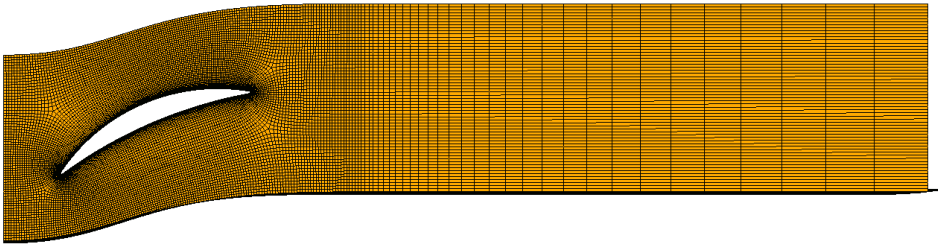
(b) Mesh exceeding three chords.

Figure 4.1: Mesh correction for solving convergence issue due to wake.

In order to reduce the computational effort, the same $k-\omega\,SST$ turbulence model is used, but with the implementation of wall functions, therefore y^+ at the wall has to be at least 50. The mesh number of elements is initially chosen in order to match the same cell size of the grid independent mesh found in section 2.4. However, by doing so, the memory required for the simulations exceeded the limit of the computational resources available. Therefore, the number of cells is reduced, to bring it under $10\,000\,000$. The number of cells per cascade obtained in this way is around $550\,000$ for Ar and around $400\,000$ for N_2. The most coarse mesh that was used for the grid independence study when validating the meanline code in section 2.4 had about $1\,200\,000$ elements and provided a total pressure loss coefficient with an error of the 5.4%. Therefore the numerical error expected for these simulations is greater than this value.

The total number of elements is about half of the one required for Ar machines and about a third for N_2 machines.

The simulations are carried out for all the machines, and they provided similar results, as can be seen in Figure 4.2 for the entropy increase with respect to the inlet one.
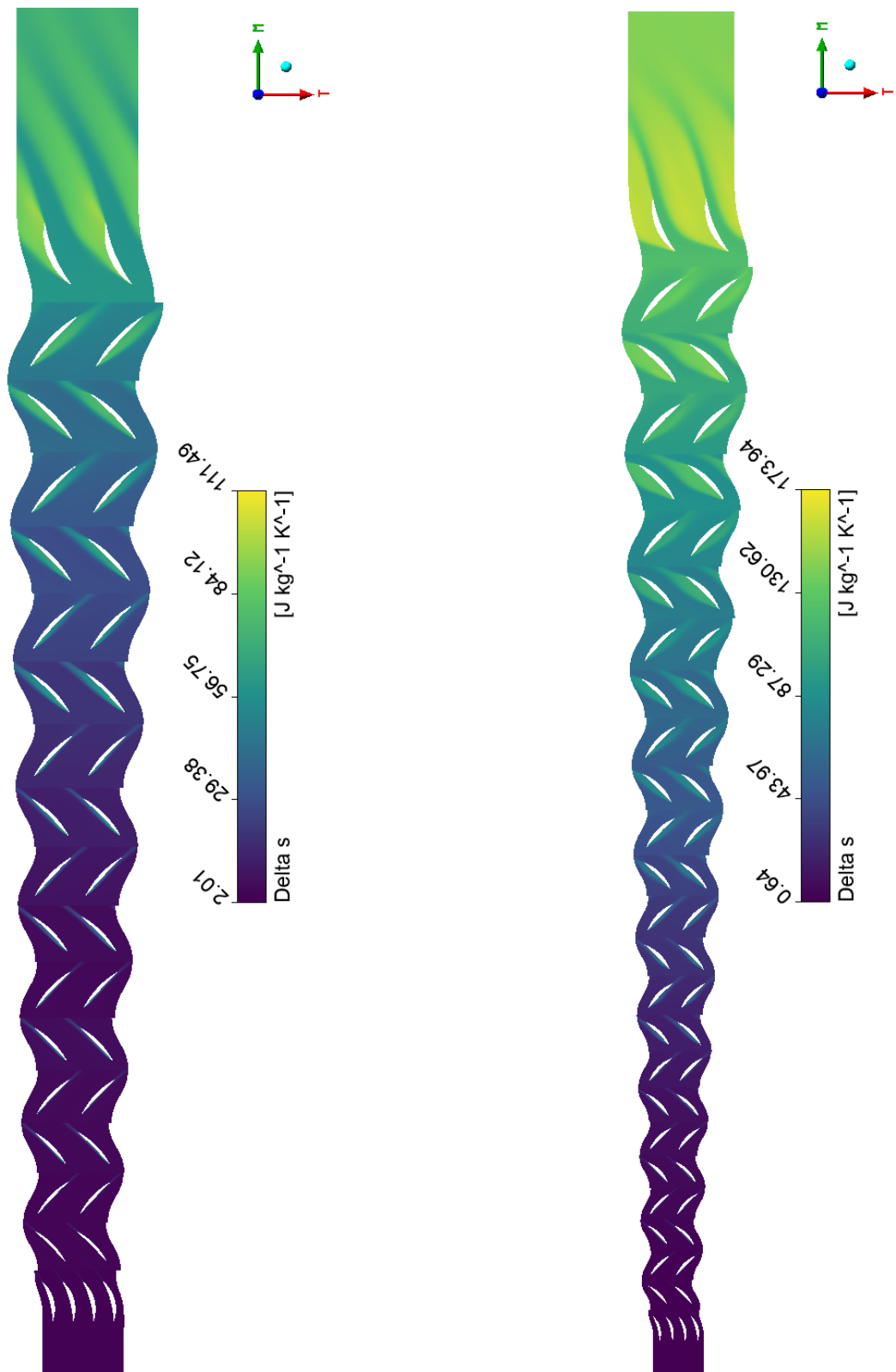
(a) Entropy field for Ar TC.

(b) Entropy field for N_2 TC.

Figure 4.2: Entropy rise in the blade-to-blade plane for both fluids in the TC
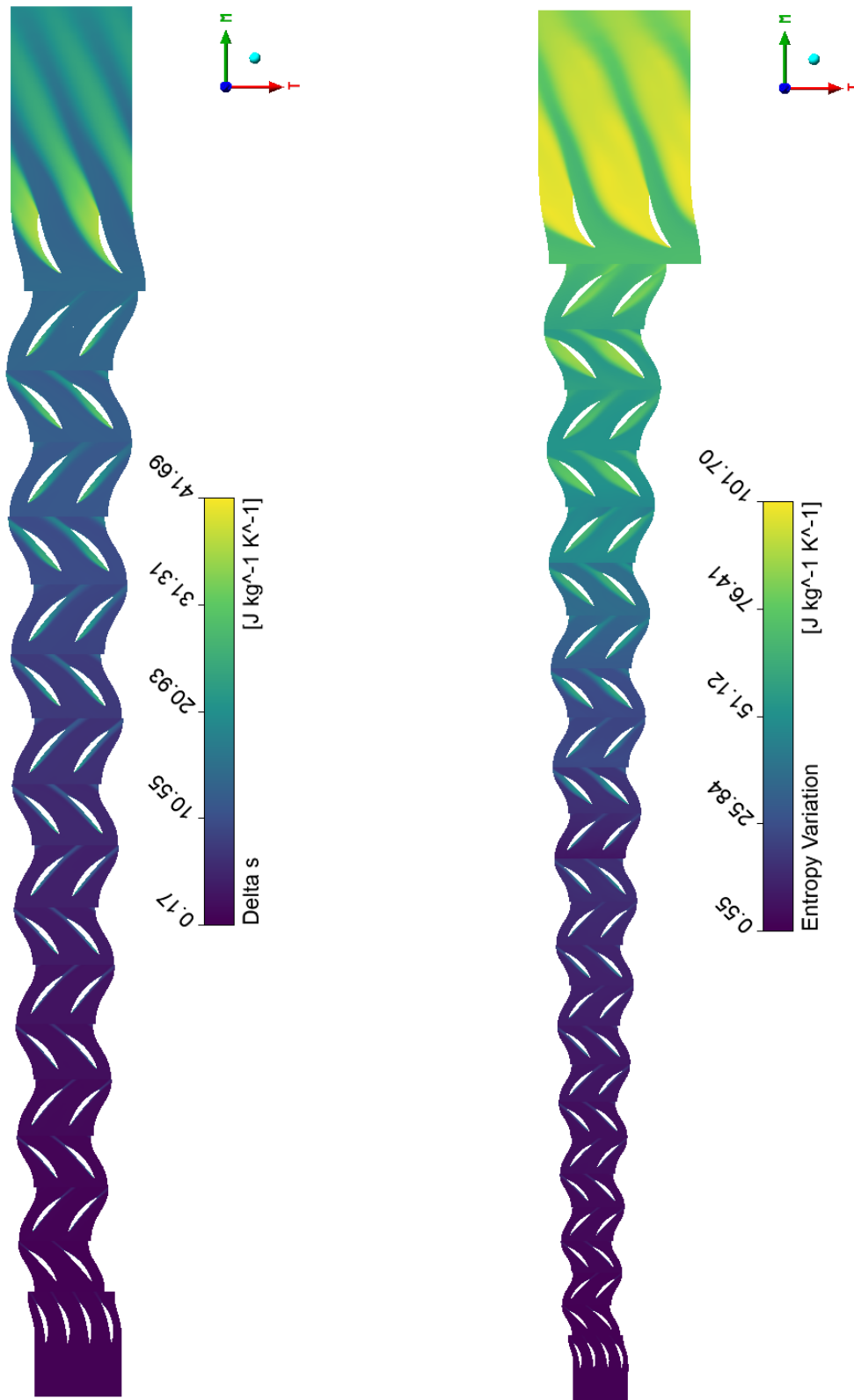
(c) Entropy field for *Ar* TD.

(d) Entropy field for N_2 TD.

Figure 4.2: Entropy rise in the blade-to-blade plane for both fluids in the TD

The graphical results are shown only for the *Ar* TC, but similar considerations can be drawn for the other machines.

As described in section 2.4, a negative incidence is expected on all the cascades. Streamlines of the machine in the blade-to-blade plane at midspan are shown in Figure 4.3.

(e) Streamlines from IGV to the fifth stator.   (f) Streamlines from the fifth rotor to the OGV.
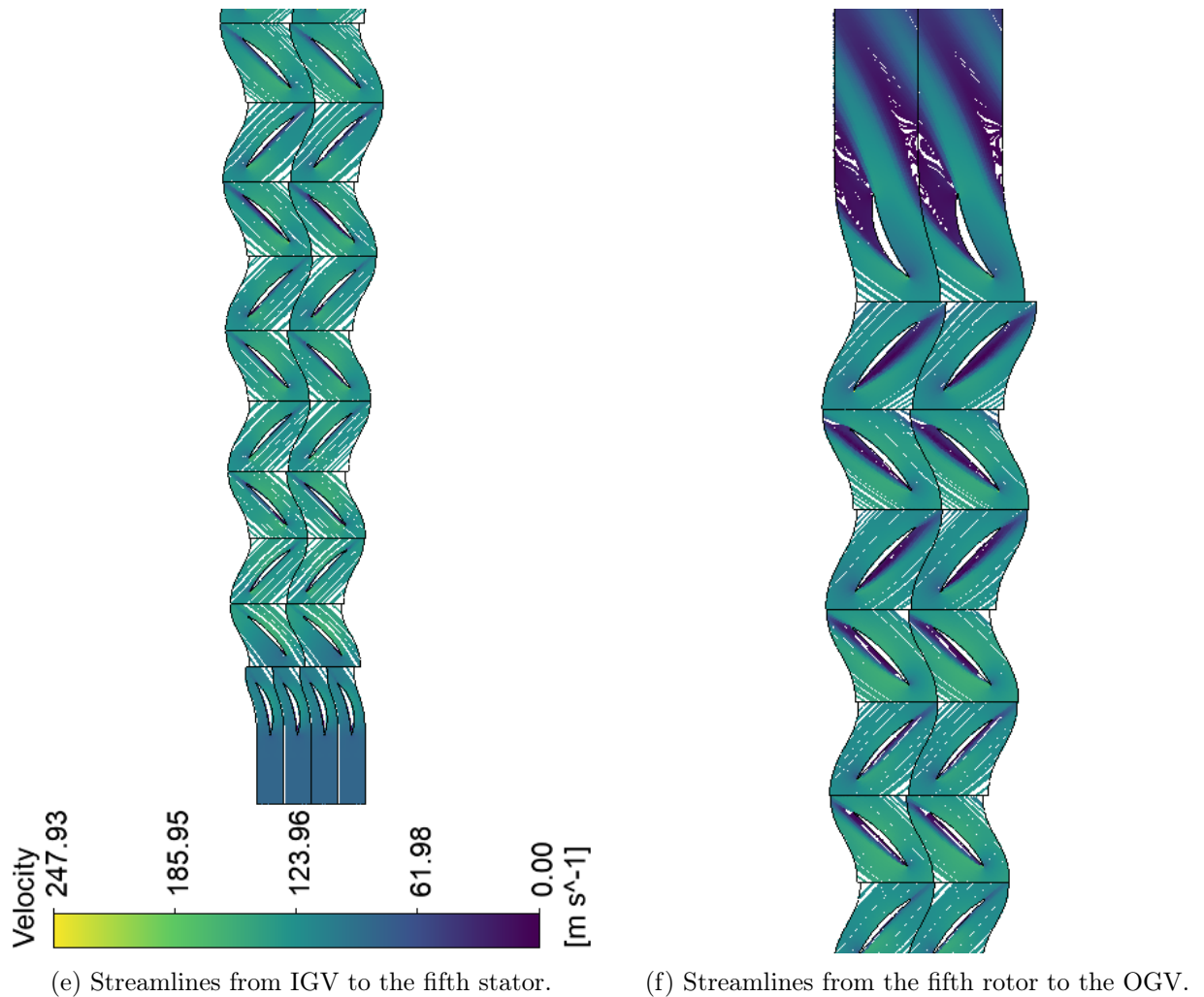
Figure 4.3: Streamlines in the blade-to-blade plane for the *Ar* TD

The predictions are verified: it can be seen a wake zone generated by the negative incidence angle that increases cascade after cascade. Since the OGV has opposite curvature with respect to the stators of the middle stages, the incidence angle there is positive.

The incidence angle along the machines is shown in Figure 4.4.
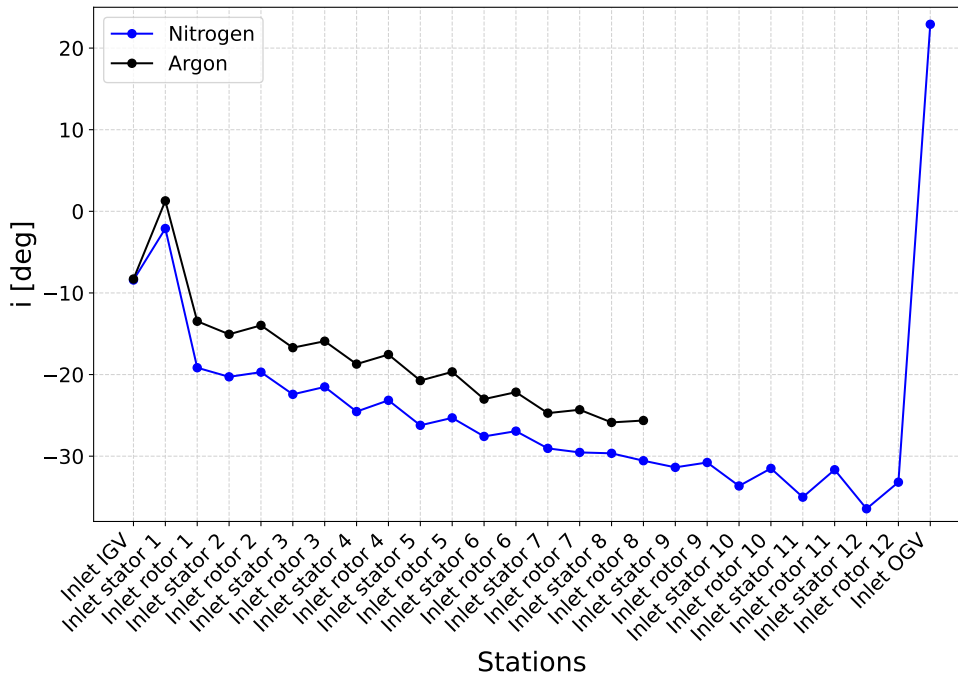
(a) TC trend of i for Ar and N_2.
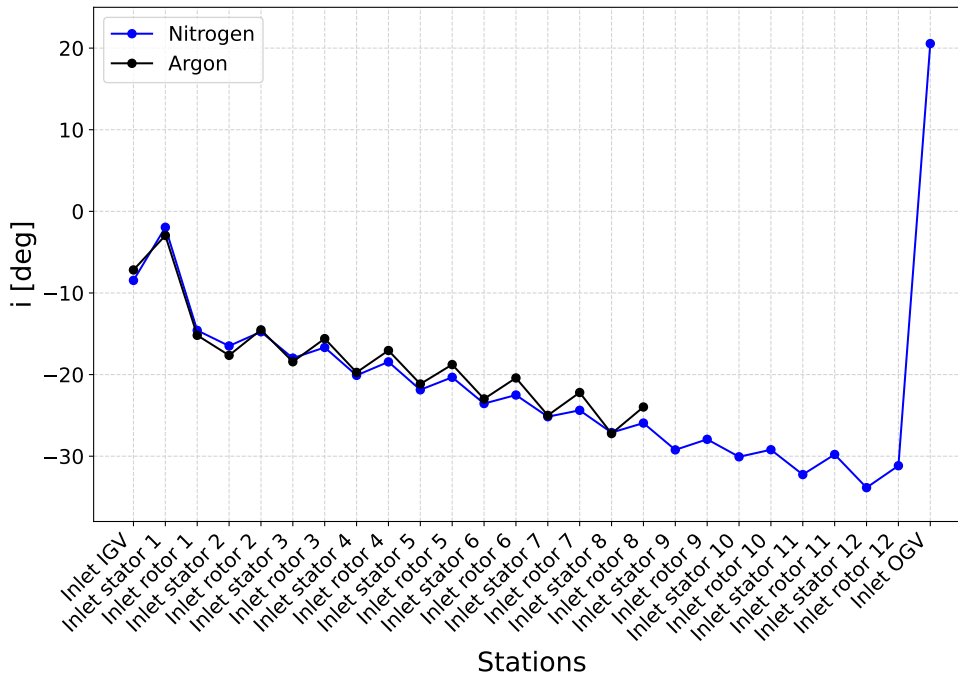
(b) TD trend of i for Ar and N_2.

Figure 4.4: Incidence angle trend for both turbines with both working fluids.

i on the OGV for Ar (not shown) is 14.4° for TC and 14.9° for TD.

The trend is similar between Ar and N_2 machines, both having i more and more negative. This situation provided particular results: the i becomes so negative for TC that the flow

enters the latter cascades with a greater angle than the outlet one, making the rotor blades act as compressor blades, increasing P_T. The trend of P_T can be seen in Figure 4.5 for both the hot and cold turbine.
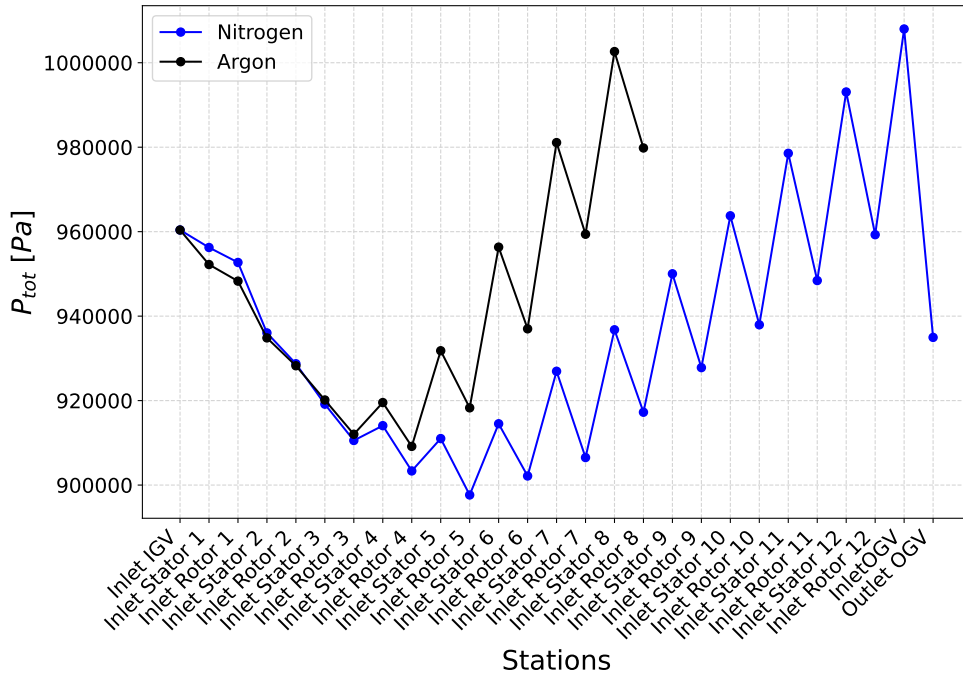
(a) TC trend of P_T for Ar and N_2.
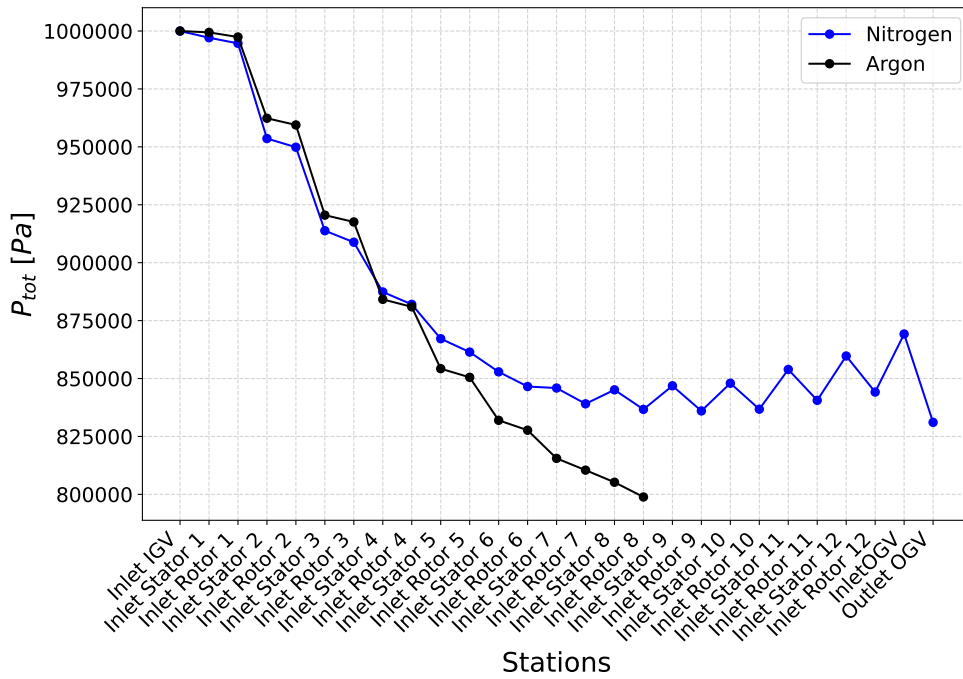
(b) TD trend of P_T for Ar and N_2.

Figure 4.5: Total Pressure trend for both turbines with both working fluids.

P_T at the inlet of the OGV is $1\,007\,920$ Pa for the Ar TC and $800\,155$ Pa for the Ar TD, while P_{Tout} is $962\,834$ Pa for the Ar TC and $779\,833$ Pa for the Ar TD.

For the first two stages of the TC, β_{TT} is approximately constant, with a value of 1.01. For the successive cascades, P_T increases for rotor blades, for the effect explained before, and it decreases for stator blades, due to the total pressure loss.
For the TD, it is observed a β_{TT} always greater than 1 for Ar, with a maximum of 1.04 for the first stage. For N_2, the first β_{TT} is greater than the one for Ar, at 1.05, but the last 5 stages pressurise the flow, with a β_{TT} of 0.99. Again, the rotor blades act as compressor blades, increasing P_T. This effect emphasises the criticality of the TC, due to its different β_{TT} with respect to its compressor counterpart.

This trend is confirmed from λ, which is negative when compression happens. Results are shown in Figure 4.6
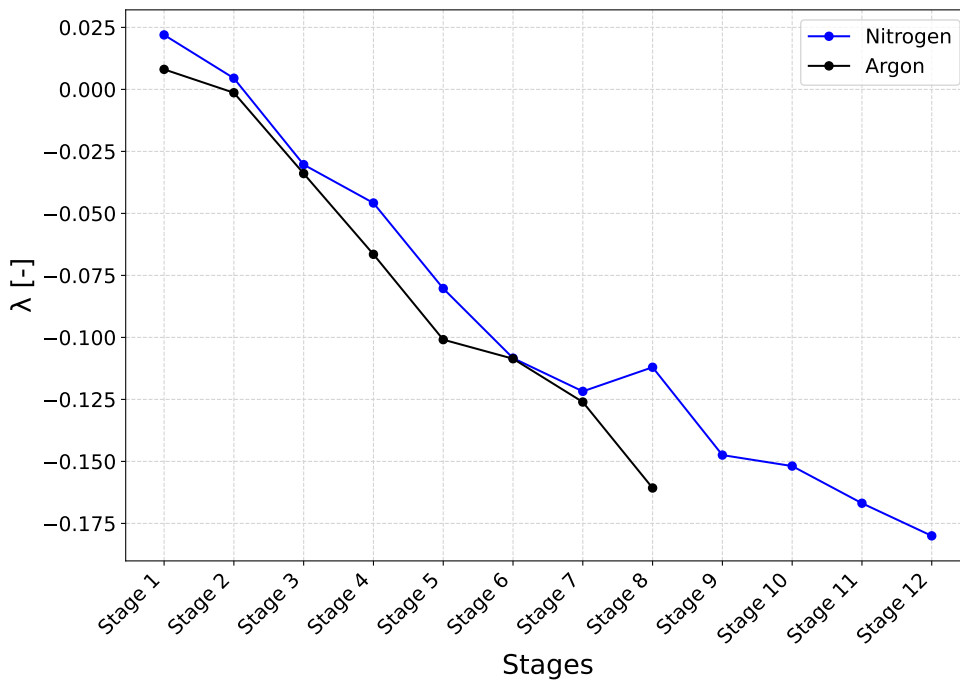
(a) TC trend of λ for Ar and N_2.

Figure 4.6: Work Coefficient trend for both turbines with both working fluids.
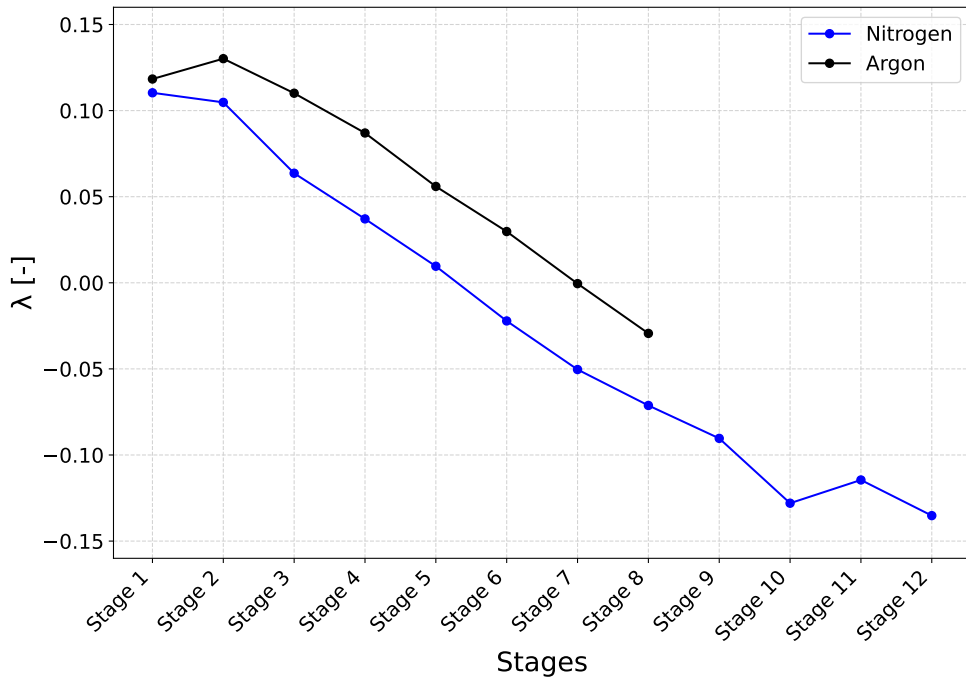
(b) TD trend of λ for Ar and N_2.

Figure 4.6: Work Coefficient trend for both turbines with both working fluids.

Losses present an increasing trend, as is expected for the increasing i. Its values are represented in Figure 4.7.
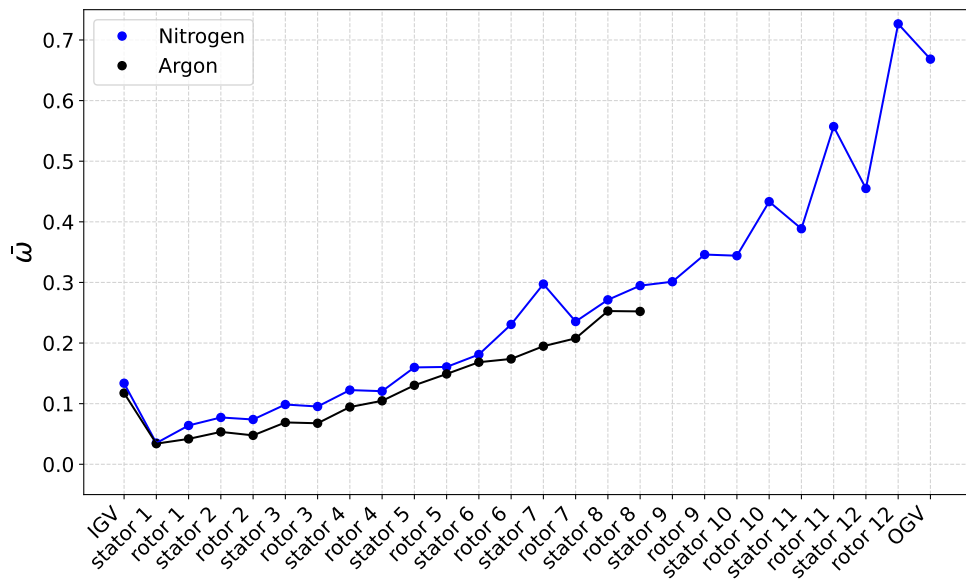
(c) TC trend of $\bar{\omega}$ for Ar and N_2.

Figure 4.7: Total Pressure Loss trend for both turbines with both working fluids.
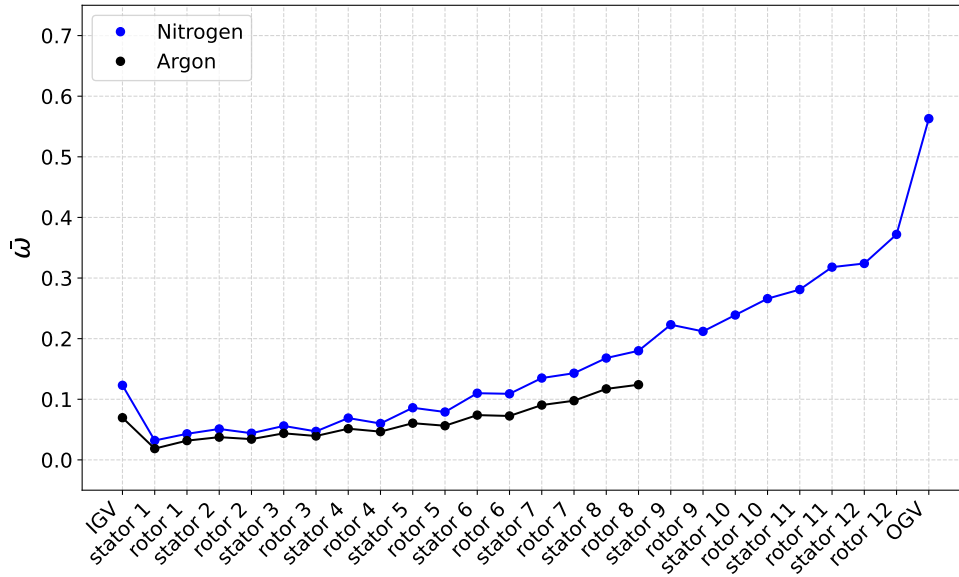
(d) TD trend of $\bar{\omega}$ for Ar and N_2.

Figure 4.7: Total Pressure Loss trend for both turbines with both working fluids.

$\bar{\omega}$ for OGV is 0.4533 for the Ar TC and 0.3874 for the Ar TD.

A way to improve the negative incidence angle is to increase $\dot{m}$. However, this is not trivial. A higher mass flow rate for discharge mode $(\dot{m}_D)$ with respect to the charge mode one $(\dot{m}_C)$ may be considered. By doing so, when operating in charge mode, the compressor is designed for the required $\dot{m}_C$, while the turbine is the reversed CD, which is designed for $\dot{m}_D > \dot{m}_C$. This means that TC has the geometry optimised for $\dot{m}_D$, but it operates with lower $\dot{m}$. This would increase the negative incidence problem. The opposite happens if $\dot{m}_C$ is higher than $\dot{m}_D$.

The maximum Mach number is around 0.42 for both TC, and around 0.35 for both TD. Therefore, there is room for increasing $\dot{m}$ without incurring in transonic behaviour. The full Mach number trend is shown in Figure 4.8.
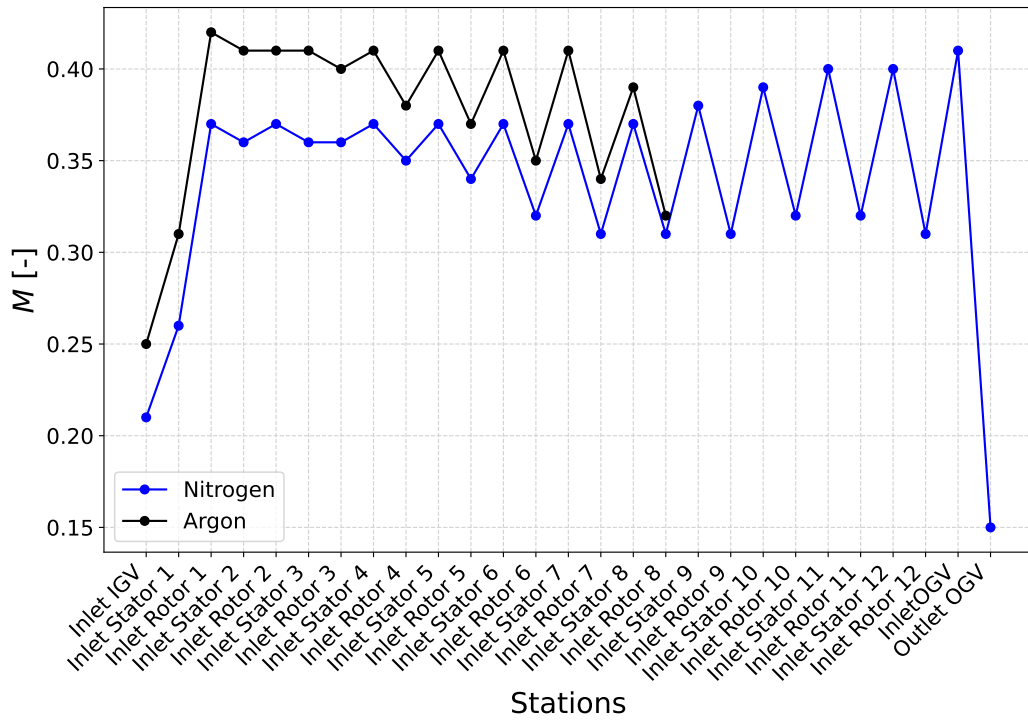
(e) TC trend of M for Ar and N_2.
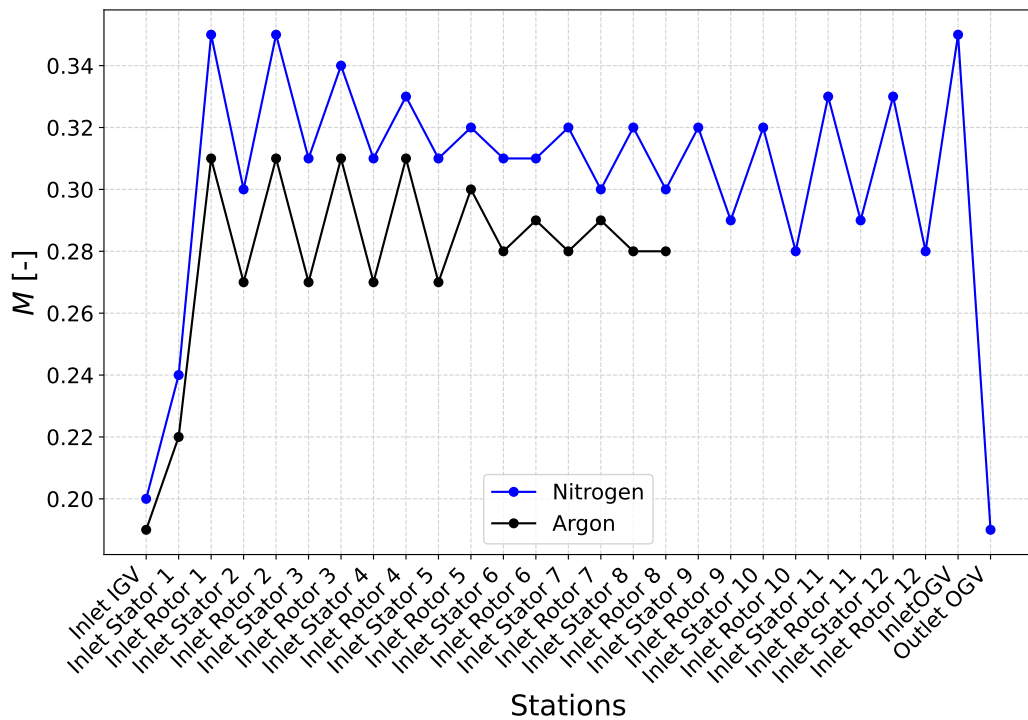
(f) TD trend of M for Ar and N_2.

Figure 4.8: Mach Number trend for both turbines with both working fluids.
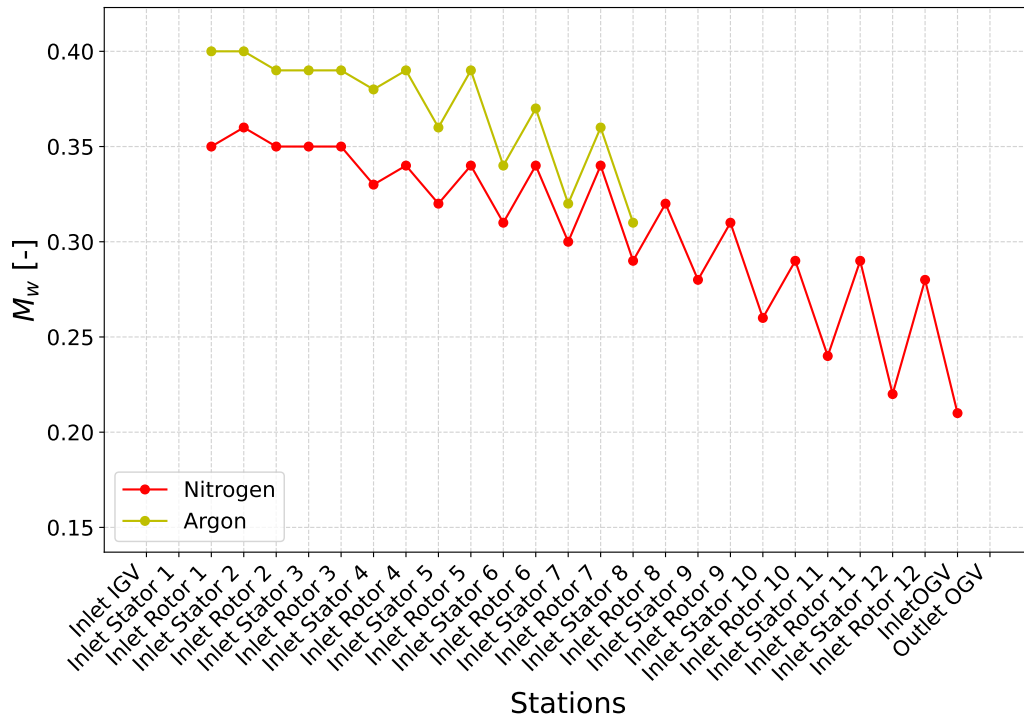
(g) TC trend of M_w for Ar and N_2.
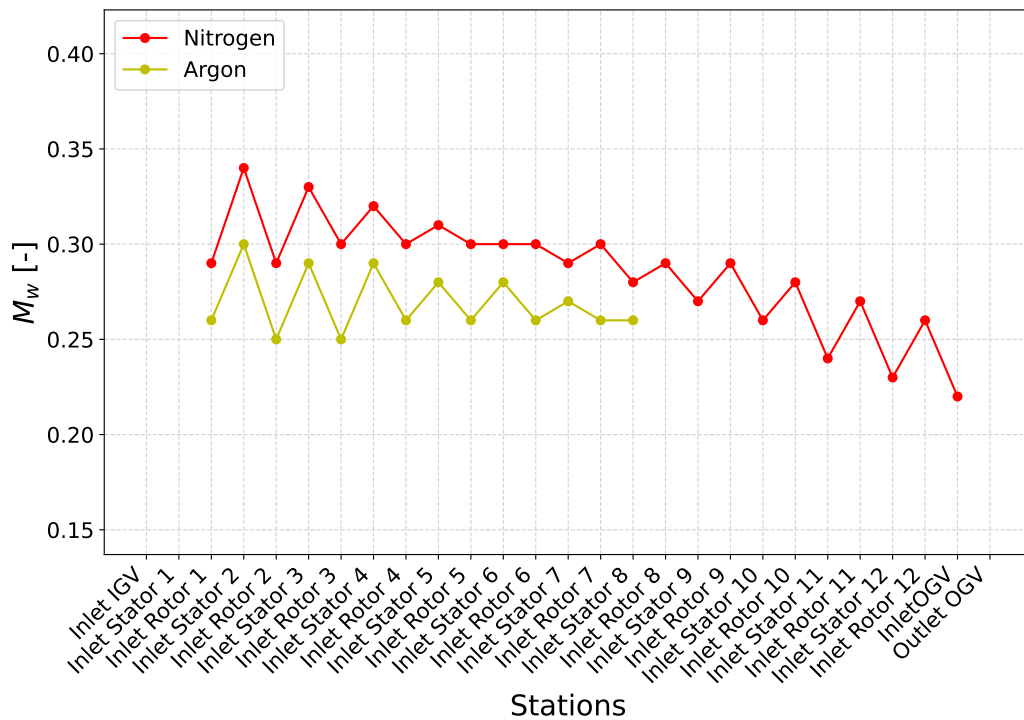
(h) TD trend of M_w for Ar and N_2.

Figure 4.8: Mach Number trend for both turbines with both working fluids.

No machine could expand the fluid as required. P_{Tout} for TC is almost the same as P_{Tin}

because of its increase in rotor rows due to work exchanged and decrease in stator rows due to total pressure losses. For TD the situation is less critical, with all the rotors expanding the flow for Ar. For N_2 only the first 7 rotors are able to expand the flow. Nevertheless, the correct P_{Tout} is not matched even in these cases. For TD Ar it is 7.79 bar compared to the theoretical 4.81 bar, while for TD N_2 it is 8.31 bar compared to 3.389 bar. However, in relative terms, the Ar machine reached 62% of the theoretical β_{TT}, while the N_2 machine only the 40%.

Overall, the two working fluids present a similar trend in all the quantities represented here. Both TC start to pressurise the flow at the third rotor. This means that almost half of the stages for Ar act as turbine, while only a third for N_2. For both machines, Ar has also lower total pressure losses.

D_m for Ar and N_2 TC is similar (respectively 1301 mm vs 1306 mm), while it is different for TD (respectively 1775 mm vs 1386 mm). This causes the λ to be lower and both M and M_w to be higher for TD N_2. For TC λ is similar, while M and M_w present opposite trend: the Ar one is higher.

All these considerations are in favour of choosing Ar as working fluid: higher β_{TT}, higher percentage of stages expanding the flow and lower losses. In order to choose the working fluid, however, other considerations, such as the cost of the heat exchangers should be considered.

Due to the results obtained for the turbines, providing estimates on RTE of the cycle is not meaningful.

Other than increasing $\dot{m}$ for increasing i, another way to increase the efficiency can be represented by pitching the IGV, to set the correct i on the first stator row. While it could make sense for the TCs, the high temperature at the inlet of the TD (more than 800 K) would prevent this option for the latter case due to structural reasons.

5 | Conclusions and Future Work

A new methodology to design and analyse reversible axial turbomachinery for the application on a closed Brayton cycle has been proposed. The main peculiarity of this kind of machine is the fact that the compressor and turbine mode exchange a different amount of work with the fluid. This causes different amount of density change through the machine, therefore different axial velocity variation. It means that both operating modes cannot operate at their optimum efficiency: the passage height variation to provide constant axial velocity for one operating mode does not guarantee constant axial velocity for its counterpart. Therefore, either compressor or turbine mode has to work with incidence angle different than the design one and cannot have repeating stages.

The parameter to optimise should not consequently be the single efficiency of an operating mode, but the round trip efficiency (RTE), which considers the whole plant functioning. In the case studied the hot machines work with the same pressure ratio, while the cold compressor (discharge mode) has to provide a higher pressure ratio than its counterpart (charge turbine). However, this configuration may vary depending on design choices.

Being a closed cycle, it has the advantage of choosing the working fluid to operate with. Two fluids were compared: N_2 and Ar. N_2 as a higher heat capacity, therefore it requires a lower $\dot{m}$ to achieve the same power. On the other hand, Ar, being monoatomic, present a higher heat capacity ratio, therefore to achieve the same temperature difference, it is required a lower pressure ratio. This has the benefit of reducing the number of stages required, therefore reducing the machine cost. However, the heat exchanger would be more costly because Ar is a monoatomic gas.

The design methodology used was to predict both operating modes functioning by developing a code base on a meanline approach. In this way, the calculations could be coupled with an optimisation routine, in order to find the geometry that maximises the RTE. Two codes were developed, one for compressor mode and one for turbine mode. Since compressor functioning is more influenced by variation in the incidence angle, it was decided to compute it at its optimum condition and using a repeating stages approach. The code was therefore a design one, taking as input the thermodynamic conditions at

inlet and outlet, adimensional coefficients and geometrical parameters to calculate the compressor geometry. The turbine code, instead, was an analysis one, which uses the compressor geometry as input and runs the flow backwards, obtaining the performance. The codes exploit specific correlations for compressor and turbines in order to calculate total pressure losses, optimal incidence angle and deviation angle.

The codes could be coupled with the optimiser only if they resulted accurate when compared to high-fidelity CFD simulations. Comparisons were carried out using quasi-3D simulations for verifying the predictions of the midspan fluidynamic and fully 3D for the whole 3D flow field. Only the compressor code resulted accurate, since it was able to match the outlet total pressure and η_{is} with reasonable accuracy (P_{Tout} obtained was of 262055 Pa, compared to 265000 Pa of the meanline code, and η_{is} was 90.5% compared to 88.6%). Turbine code, instead resulted very inaccurate, showing a complete mismatch of both P_{Tout} (209753 Pa of the simulation vs 186060 Pa of the code) and η_{is} (94.3% of the simulation vs 87.6% of the code). The significant mismatch is due to the negative incidence angle present, which effects are not well predicted by the code. In particular, deviation angle correlation does not depend on the incidence angle, but only on geometrical parameters, therefore it is not able to predict accurately the actual behaviour.

This meant that RTE could not be optimised, but only η_{is} of the compressor mode.

Two architectures were compared: one composed by only rotors and stators, the other with guide vanes at the inlet and at the outlet, which simplified the design, since only repeated stages are utilised. These vanes could be rotated, in order to regulate the operation of the turbine mode of the machines. OGV could be pitched in order to achieve fully axial outlet velocity, while a rotation of the IGV could allow design incidence on the first stator. The IGV of the discharge turbine, however, cannot be moved because of the high temperature present.

Due to the low reliability of the turbine code, no rotation is implemented.

The two optimised machines provided comparable efficiencies, but the design of the one with guide vanes was not affected by design criticality. In particular, the machines composed by rotors and stators presented reduced blade thickness and decreasing pressure across the first stator. η_{is} for the machines with guide vanes are of 86.7% for N_2 and 89.9% for Ar in charge mode, while for discharge mode they are 84.9% for N_2 and 84.0% for Ar. This architecture was the one chosen for analysing turbine mode.

As predicted, turbines cascade showed increasing negative incidence angles. Because of this, not only the target outlet pressure could not be reached, but some rotor rows acted as compressor cascades during the turbine mode operation. The incidence was so negative

that the inlet tangential velocity was greater than the outlet one, increasing P_T. This is more significant in the turbine in charge mode, emphasising its criticality.

As the turbine modes were not able to achieve the corresponding operating points, no value of η_{is} for the turbine modes or RTE for the whole plant could be provided.

Nevertheless, Ar machine provided better results in terms of expansion ratio and incidence angle, showing more promising results.

A method to arguably improve the flow condition for turbines is to implement rotating IGV, in order to obtain design incidence angle on the first stator. This solution is only employable for the turbine in charge mode due to the lower inlet temperature.

Another solution is to increase $\dot{m}$, but it is not trivial due to the compressor geometry matching.

5.1. Future Works

This work was the starting point for designing reversible axial turbomachinery. There are different paths that can be pursued in order to improve the design method for this kind of machines:

- improve the meanline analysis code predictions by improving turbine losses and deviation correlations. In particular, there is the necessity of including the influence of the incidence angle on the deviation angle. By doing so, also the turbine code could be coupled together with the compressor one for the optimisation routine, therefore maximising RTE, and not the single machine efficiency

- accounting for spanwise evolution at the meanline level. Flow calculations are performed using a meanline approach, but more accurate results could be obtained by including three-dimensional effects, such as solving the non-isoentropic radial equilibrium for the spanwise distribution of properties

- different design strategy. Operating the compressor at its optimum design point made the turbine work with strong negative incidence. A different spanwise design from the free-vortex method can be also envisaged

- evaluate the benefits of employing rotating IGV for turbine mode, in order to obtain design incidence angle on the first stator.

- consider different rotational speeds for the two operating modes, with the aim of mitigating the negative effects.

Bibliography

[1] European Commission. A european green deal. https://commission.europa.eu/strategy-and-policy/priorities-2019-2024/european-green-deal_en#actions, 2019.

[2] European Commission. Energy scenarios - explore the future of european energy. https://visitors-centre.jrc.ec.europa.eu/en/media/tools/energy-scenarios-explore-future-european-energy.

[3] IEA. Real-time electricity tracker. https://www.iea.org/data-and-statistics/data-tools/real-time-electricity-tracker, 2022.

[4] EASE. Energy storage targets 2030 and 2050. Technical report, EASE, https://ease-storage.eu/, 2022.

[5] EPRI. Electric energy storage technology options: A primer on applications, costs & benefits - an epri executive summary. Technical Report 000000000001022261, EPRI, The address of the publisher, 12 2010.

[6] M. Aneke and M. Wang. Energy storage technologies and real life applications – a state of the art review. *Applied Energy*, 179:350–377, 2016. ISSN 0306-2619. doi: https://doi.org/10.1016/j.apenergy.2016.06.097.

[7] P. Farrés Antúnez. *Modelling and development of thermo-mechanical energy storage*. PhD thesis, University of Cambridge, https://www.cam.ac.uk/, 9 2018.

[8] R. Laughlin. Pumped thermal grid storage with heat exchange. *Journal of Renewable and Sustainable Energy*, 9:044103, 07 2017. doi: 10.1063/1.4994054.

[9] A. Benato and A. Stoppato. Pumped thermal electricity storage: A technology overview. *Thermal Science and Engineering Progress*, 6:301–315, 2018. ISSN 2451-9049. doi: https://doi.org/10.1016/j.tsep.2018.01.017.

[10] J. D. Chiapperi. Attributes of bi-directional turbomachinery for pumped thermal energy storage. Master's thesis, Massachussetts Institute of Technology, https://www.mit.edu/, 5 2021.

[11] Harris P., T. Wolf, J. Kesseli, and R. B. Laughlin. An Investigation of Reversing Axial Turbomachinery for Thermal Energy Storage Application. volume 5: Controls, Diagnostics, and Instrumentation; Cycle Innovations; Cycle Innovations: Energy Storage of *Turbo Expo: Power for Land, Sea, and Air*. ASME, 09 2020. doi: 10.1115/GT2020-15286. V005T07A003.

[12] S. Korpela. *Principles of Turbomachinery*, volume 108. John Wiley & Sons, Inc, 11 2011. ISBN 9780470536728. doi: 10.1002/9781118162477.ch12.

[13] R. H. Aungier. *Axial-Flow Compressors*. ASME Press, 01 2003. ISBN 0791801926. doi: 10.1115/1.801926.

[14] S. Lieblein. Loss and stall analysis in compressor cascades. *Journal of Basic Engineering*, 81:387–397, 1959.

[15] A. R. Howell. Fluid dynamics of axial compressors. *Proceedings of the Institution of Mechanical Engineers*, 153(1):441–452, 1945. doi: 10.1243/PIME_PROC_1945\ _153_049_02.

[16] *Transonic Axial Compressors Loss Correlations: Part I — Analysis and Update of Loss Models*, volume Volume 2A: Turbomachinery of *Turbo Expo: Power for Land, Sea, and Air*, 09 2020. doi: 10.1115/GT2020-14713. V02AT32A029.

[17] S. Lieblein. Incidence and Deviation-Angle Correlations for Compressor Cascades. *Journal of Basic Engineering*, 82(3):575–584, 09 1960. ISSN 0021-9223. doi: 10.1115/1.3662666.

[18] R. H. Aungier. *Turbine Aerodynamics: Axial-Flow and Radial-Flow Turbine Design and Analysis*. ASME Press, 01 2006. ISBN 0791802418. doi: 10.1115/1.802418.

[19] S. C. Kacker and U. Okapuu. A Mean Line Prediction Method for Axial Flow Turbine Efficiency. *Journal of Engineering for Power*, 104(1):111–119, 01 1982. ISSN 0022-0825. doi: 10.1115/1.3227240.

[20] J. Dunham and P. M. Came. Improvements to the Ainley-Mathieson Method of Turbine Performance Prediction. *Journal of Engineering for Power*, 92(3):252–256, 07 1970. ISSN 0022-0825. doi: 10.1115/1.3445349.

[21] D.G. Ainley, G.C.R. Mathieson, Aeronautical Research Council, and Aeronautical Research Council Ministry of Supply. *An Examination of the Flow and Pressure Losses in Blade Rows of Axial-flow Turbines*. ARC technical report. H.M. Stationery Office, 1951.

[22] R. P. Benedict and N. A. Carlucci. *Losses across Abrupt Enlargements and Contractions*, pages 23–26. Springer US, Boston, MA, 1966. ISBN 978-1-4684-6063-6. doi: 10.1007/978-1-4684-6063-6_6.

A | Appendix A

Blade profile construction is explained in section 2.2. Here are reported more in detail the equations used, some taken from Aungier [13], while others were constructed for the eventuality.

First, the camberline is drawn from the equation of a circular arc of radius R_c, passing through $\left(-\frac{c}{2}; 0\right)$, $\left(\frac{c}{2}; 0\right)$ and y_0, the point of maximum camberline height.

The points and the construction is shown in Figure A.1.

Camberline Creation
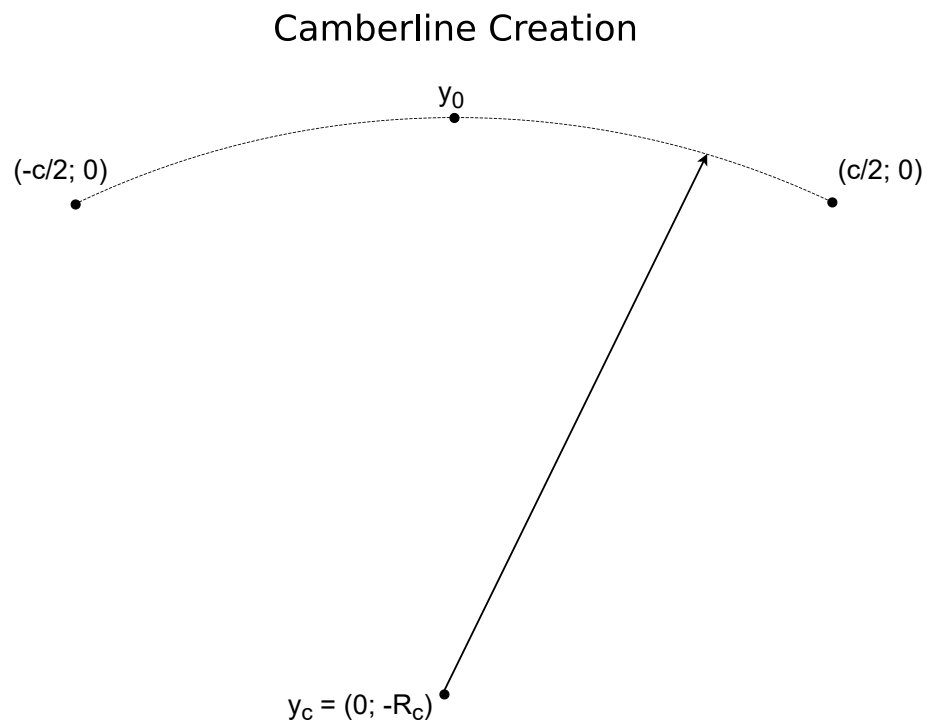
Figure A.1: Camberline construction for DCA blade.

Its equations are reported in Equation A.1.

$$R_c = \frac{c}{2 \cdot \sin\left(\frac{\theta}{2}\right)}$$

$$y_c = -R_c \, \cos\left(\frac{\theta}{2}\right) \qquad \text{(A.1)}$$

$$y_0 = \frac{c}{2} \tan\left(\frac{\theta}{4}\right)$$

Then, the lower profile is drawn, again with the equation of a circular of radius R_l passing through the point of minimum thickness and blending with the edges radii. The equations referring to its construction in Figure A.2 are presented in Equation A.2.
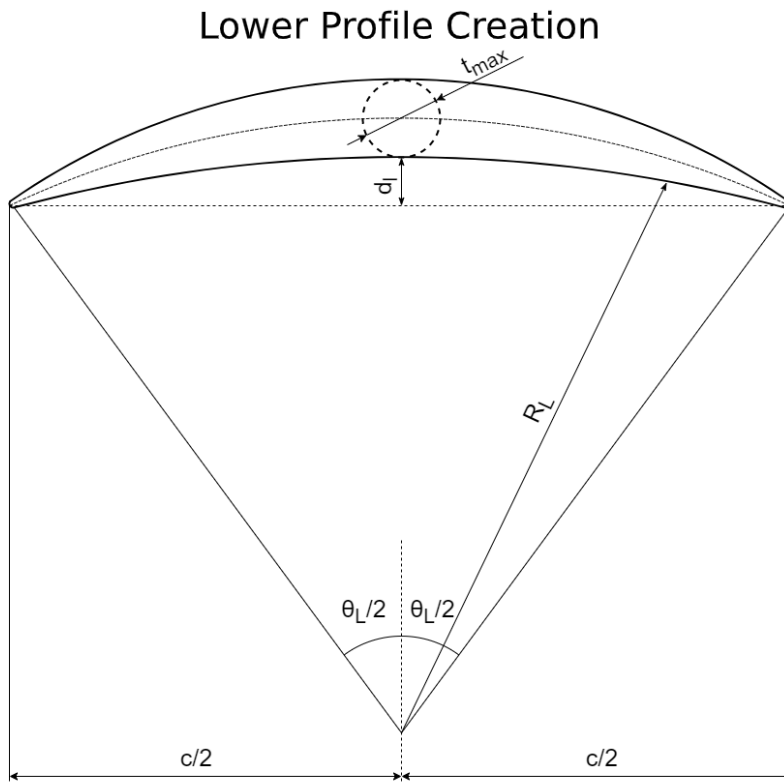
Figure A.2: Lower profile geometrical parameters for DCA blade.

$$d_l = y_0 - \frac{t_{max}}{2} - \frac{t_e}{2} \sin\left(\frac{\theta}{2}\right)$$

$$R_l = \frac{d_l^2 - \left(\frac{t_e}{2}\right)^2 + \left(\frac{c}{2} - \frac{t_e}{2}\cos\left(\frac{\theta}{2}\right)\right)^2}{2\left(d_l + \frac{t_e}{2}\right)}$$

$$\theta_l = 2\arcsin\left(\frac{\frac{c}{2} - \frac{t_e}{2}\cos\left(\frac{\theta}{2}\right)}{R_l + \frac{t_e}{2}}\right)$$

$$y_l = y_0 - \frac{t_{max}}{2} - R_l + \sqrt{R_l^2 - x^2}$$

(A.2)

The problem reported of opposite curvature is presented when d_l is negative, bringing the point of the lower profile below the two edges extremities.

The upper profile presents a similar construction, with the difference of d_u, being the equivalent of d_l, cannot be negative. The equations are reported in Equation A.3.

$$d_u = y_0 + \frac{t_{max}}{2} - \frac{t_e}{2} \sin\left(\frac{\theta}{2}\right)$$

$$R_u = \frac{d_u^2 - \left(\frac{t_e}{2}\right)^2 + \left(\frac{c}{2} - \frac{t_e}{2}\cos\left(\frac{\theta}{2}\right)\right)^2}{2\left(d_u - \frac{t_e}{2}\right)}$$

$$\theta_u = 2\arcsin\left(\frac{\frac{c}{2} - \frac{t_e}{2}\cos(\frac{\theta}{2})}{R_u + \frac{t_e}{2}}\right)$$

$$y_u = y_0 + \frac{t_{max}}{2} - R_u + \sqrt{R_u^2 - x^2}$$

(A.3)

Finally, leading and trailing edges are drawn, using the equation for a circle centered in (x_e, y_e), of radius $r_0 = \frac{t_{TE}}{2}$. The equations for x_e and y_e is depicted in Equation A.4.

$$x_e = \pm\left(\frac{c}{2} - \frac{t_{TE}}{2}\cos\left(\frac{\theta}{2}\right)\right)$$

$$y_e = \frac{t_{TE}}{2}\sin\left(\frac{\theta}{2}\right)$$

(A.4)

The construction of the edges is shown in Figure A.3.

Edges Creation
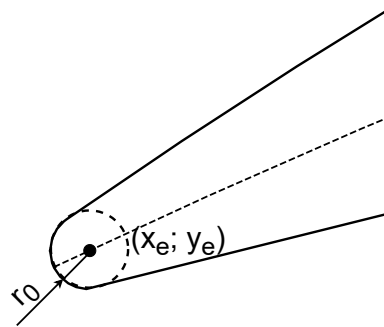
Figure A.3: DCA edges creation.

The last step is to stagger the blade, by simply performing a rigid rotation around the z-axis of the angle γ, as described in Equation A.5.

$$\begin{bmatrix} x' \\ y' \end{bmatrix} = \begin{bmatrix} \cos(\gamma) & -\sin(\gamma) \\ \sin(\gamma) & \cos(\gamma) \end{bmatrix} \begin{bmatrix} x \\ y \end{bmatrix} \tag{A.5}$$

The final result is shown in Figure A.4.

Staggered Blade
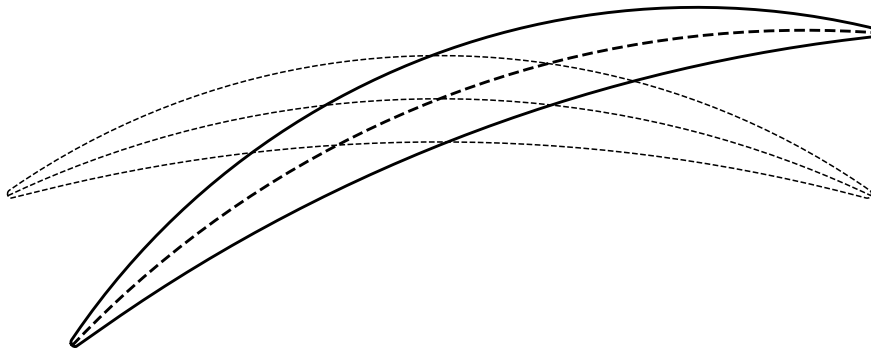
Figure A.4: Blade rotation of the stagger angle

List of Figures

List of Tables

List of Symbols

Variables

Variable	Description	SI unit
AR	aspect Ratio	$[-]$
b	blade height	m
C_D	drag coefficient	$[-]$
C_L	lift coefficient	$[-]$
c	chord	m
D_{eq}	diffusion factor	$[-]$
D_m	mean diameter	m
h	enthalpy	$\dfrac{kJ}{kg}$
I	rothalpy	$\dfrac{kJ}{kg}$
i	incidence angle	$^\circ$
l	work	$\dfrac{kJ}{kg}$
M	Mach number	$[-]$
M_w	Mach number in relative frame	$[-]$
$\dot{m}$	mass flow rate	$\dfrac{kg}{s}$
N_{bl}	number of blades	$[-]$
N_{st}	number of stages	$[-]$
o	throat opening	m
P	pressure	Pa
R_c	camberline radius	m
Re_c	Reynolds number base on chord	$[-]$
s	entropy	$\dfrac{kJ}{kgK}$
s	blade spacing	m

Variable	Description	SI unit
T	Temperature	K
t_{max}	maximum blade thickness	m
t_{TE}	trailing edge thickness	m
U	peripheral velocity	$\dfrac{m}{s}$
V	absolute velocity	$\dfrac{m}{s}$
W	relative velocity	$\dfrac{m}{s}$

Variable	Description	SI unit
α	absolute angle	°
β	relative angle	°
β	pressure/expansion ratio	$[-]$
γ	stagger angle	°
Δ	difference	$[-]$
δ	deviation angle	°
ϵ	kinematic deflection	°
η	efficiency	$[-]$
θ	camber angle	°
θ_w	wake momentum thickness	$[-]$
λ	work coefficient	$[-]$
μ	dynamic viscosity	$\dfrac{kg}{m\,s}$
ρ	density	$\dfrac{kg}{m^3}$
σ	solidity	$[-]$
τ	tip clearance	m
ϕ	flow coefficient	$[-]$
χ	reaction degree	$[-]$
$\bar{\omega}$	pressure loss coefficient	$[-]$

Subscripts

Subscript	Description
c	charge
cl	clearance
d	discharge
des	design
ew	endwall
in	inlet station
is	isoentropic
m	meridional
max	maximum
opt	optimum
out	outlet station
rotor	rotor cascade
sec	secondary
stator	stator cascade
T	total thermodynamic condition
TT	total to total
t	tangential
TE	trailing edge
tip	tip clearance

Acronyms

Acronym	Description
CAES	Compressed Air Energy Storage
CC	Compressor in Charge Mode
CD	Compressor in Discharge Mode
CFD	Computational Fluid Dynamics
DCA	Double Circular Arc
HE	Heat exchanger
IGV	Inlet Guide Vane

Acronym	Description
LAES	Liquid Air Energy Storage
OGV	Outlet Guide Vane
PHS	Pumped Hydroelectric Storage
PS	Pressure Side
PTES	Pumped Thermal Energy Storage
SS	Suction Side
TC	Turbine in Charge Mode
TD	Turbine in Discharge Mode

Acknowledgements